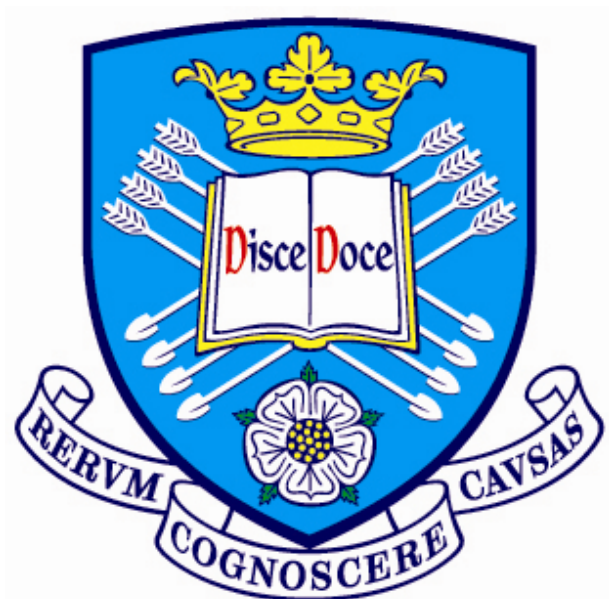# Self-Assembled Liquid Crystal Nanostructures

Xiaobin Mang

Supervised by Prof. Goran Ungar

Dr. Xiangbing Zeng

A thesis submitted for the degree of Doctor of Philosophy in Department of Materials Science and Engineering, University of Sheffield

June 2011

Acknowledgements

It is my pleasure to gratefully acknowledge many people who helped me so much and made this thesis possible. Here I would like to give my particular acknowledgements to the most important people during this work.

First and foremost I am most grateful to my two supervisors Professor Goran Ungar and Dr. Xiangbing Zeng for providing me this opportunity to study in this group, and thanks for their valuable supervising, important suggestions and advices. Thanks for their constant encouragements not only about my study but also my daily life. Without what they have done for me it would have been impossible for me to finish my work. I wish all the best for them.

I would like to thank Dr. Feng Liu who provided me lots of help and very useful suggestions during my study, and all members of our group and people in the Department of Materials Science and Engineering who have ever helped me.

My special thanks to all of our collaborators, Dr. Georg Mehl from Hull University in UK, Professor Carsten Tschierske from Martin-Luther-University at Halle-Wittenberg in Germany, and Prof. Thomas Burgi and Dr. Alastair Cunningham from Université de Genève, and all other members in their groups who were involved in synthesising and providing the compounds studies in this thesis.

Here I would like to thank the Diamond Light Source (United Kingdom) and the European Synchrotron Radiation Facility (France) for the beamtime they have provided for conducting the experiments involved in this thesis.

I would like to thank the Harbin Institute of Technology and China Scholarship Council for providing me this opportunity to study abroad. I am most grateful to the Chinese government, the Department for Innovation, Universities and Skills (DIUS) in UK and the University of Sheffield for their financial support over the past three years.

My special acknowledgement to my mother, my brother and my passed away father for their love, encourage and caring all the time. Particularly, I would like to thank my beloved girl friend, Shaoli Hao, for her love, support and understanding especially over the past three years. Thanks all the people who have ever helped me.

Abstract

Self-assembly of liquid crystalline molecules has been a highly interesting research area over the past few decades. The modification of traditional rod-like liquid crystalline molecules by adding additional functional groups is an effective way to obtain novel liquid crystal phases due to the segregation of incompatible molecular components, and this has been proved by various mesophases obtained from molecules which possess special shapes and structures. More recently, liquid crystalline molecules have been introduced to functionalize metallic nanoparticles to arrange these spherical particles into ordered structures. In this case, liquid crystalline molecules are grafted onto the surfaces of nanoparticles and the strong self-assembly ability of the molecules is the driving force for the ordered arrangement of nanoparticles. This method opens a new way to build spherical nanoparticles into untraditional nanostructures. Gold nanoparticles, due to their potential of building metamaterials that possess novel optical properties, such as negative refractive index and tunable surface plasmon resonance, is of great interest in this field of research.

In this thesis, the self-assembly behaviour of a number of T-shaped liquid crystalline molecules have been investigated by small angle X-ray scattering (SAXS) and grazing incidence small angle X-ray scattering (GISAXS) methods and some complicated liquid crystal phases formed by T-shaped bolaamphiphiles have been solved. These T-shaped liquid crystalline molecules, each of which is composed of a biphenyl core ended by two terminal polar groups and a relatively long lateral chain, were found to form several novel structures which have never been realized in any liquid crystalline systems reported before.

Using the same experimental methods, the self-assembled nanostructures of liquid crystalline molecules functionalized gold nanoparticles (GNPs) were also investigated. Different ordered superlattice structures including both 2D and 3D ones have been obtained from these hybrid systems. The results show how the mode of self-assembly of gold nanoparticles can be controlled by changing the parameters of coating molecules.

Electron density maps of these structures were reconstructed using the diffraction intensities obtained from experimental results. The corresponding model of each structure was also proposed based on the reconstructed electron density maps as well as the structures and dimensions of molecules. Moreover, some simulation work was conducted, for example diffraction intensity simulation, diffraction pattern simulation and molecular dynamic

simulation, and good agreements between experimental and simulation results have been achieved.

Finally, with the help of GISAXS technique the morphologies of double layers of gold nanoparticles prepared *via* layer-by-layer fabrication method have been investigated. By carefully adjusting the distance between adjacent gold nanoparticle layers, a successful control of the coupling of the localized surface plasmon polariton resonance was reported recently. In this thesis the sideway correlation of gold nanoparticles and the correlation between two gold nanoparticle layers were studied. The features observed in GISAXS patterns can be interpreted very well with relatively simple models.

Contents

CHAPTER 1 Literature Review

1.1 Introduction to Liquid Crystals

1.1.1 Concept of Liquid Crystal

Since the first liquid crystal (LC) phase was found more than one hundred years ago liquid crystalline materials have become a highly interesting research topic. Especially in recent decades, more and more attention has been paid to liquid crystals due to their unique properties and potential applications. The applications of liquid crystalline materials range from displays, telecommunication devices, to biological systems *etc.* and are still expanding, feeding continuous research interests in this field [1-3].

Solid   Liquid crystal   Liquid
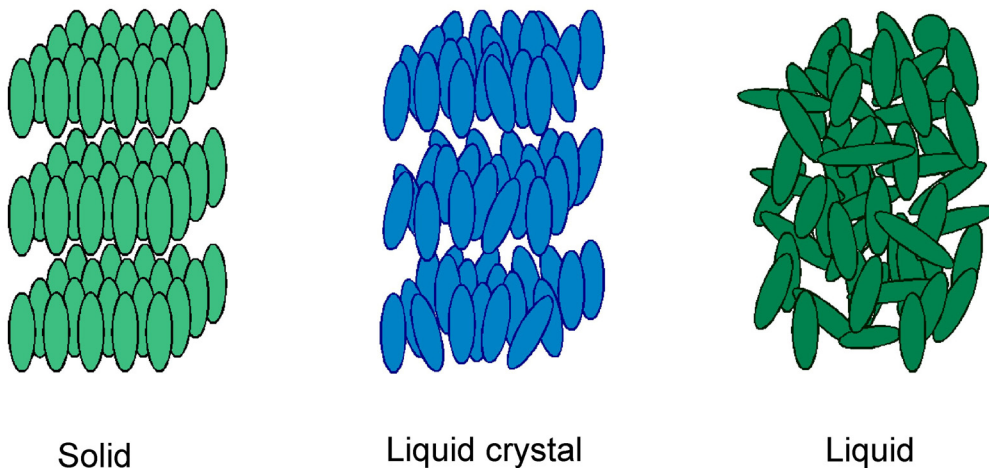
Figure 1.1. Schematic diagrams of solid, liquid crystal and liquid phases. For a typical liquid crystalline material, with increasing temperature the phase transition from solid to liquid occurs through an intermediate liquid crystalline phase (a smectic phase is shown as an example) [4].

It is well known that liquid crystal (LC) is a state of matter which exists in between liquid and solid. As a true thermodynamic stable state of matter, like solid, liquid and gas, liquid crystal phase is always referred to as the "fourth". In the solid state the components (atoms, ions or molecules) are regularly stacked, giving a periodical lattice with both long range positional and orientational order in space. In the liquid state the components can move and tumble randomly and do not show such long range order. However, in a typical liquid crystal phase

(*e.g.* nematic) the molecules with special shape can align along a certain direction called director. The characteristic orientational order of liquid crystal state is between traditional solid and liquid as indicated in Figure 1.1 [1, 5]. Moreover, in contrast to the 3D positional order in the solid, components in a liquid crystal phase can possess long range positional order of lower dimensions, for example in the smectic phase (1D) and the columnar phase (2D) [6]. These unique properties of liquid crystal state are the origin of the term mesogenic state which is used synonymously with mesophase [7].

The characteristic properties of liquid crystal phases can be explained in terms of the special structure of liquid crystalline molecules. Typically, a liquid crystalline molecule consists of a rigid moiety and one or more flexible parts. During the formation of liquid crystals the rigid parts of molecules, often referred to as the "mesogens", align along a certain direction, whereas the flexible parts induce fluidity and improve the mobility of molecules in the liquid crystal phase. The balance of these two factors is essentially the driving force to form liquid crystal phases.

1.1.2 Typical Liquid Crystal Phases

There are various ways of classifying liquid crystal phases, *e.g.* by their molecular features, hence rod-like, discotic and bent-core LCs *etc*; or by their supramolecular assemblies, hence nematic, smectic and columnar phases *etc*. The most commonly used classification is based on how the liquid crystalline phases were obtained, and liquid crystal phases can thus be divided into two categories: thermotropic liquid crystals and lyotropic liquid crystals [8]. The formation of thermotropic liquid crystals is obtained by controlling the temperature of a system which is composed usually of non-amphiphilic, anisometric liquid crystalline molecules. Meanwhile, lyotropic phases are formed by dissolving amphiphilic molecules in suitable solvents and followed by changing the solution concentration [9]. Amphiphilic molecules can form both lyotropic and thermotropic mesophases as these can be induced by adding solvent as well as changing temperature [10].

The formation of liquid crystalline phases also depends on the shape of molecules. Due to the different features of traditional rod-like and disk-like molecules, they are apt to form different mesophases. Rod-like (calamitic) molecules, which are composed of rod-like rigid cores and flexible terminal chains, are likely to form the nematic (N) and the smectic phases (Sm). In

the nematic phase, molecules are oriented with their long axes pointing to a common preferred direction. The nematic phase has the lowest order in all mesophases, and presents a long range orientational order but no long range positional order. In the smectic phase, the rigid cores of molecules form layers which are separated by flexible terminal chains of molecules (1D positional order), and within each layer the molecules possess only orientational order [1]. If the long axes of molecules (or the molecular director) are perpendicular to the layer planes, the phase is specified as the smectic A (SmA); otherwise if the mesogens tilt at an angle with respect to the layer normal the smectic C (SmC) phase is formed (Figure 1.2).
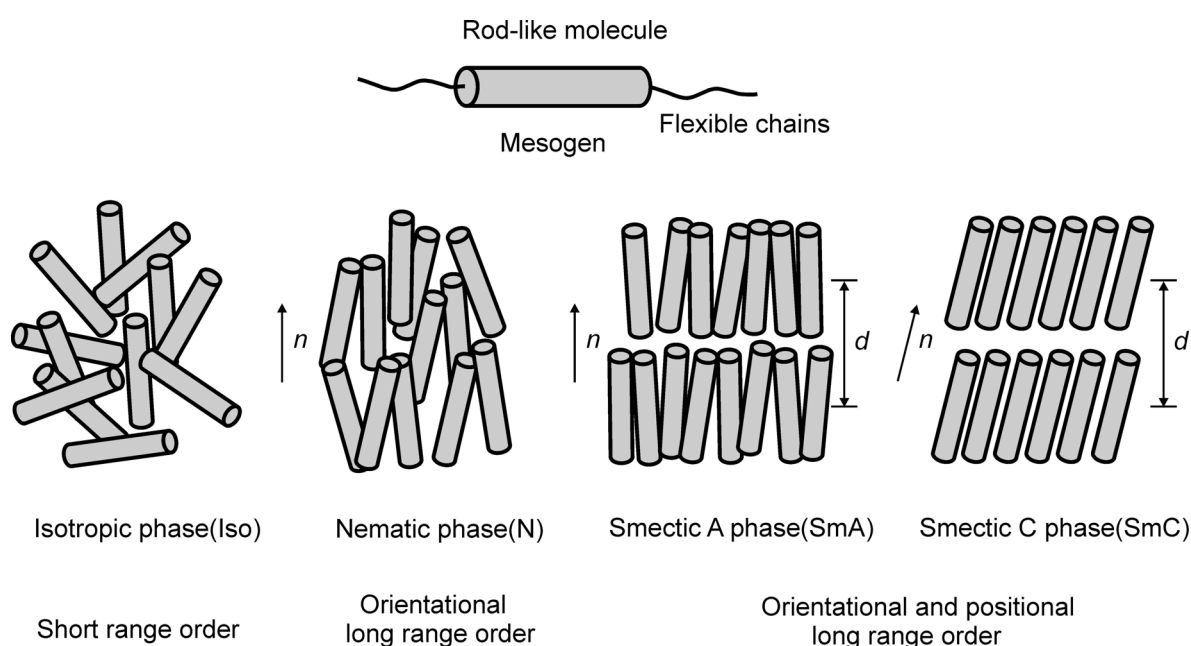
Figure 1.2. Schematic drawing of rod-like molecule and the organization of molecules in different liquid crystal phases. For clarity the alkyl chains are not shown in the models [11].

Molecules with disk-like rigid cores and flexible chains around are commonly called discotic molecules. Due to the special shape, such molecules mainly exhibit discotic nematic (N_D), columnar (Col) and lamellar (Lam) phases [1, 12-13]. As indicated in Figure 1.3, in the discotic nematic phase molecules display only orientational order. In the columnar phase the discotic cores stack into columns with the sideway attached flexible chains filling the intercolumn space, and then these columns pack on lattices with different symmetries, *e.g.* hexagonal, rectangular and oblique lattices or even columnar lamellar phases [14-15]. However, if the molecular shape is neither rod-like nor disc-like, new mesophases may be formed [16].
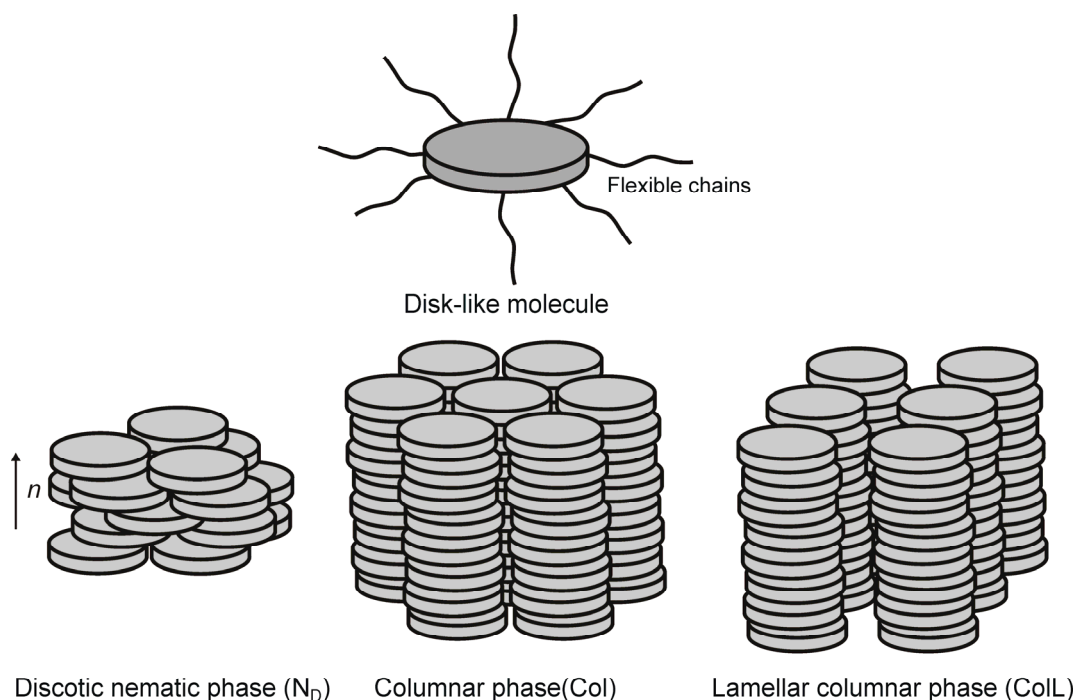
Figure 1.3. The schematic drawing of disk-like molecule and the organizations of molecules in some typical mesophases [4].

1.2 Liquid Crystal Phases of Amphiphilic Molecules

1.2.1 Liquid Crystalline Phases of Binary Amphiphiles

Binary amphiphilic molecules are composed of two incompatible segments without necessarily an anisometric unit. The self assembly in amphiphilic systems is based on the segregation of the two incompatible molecular parts into their own subspaces, and the mesophases formed are determined by the relative volume of these two. As indicated in Figure 1.4, by increasing the volume of one segment, for example that of the polar chains, we can obtain a series of mesophases: starting from the smectic phase with 1D positional order when the two segments have nearly equal volume fractions, followed by the bicontinuous network phase(s) with 3D cubic symmetry, the 2D columnar phase, and finally the 3D cubic micellar phase(s). Interestingly, by increasing the volume of the other segment then we obtain a series of "reversed" phases, which means the subspaces formed by the two incompatible segments exchange their positions in these mesophases as indicated by the reversed colour in Figure 1.4 [12-13, 17-23].

4
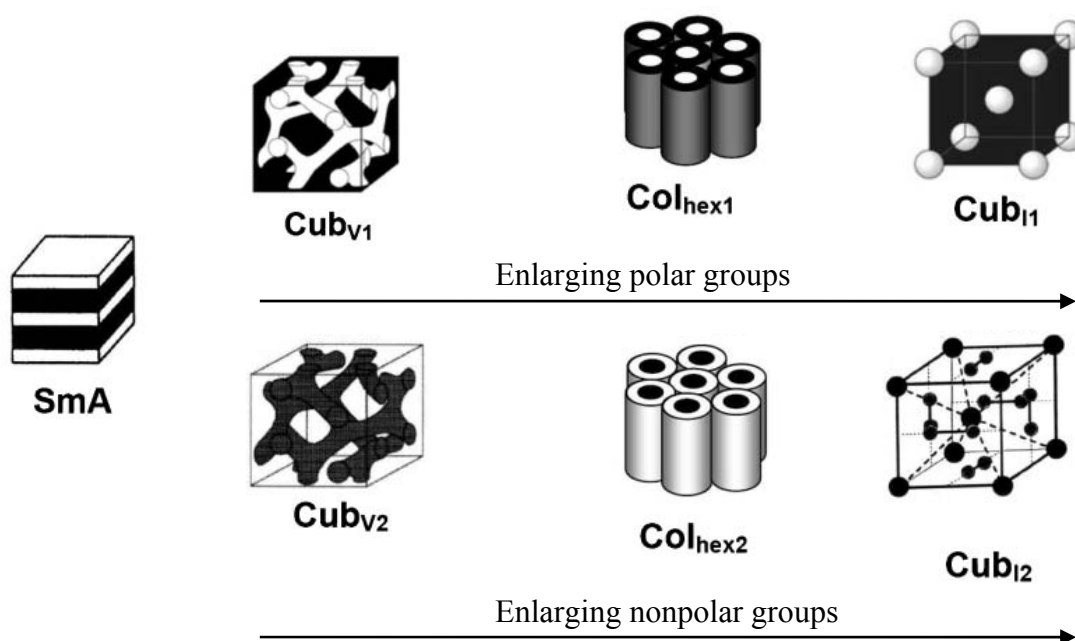
Figure 1.4. The general phase sequence of flexible binary amphiphiles as obtained by changing the volume fraction of the incompatible molecular segments [17]. (in these models the polar parts are shown in black, lipophilic parts in white); Abbreviations: Col_{hex} = hexagonal columnar phase; Cub_V = bicontinuous cubic mesophase formed by interpenetrating networks of branched columns, Cub_I = discontinuous cubic mesophase built up by spheroidic aggregates; the subscript ''1'' indicates ''normal type'' phases where the stronger attractive forces (hydrogen bonding) are located in the continuum outside the aggregates, the subscript ''2'' is assigned to ''reversed type'' phases where the strongest attractive forces are located inside the aggregates.

As binary amphiphiles are merely composed of two different molecular parts which provide the fundamental driving force for the self assembly process, the number of possible mesophases which can be obtained from these binary amphiphiles is limited mainly to those structures described above [18, 24-27]. Similar to diblock copolymer in which the complexity and diversity of the self organized structures can be significantly enhanced by modifying the binary amphiphiles to ternary *i.e.* from AB-diblock to ABC triblock copolymers. The combination of the three distinct parts, which are all incompatible with each other, increases the block sequences from only one in binary amphiphiles to several in ternary amphiphiles as indicated in Figure 1.5. By changing the topology, the block size and the block sequence different phase structures can be obtained [28-32]. So from this point of view mesophases with higher levels of complexity can be expected in polyphilic molecules which combine three different functional groups.
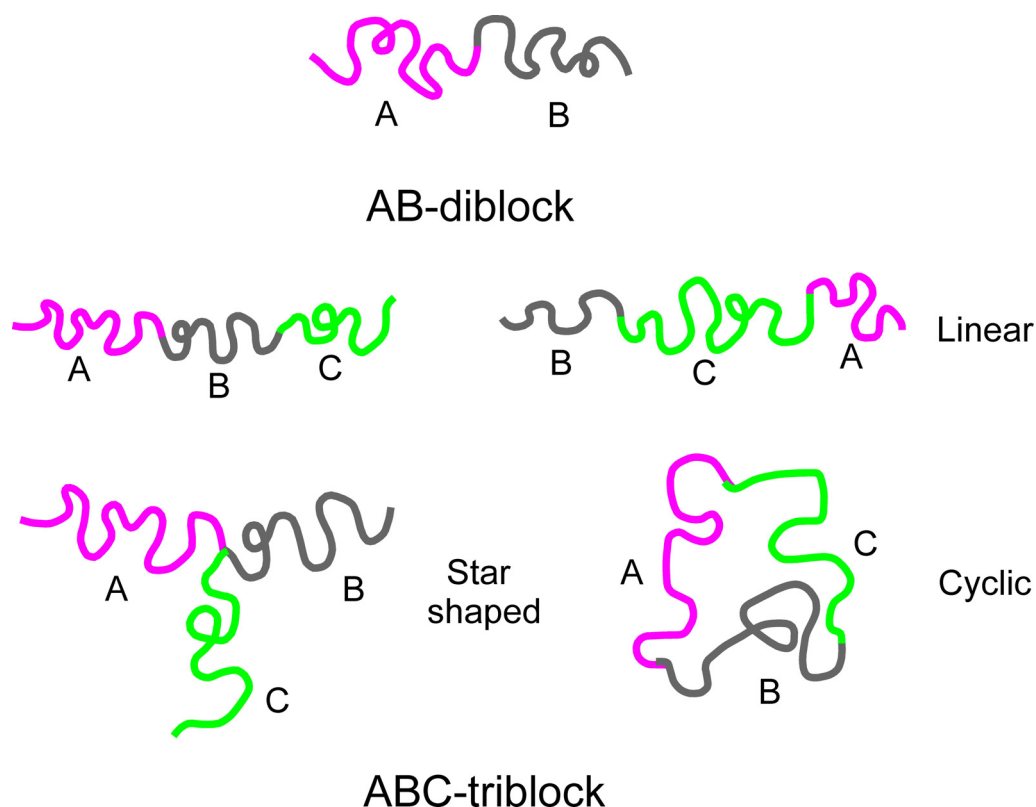
Figure 1.5. Comparison of diblock-copolymers and different types of triblock copolymers; only two of the three possible sequences for linear triblock copolymers are shown [33-35].

1.2.2 Liquid Crystalline Phases of Ternary Amphiphiles

Liquid crystal structures formed by traditional rod-like molecules are dominated by smectic phases due to the parallel organization of rigid cores and the segregation of incompatible molecular parts, while binary amphiphilic molecules form only limited structures as described above. So in order to obtain novel structures many attempts have been tried, for example, by adding lateral substituent to the rigid core of rod-like molecules. However, if there is no strong incompatibility between lateral chains and terminal groups, the mixing of these two parts and the loss of long range positional order induced by the steric distortion always lead to the formation of nematic phases [1, 36]. Bearing this in mind, one of the basic ideas to obtain new mesophases should be based on the principle of functionalizing rod-like molecules by terminal groups and lateral chain which are strongly incompatible with each other and also with the cores [37], and this leads to the well studied T-shaped molecules.

A typical T-shaped molecule generally consists of three distinct incompatible parts, a hydrophilic part, a flexible hydrophobic part and a rod-like core [38]. According to the combination sequence and relative position of each part, one linear and two T-shaped ternary amphiphilic molecules can be formed and these molecules can be considered as four-block molecules with different block sequences as indicated in Figure 1.6.
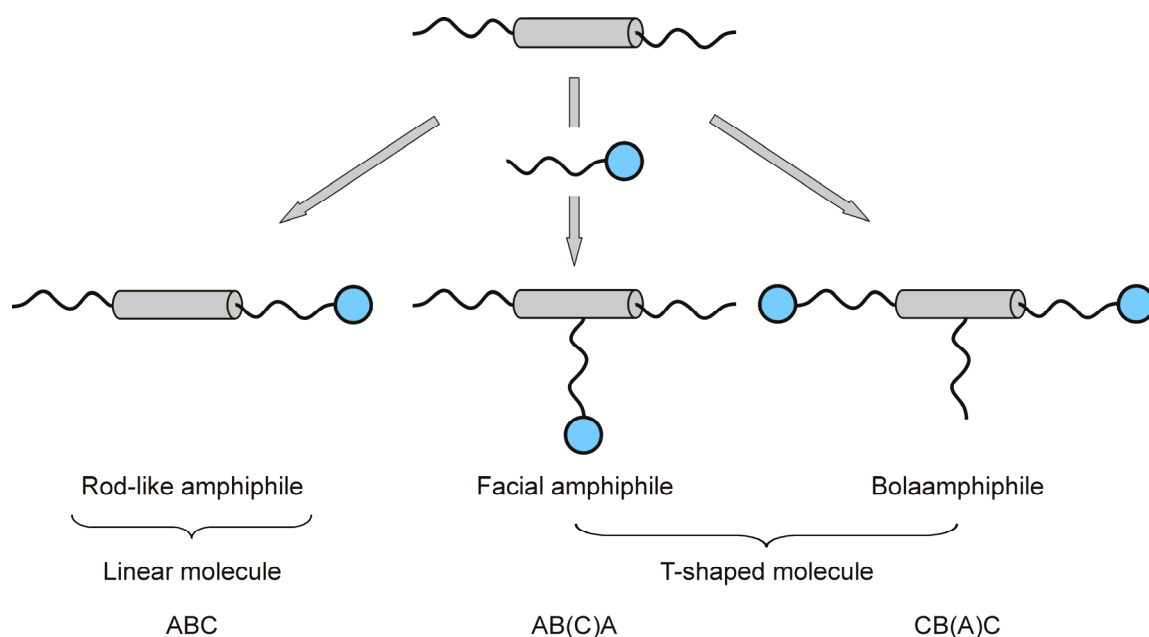
Figure 1.6. Distinct molecular topologies and block sequences of ternary amphiphilic molecules incorporating rigid rod-like segments (ternary block-molecules). The facial amphiphiles and bolaamphiphiles discussed here can be regarded as ternary AB(C)A and CB(A)C tetra-block molecules, respectively, where A denotes the non-polar chain(s), B the aromatic core and C the polar group(s) [11].

A rod-like ternary amphiphile is also a linear molecule, in which a hydrophilic group is grafted to one terminal of the rigid core and a hydrophobic group is grafted to the other (see Figure 1.6). Similar to traditional rod–like molecules, the mesophaes formed by this kind of amphiphiles are dominated by smetic A and smectic C layer structures, although oblique columnar phases have been obtained only for compounds with long hydrophobic chains [39-42]. This is because in smectic phases the hydrophilic groups are confined between layers, and the segregation of hydrophilic and hydrophobic groups favours the parallel alignment of the rigid cores that additionally stabilises the layer structures. As a result, only a large volume of hydrophobic chains would be able to cause the collapse of layer structures, leading to the formation of columnar phases [43-44].

If the hydrophilic groups are grafted to the two terminals while the hydrophobic group is grafted to the lateral position of the rod-like core, a bolaamphiphile with a nonpolar lateral chain is formed (Figure 1.6). Compounds shown in Figure 1.7a are the first reported bolaamphiphile molecules. For these bolaamphiphiles the strongest attractive force *i.e.* the hydrogen bonding network and the tendency of segregation between different groups would favour the stabilization of smectic A phase for compounds without or with short lateral chains. By increasing lateral chain length the stability of smectic phase is reduced and the SmA phase is replaced by disturbed layer structure (SmA$^+$). Further increasing of the lateral chain length leads to a complete collapse of the layer structure and the formation of different columnar mesophases.

Another type of well studied bolaamphiphiles is shown in Figure 1.7b, in which the traditional simple hydrocarbon lateral chain is replaced by fluorinated one. The fluorinated lateral chain has an even stronger incompatibility with the other parts of the molecule, and the volume of a CF_2 group is also larger than that of a CH_2 group. As a result, different mesophases were obtained either by changing temperature or by increasing the lateral chain length [45-49]. According to their phase behaviour, these compounds can be divided into three groups. Similar mesophases as in the alkyl-substituted compounds (Figure 1.7a) were found for group I, while group Π and Ш compounds tend to form mesophases with large lattice parameters or form lamellar phases. Other bolaamphiphiles that have lateral chains with different components or different polar groups for example, have also been studied [50-52].

In facial amphiphilic ternary block molecules the positions of the polar and the nonpolar groups are reversed in comparison with bolaamphiphiles: the hydrophilic group is grafted to the lateral positions of the rigid rod-like core, and the hydrophobic groups are located at terminal positions (Figure 1.6). Although the combination of different parts in facial and bola amphiphile is different, the crucial driving forces of forming novel liquid crystalline phases for both are the same, which are the segregation of different functional groups, the strong competition between the parallel alignment of rigid cores and the steric interaction caused by lateral chains [53].
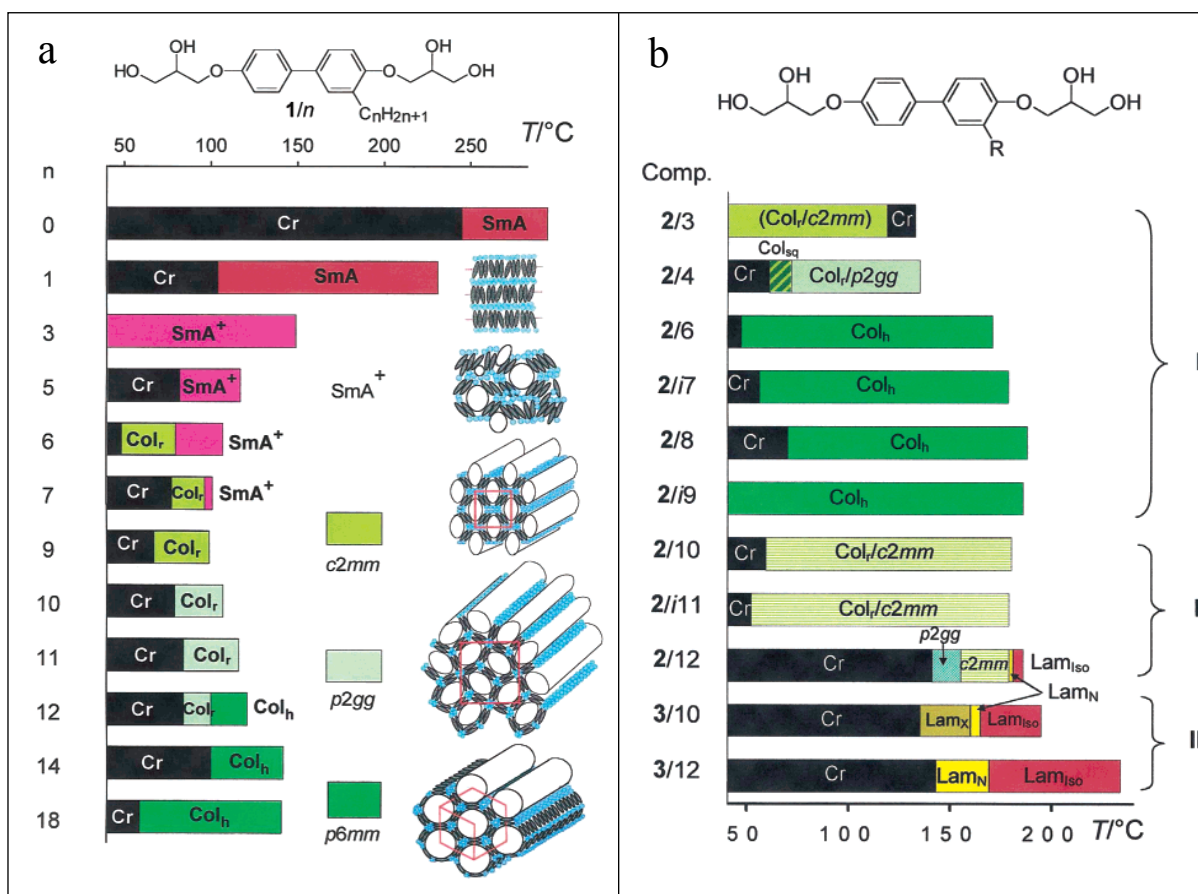
Figure 1.7. a) Dependence of the liquid crystalline phases of compounds 1/n with respect to the length of the lateral alkyl chains and models for the organization of the molecules in their mesophases. Cr= crystal, SmA= smectic A phase, SmA[+]= disordered layer phase, Colr = centered (*c2mm*) or noncentered (*p2gg*) rectangular columnar phases, Col_h = hexagonal columnar phase (*p6mm*). Models: blue = hydrogen-bonding networks of the terminal diol groups [54]; white = microsegregated regions of the lateral alkyl chains; gray = rigid biphenyl units. b) Dependence of the liquid crystalline phases of compounds 2/n and 3/n with respect to the length of the semiperfluorinated lateral chain. In compound 2/n, R = $(CH_2)_3CnF_{2n+1}$. In compound 3/n: R = $O(CH_2)_6CnF_{2n+1}$) [48].

One of the general phase diagrams of facial amphiphilic compounds is shown in Figure 1.8, in which the rigid terphenyl core is terminated by two linear alkyl chains with the same length and a polar lateral chain is connected laterally. The phase sequence shown here has been observed either by increasing the volume fraction of the polar lateral chain or by reducing the volume fraction of the terminal ends. Other facial amphiphiles with different molecular structures were also developed, for example by incorporating different elements in the polar lateral chain [52], or by replacing its end with a -COOH group [51] or liquid crystalline crown ether [55]. The two terminal ends could also have identical or different lengths [53].
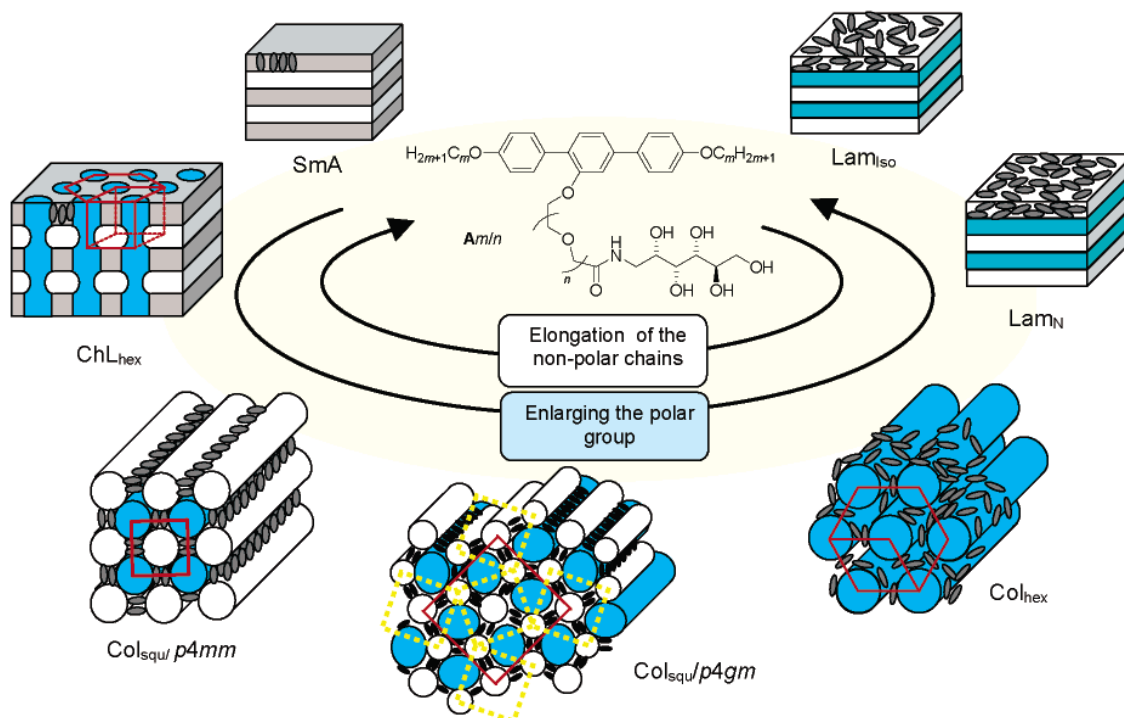
Figure 1.8. Schematic view of the phase sequence of the facial amphiphiles with lateral polyhydroxy groups as a function of the size of polar lateral and lipophilic terminal groups [56].

1.3 Self-assembly of Nanoparticle - Liquid Crystal Hybrid System

Self-assembly of metallic, magnetic or semiconducting nanoparticles is a promising way to construct well ordered nano-structures and to produce large scale structures with small feature sizes. Such nano-structures provide new opportunities for application and devices in various areas. For example drug carriers and biosensors [57], semiconductor nanocrystal based solar cells [58], photodetectors [59] and transistors [60] *etc*. Liquid crystalline materials, which combine order and mobility at molecular level, are perfect candidates for self-assembly of nano-materials. The combination of nanoparticles with liquid crystalline molecules can be generally divided into two categories, both of which will be described in more detail in sections below. The first one is nanoparticles or colloidal particles doped liquid crystal system. In this case, the interactions between the dopant and the liquid crystalline molecules, the formation of particle aggregations *etc* have been intensively studied over the past years, and lots of experimental as well as theoretical achievements have been made (see the section below). The second category is liquid crystalline molecule functionalized nanoparticles. The attempt of grafting liquid crystalline molecules onto the surfaces of inorganic nanoparticles is

quite recent and most of the studies have been focused on gold nanoparticles due to their unique physical and chemical properties.

1.3.1 Colloidal Particle-Liquid Crystal System

Researches on nanoparticle doped liquid crystal system were mainly focused on the assembly of colloidal particles in nematic liquid crystals [61-63], which were driven by the development of new optical elements, photonic structures and metamaterials [64-66]. After colloidal particles are introduced into nematic liquid crystal, the orientation of LC molecules is locally disturbed due to their interactions with the inclusions. Generally, the liquid crystalline molecules, in the vicinity of a colloidal particle, are forced to align along a preferred direction with respect to the surface of the particle. This disturbance leads to the formation of defects in the system and can be considered in terms of the elastic energy of deformation [67-71]. Depending on the strength and direction of the nematic anchoring on the particle surface, topological defects and additional structural forces between the colloidal particles are the key factors that affect the final structures. The topological defects can be further divided into point defects and line defects, and they lead to linear chains and two dimensional arrays of colloidal particles respectively [72]. The structural forces in nematic liquid crystals are long range and usually spatially anisotropic, hence the disturbance spreads on a large scale [73]. Consequently, these colloidal-liquid crystal systems end in one of the numerous metastable colloidal structures corresponding to the local minima of nematic free energy [74].

Intensive studies have indicated that the interactions between colloidal particles and liquid crystal molecules not only depend on the molecular structure, elastic properties of liquid crystal, but also the type, size and shape of the inclusions. Many different kind of self-assembly patterns have been reported, including two dimensional colloidal crystals in thin nematic cells [75], two dimensional hexagonal and colloidal lattices at interfaces [67, 76], colloidal particles linear chains [77-78], and hierarchical self-assembled nematic colloidal superstructures [79-80].

1.3.2 Mesogen Functionalized Nanoparticles

Self assembly of metallic nanoparticles, functionalized by liquid crystalline molecules, has attracted more and more attention in the past few years triggered by their broad applications [81]. By grafting liquid crystalline moieties of various shapes to the surface of nanoparticles the packing behaviour of nanoparticles can be affected due to the tendency for alignment of the anisotropic molecules, leading to different nanoparticle packing styles. In this section, a brief introduction to the synthesis of mesogen functionalized gold nanoparticles will be given first, followed by a discussion on nanostructures formed by gold nanoparticles covered by different mesogens, including rod-like, disk-like, bent-core and dendrimeric ones. Our research focused on rod-like mesogen functionalized gold nanoparticles, with the aim of investigating the effect of coating molecules on the gold nanoparticle self-assembly. The results are presented and discussed in detail in chapter 4 of this thesis.

1.3.2.1 Synthesis of Mesogen Functionalized GNPs

Gold nanoparticles, due to their chemical stability, facile surface functionalization [82-84] and potential applications especially in the medical field [85-86], have been the most studied nanoparticles. Furthermore, while the packing behaviour of hard bodies is highly dependent on geometry and polydispersity [87], monodisperse gold nanoparticles are relatively easy to synthesize with possible size ranging from 1 nm to about 150 nm [85]. However, because of their metallic character, gold nanoparticles are likely to attract each other and eventually form aggregations. A successful attempt to overcome this problem was first reported by stabilizing gold nanoparticles with alkanethiols [88], and this led later on to the efficient and well established Brust-Schiffrin method or two-phase approach [89-90] to synthesize mesogen functionalized gold nanoparticles. Now this method is widely adopted due to its reliability comparing to some other physical methods [91] and the more recently developed one step method [92-93].
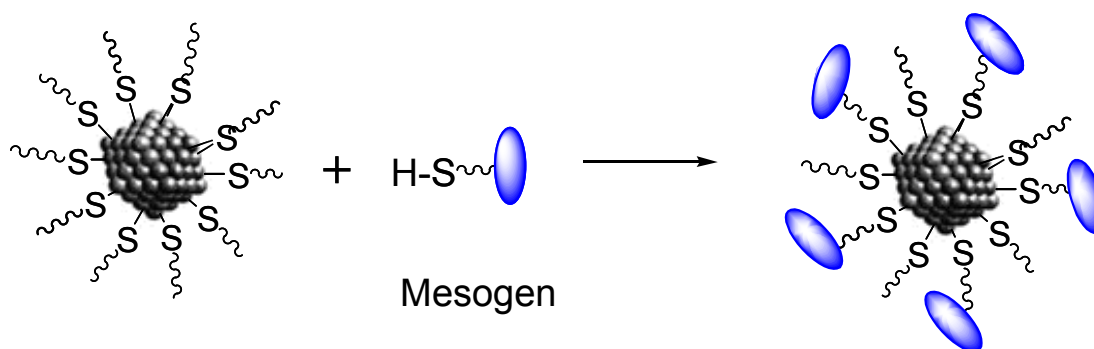
Figure 1.9. Schematic representation of the synthesis process of mesogen covered gold nanoparticles. The monolayer protected gold nanoparticle is functionalized *via* an exchange reaction [94].

During the synthesis of mesogen functionalized gold nanoparticles *via* Brust-Schiffrin method, two main steps are involved. Firstly, gold nanoparticles covered with hydrocarbon monolayer (thiol chains) are synthesized. The hydrocarbon monolayer can screen the interparticle attractive force and make nanoparticles stable and processable in solvents [95]. In the second step, the hydrocarbon covered gold nanoparticles are further functionalized by liquid crystalline molecules *via* an exchange reaction (Figure 1.9). During the reaction some or all of the covering hydrocarbons are replaced by the mesogenic molecules. So the final gold nanoparticles can be decorated either completely by mesogens or by both mesogens and hydrocarbon chains, and the ratio between the two can be controlled by changing reaction conditions. The mesogens and remaining hydrocarbon chains here are also called ligands and co-ligands respectively.

1.3.2.2 Rod-like mesogen (laterally and end-attached) covered GNPs

Rod-like (calamitic) molecules possess significant anisotropy due to the large difference between their length and breadth. The elongated rigid cores usually have stronger attractive force between them when they are parallel to each other, and this can also reduce the collision between molecules effectively [7]. The flexible chains can improve the mobility of molecules, leading to the formation of liquid crystal phases in which molecules possess directional and/or positional orders. As representatives of liquid crystalline molecules, rod-like molecules have been well studied.
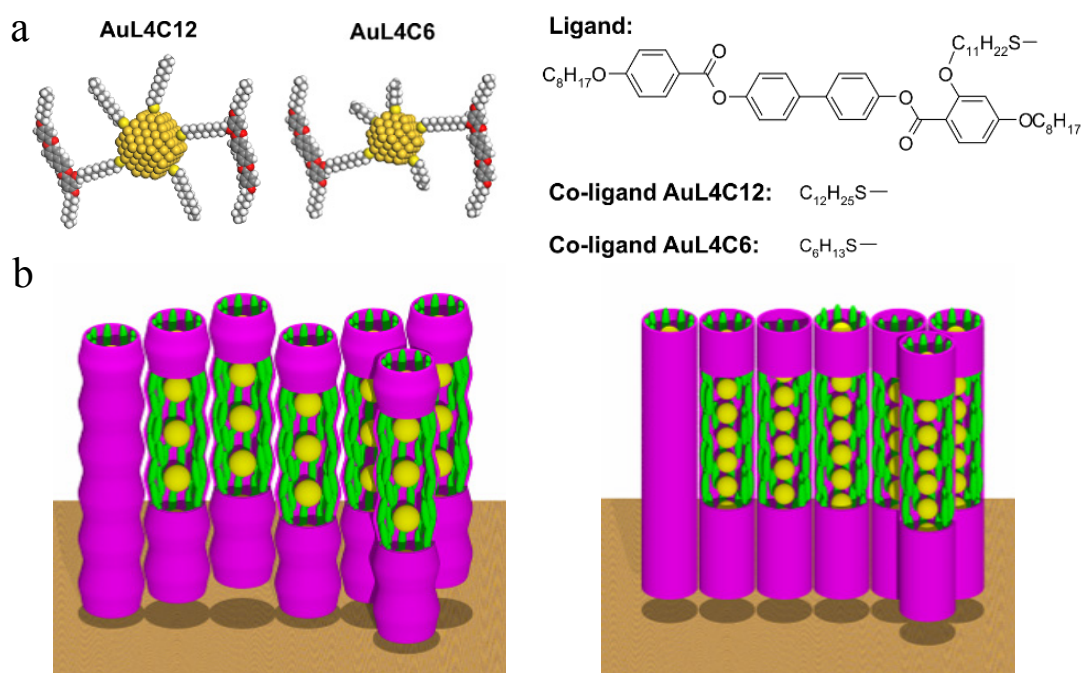
Figure 1.10. a) Models of functionalized gold nanoparticles and the chemical structure of mesogenic ligand and co-ligands. b) Structure models of the gold nanoparticle strings. Left: AuL4C12 which has long co-ligands. Right: AuL4C6 which has shorter co-ligands. The yellow balls and the green color represent gold string and mesogens respectively.

Using the Brust-Schiffrin method rod-like molecules were successfully grafted to gold nanoparticles *via* alkylthiol spacers and some interesting results have been obtained. For example, a change of the shape morphology of such liquid crystalline gold nanoparticles, which is caused by the density coverage and the anisotropic interactions between liquid crystalline molecules, has been reported [96]. Also such functionalized gold nanoparticles have been found to exhibit nematic phase behaviour at room temperature [87, 94]. By controlling the co-ligand chain length, 2D and 3D structures were found in these gold nanoparticle systems [97]. The decorated gold nanoparticles, along with covering mesogen ligands and co-ligands, are schematically shown in Figure 1.10a. For nanoparticles functionalized by a ligand containing 4 benzene rings and dodecylthiol co-ligand (AuL4C12) rhombohedral lattices were found, and for particles coated with shorter hexylthiol co-ligands (AuL4C6) 2D rectangular and hexagonal structures were obtained. In all of these 2D and 3D structures, the functionalized gold nanoparticles form columns (gold strings) with rigid aromatic cores lying parallel to the column axes, while co-ligand chains fill the gaps between

neighbouring particles in the same column (see Figure 1.10b). Consequently, the intracolumnar particle distance can be adjusted by the length of the co-ligands used.
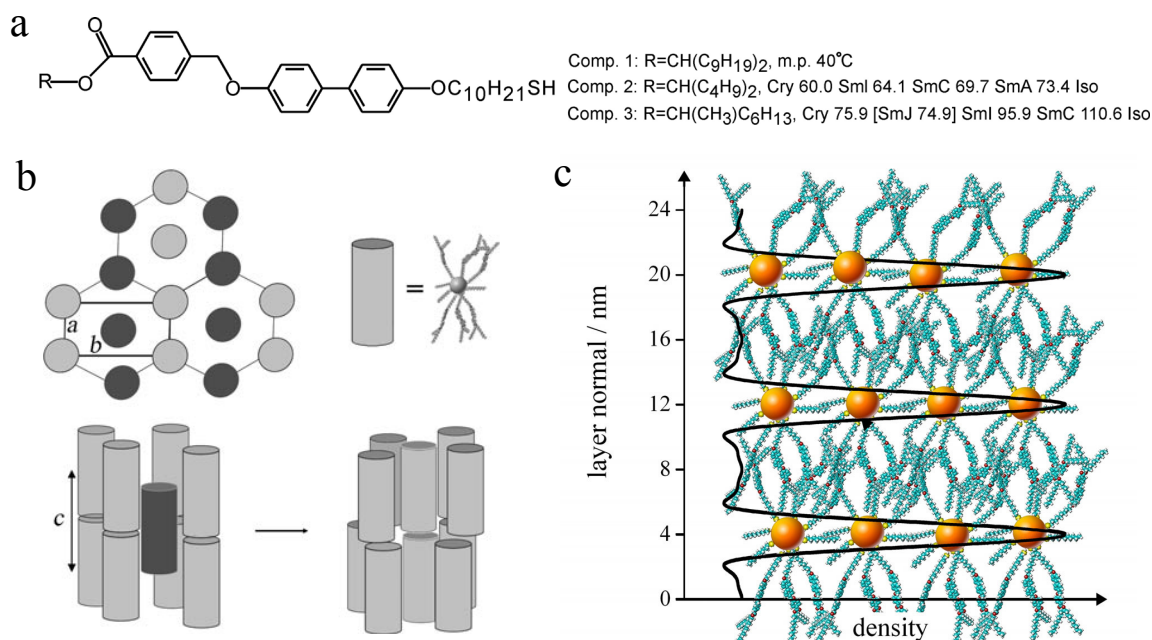
Figure 1.11. a) Structure of mesogenic ligands which are end attached to gold nanoparticles. b) Schematic drawing of the arrangement of nanoparticles in the columnar phase, as viewed from above (top, left) and from the side (bottom, left); a, b, and c are the crystal lattice parameters. A gold particle is located at the center of each cylinder, and the cylinder is filled by orientationally and positionally disordered n-alkyl and mesogenic thiol molecules redistributed around the gold cluster. The two colors distinguish particles with their mass center (gold cluster) positioned at different levels along the c direction. Bottom: the smectic phase and columnar phase formed observed here are closely related. c) Model of the smectic phase in which metallic cores rich layers are intersected by organic layers. The black curve represents the electron density profile along layer normal in the smectic phase [98].

Rod-like mesogen functionalized gold nanoparticles were also reported recently by Wojcik *et al*. [98] to form layer and columnar phases. In this case, the mesogens were grafted to gold nanoparticles *via* a spacer from the end of each molecule rather than from a lateral position, together with the alkylthiol co-ligands. For gold nanoparticles passivated by mesogens with long forklike end groups (compound 1 in Figure 1.11a) and co-ligands $C_{10}H_{21}SH$, typical smectic A phase was obtained. In this structure the gold particle layers are separated by the organic sublayers which are formed by the mesogenic ligands, while the alkyl thiol co-ligands fill the space between gold nanoparticles in the same layer as indicated in Figure 1.11b and

Figure 1.11c. However, if a shorter forklike tail or a 2-octyl end were used at the end of the mesogen (compound 2 and compound 3) then a columnar phase with body centered orthorhombic lattice was formed (see Figure 1.11b). This body centered lattice can be obtained by modification of simple hexagonal columnar phase by shifting every second row of the columns a distance half the side length of the unit cell along the column axis.

Further investigations indicated that different ordered structures of such decorated gold nanoparticles can also be obtained by changing the length of n-alkyl thiols (co-ligand) when the mesogenic ligand is kept the same [99]. Figure 1.12 shows the different structures formed by gold nanoparticles functionalized with the same mesogenic ligand (compound 3) but different co-ligands which are composed by n-alkyl thiols having 6, 8 and 12 carbon atoms respectively. As indicated, with the increasing of co-ligand length three different phases which Wojcik *et al* called smectic, modulated smectic and 3D columnar phase were obtained. In the modulated smectic phase, the *c* parameter of the 2D rectangular unit cell is the layer thickness while the *a* parameter is the modulation period along the layer. In this 3D phase, they found that the gold particles are arranged into a centred orthorhombic network with the meta particles stacked one above another, so they also called it columnar phase. The influence of the co-ligand length on the final structures was interpreted by analyzing the shape of single decorated gold nanoparticle. It is believed that the smectic phase is formed by particles with mesogenic ligands collected mainly above and below the gold sphere, and the gold particles inside each smectic layer are separated by co-ligands (see Figure 1.11). In this case each particle can be considered to possess a cylindrical shape. With increasing co-ligand chain length, the original cylindrical shape of the columns becomes "tri-cylinder" type or ellipsoidal with the bulky part in the middle, leading to different phases as shown in Figure 1.12c.

In summary, rod-like mesogens can be grafted onto gold nanoparticles either from their ends or sideways, and in both cases gold nanoparticles are able to form ordered phases. However, if the mesogens are attached laterally, the gold nanoparticles form chains with mesogenic ligands form the outer sheaths of such chains with co-ligands filling the gaps between particles. On the contrary, if the mesogens are attached from their ends, then the nanoparticles tend to form layers with mesogens in between and oriented in the direction perpendicular to the layer plane.

a   b   c
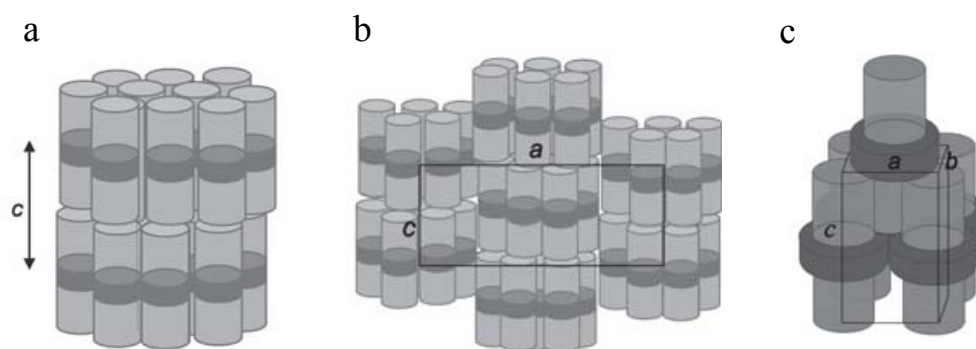
Figure 1.12. Proposed structure models of the smectic A phase (a), the "modulated smectic" phase (b) and the "columnar" phase (c) obtained from gold particles with alkylthiol co-ligands having 6, 8 and 12 carbon atoms, respectively. The mesogen used is compound 3 in Figure 1.11. It is believed that for gold nanoparticles forming liquid crystalline structure the mesogenic ligands and alkyl thiols are redistributed around the gold centre forming cylindrical type objects, the mesogenic cores are collected above and below the gold centre (light grey part of cylinders), while the n-alkyl thiols are collected in the middle (dark grey part of cylinder) [99].

1.3.2.3 Disk-like mesogen covered GNPs

Disk-like molecule also shows a great difference between its length and breadth, but in this case the length and breadth represent the height and diameter of the disk-like core respectively. The rigid part of discotic molecule is usually flat like a dish and is often symmetric, around which flexible chains are connected. The physical properties of this kind of molecules can be influenced significantly by the variation of the core and/or the side chains.
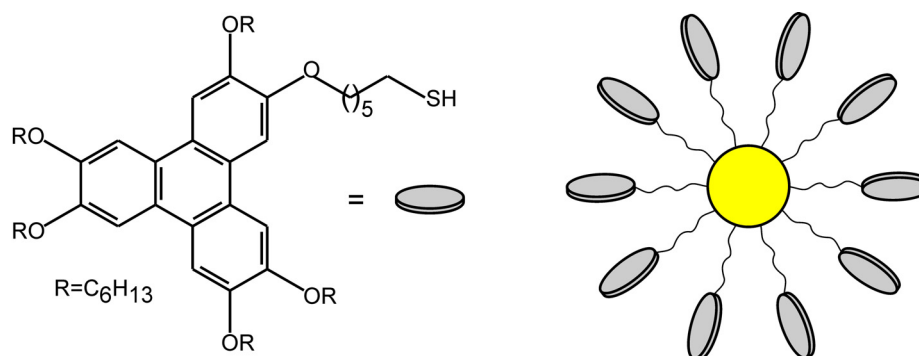
Figure 1.13. Chemical structures of a discotic molecule 6-{[3, 6, 7, 10, 11-pentakis (hexyloxy)-2-triphenylenyl] oxy}-1-hexanethiol and a schematic drawing of how they are attached to a gold nanoparticle.

The incorporation of metallic nanoparticles with discotic liquid crystalline molecules would enable the commonly formed columnar phase to possess the properties of metallic particles as well as the processing, handling and self-assembly properties of liquid crystal. These columnar phases can be potentially applied as one dimensional conductors, photoconductors, and gas sensors *etc.* [100-102]. Figure 1.13 shows the discotic liquid crystalline molecule and the model of functionalized gold nanoparticle. It was found that dispersion of this decorated gold nanoparticle into a structure related liquid crystal host does not disturb the nature of the mesophase but only alters the phase transition temperature and significantly improves electrical conductivity [103].
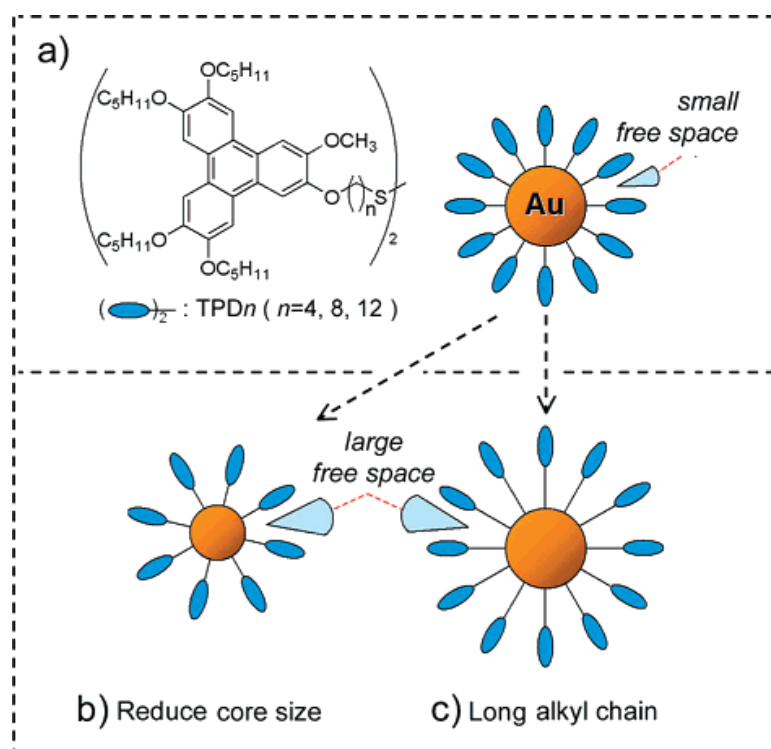
Figure 1.14. Three strategies to construct 1D arrangement of gold nanoparticles: (a) Synthesize molecules with triphenylene ligands (TPDn, n = 4, 8 or 12) and gold nanoparticles stabilized by TPDn; enlarge free space between triphenylene moieties: (b) reduce the core size; (c) or use long alkyl chain.

Ordered arrangements of triphenylene ligand functionalized gold nanoparticles were also realized without any host matrix. In this case the π-π stacking of the ligands plays an important role. By using either smaller gold nanoparticle or longer alkyl chain spacer larger free spaces between triphenylene moieties can be achieved (see Figure 1.14), and these spaces allow easy insertion of triphenylene on adjacent nanopartilces leading to interparticle π-π

interaction. Alternatively, the particle arrangement could also be tuned between stripe-like, hexagonal close packing and disorder by changing solvent polarity using solutions with different methanol to toluene ratios (Figure 1.15). Strong intermolecular π-π stacking interaction can thus be obtained and leads to ordered nanopartilce arrangement [104]. The π-π interaction and solvent polarity were also introduced to self-assemble monolayer-coated magnetic nanoparticles, and pyrene-capped gold nanoparticles to investigate the intermolecular interactions [105-106].
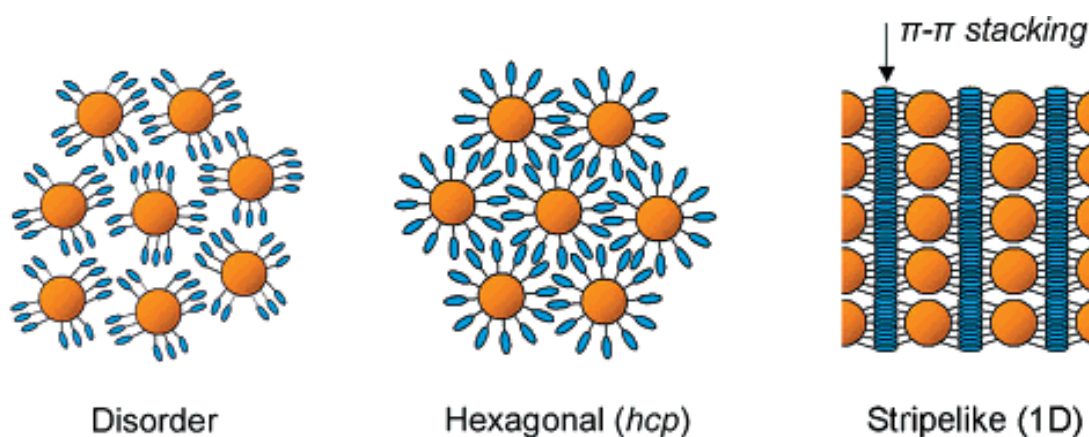
Figure 1.15. The possible arrangement of triphenylene functionalized gold nanoparticles depends on factors of π-π interaction, space around triphenylenes on Au, and solvent polarity (ratio of methanol/toluene) [104].

1.3.2.4 Bent-core mesogen covered GNPs

Bent-core molecule is also called banana-like or bow-like molecule which can develop polar structures even if the molecule itself could be achiral. The compact packing arrangement of such molecules restricts their rotational freedom [107], leading to novel liquid crystal phases that cannot be obtained from traditional rod-like molecules [108-109]. Due to the shape of bent-core molecules, they can pack in a polar fashion giving rise to new smectic mesophases with a long range correlation of lateral dipoles [16]. Since the first report of the unique ferroelectric behaviour of bent-core LC molecules in mid-1990s [109], these molecules have received lots of attention. Thiol terminated bent-core molecules have been used to decorate gold nanopartilces and self-assembled nanocluster arrays were obtained. The self-assembly behaviour was also observed after dispersion of these functionalized gold nanoparticles into liquid crystal host with similar structures. In this case, it was found that the aggregation of the

decorated gold nanoparticles is liquid crystal host dependent. Figure 1.16 shows the synthesis routine and potential application of such gold nanoparticles.

If the bent-core compound, which has more complicated molecular structure and with branches linked at both ends, is connected to gold nanoparticles from its centre rather than from the end, interesting self-assembled results were found. In this case, no long range order of the gold nanoparticles was observed, but the diffused peaks in the small angle X-ray diffraction pattern suggested that the arrangement of the decorated gold nanopartilces might be short range FCC or distorted icosahedral [98, 110].
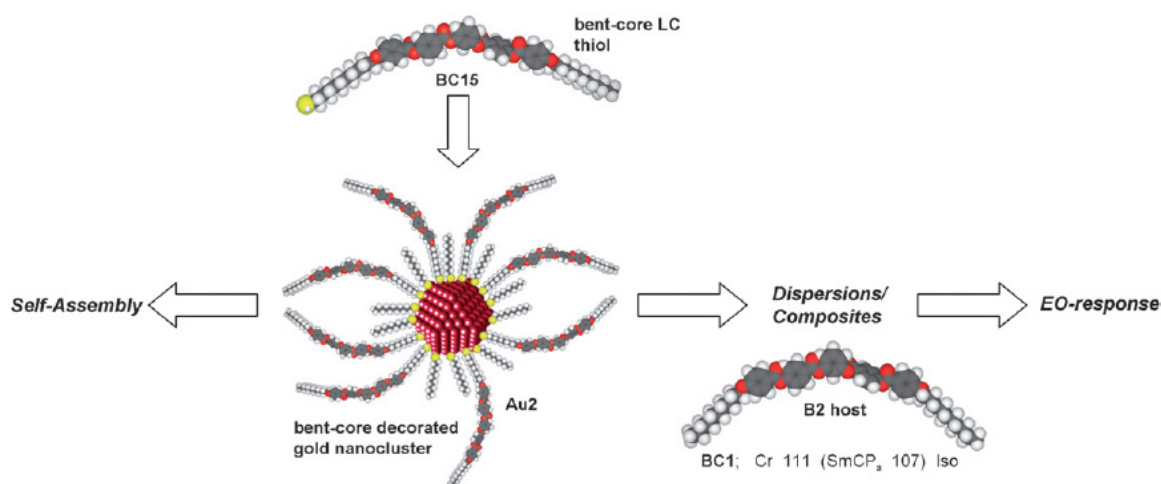
Figure 1.16. Schematic representation of the use of thiol-terminated bent-core compounds in the formation of bent-core functionalized gold nanoparticles, and the potential of using such nanoparticles in dispersions with bent-core LC hosts to alter the bent-core LC host's thermal properties and/or electro-optic response [111].

1.3.2.5 Dendrimer mesogen covered GNPs

A dendrimer is a repeatedly branched molecule which is usually highly symmetric, having three distinct anatomical features, a core, repetitive branch units (dendrons) and terminal groups [112]. The great number of intra-molecular and terminal functional groups can be used as endo- or exo-receptors for binding small size molecules or ions [113-115], and these features have been employed to self-assemble gold nanoparticle-dendrimer composite thin films which have sensor applications [116].
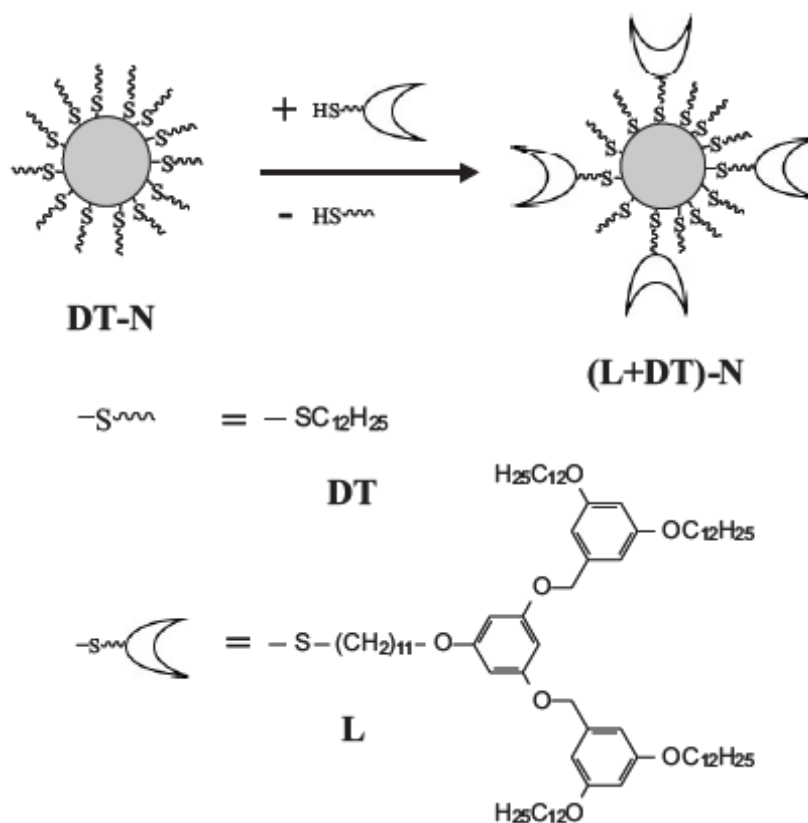
Figure 1.17. Schematic representation of exchange reaction yielding gold nanoparticles (N) covered with surface-protecting groups (dodecanethiol, DT) and dedrimers (L).

By grafting organic dendrimers onto the surface of gold, core-shell decorated gold nanoparticles have been reported for many years [117-119]. The first report that ordered structures of denrimer functionalized gold nanoparticles can be obtained *via* self-assembly method is published in 2007 by B. Donnio *et al.* [95]. 3D cubic structure in bulk and 2D hexagonal lattice on surface were observed. In this study, gold nanoparticles with average diameter of 21 Å and a narrow size distribution ($\sigma = 5$Å) were chosen, as their size is compatible with the length of the second generation dendron used and to favour the induction of mesophases. For the cubic structure (body centred cubic), in each unit cell there are two gold particles, one located at the corner and one at the centre of the cell. The structure of this cubic phase can be described by the space-filling polyhedron geometrical model which consists of the 3D packing of a single type of pseudospherical decorated gold nanoparticles. Each polyhedron composes of eight hexagonal and six square edge faces with gold particle at the gravity centre (see Figure 1.18). Figure 1.17 shows the synthesis process and structures of the dendrimer ligand and the co-ligand. The pre-stabilized gold nanoparticles undergo an

exchange reaction *via* which the dodecanethiol chains (DTs) were partially substituted by dendrons (L)
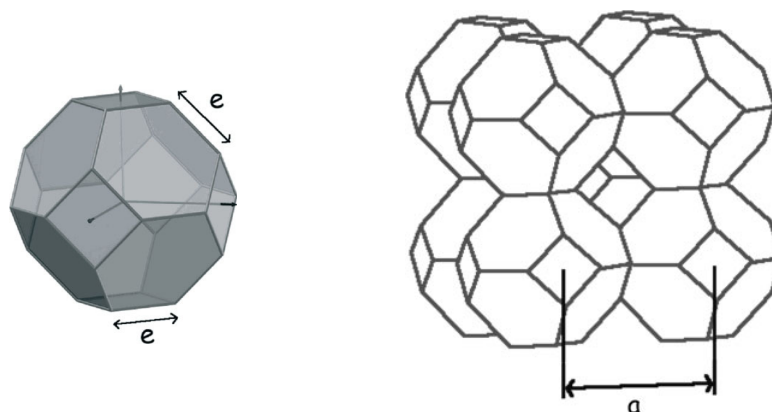
Figure 1.18. Left: The truncated octahedron with the polyhedron edge length of *e*. Rights: Body-centered cubic lattice of *Im*$\bar{3}$*m* symmetry composed of truncated octahedrons. The cubic lattice parameter is *a*.

Dendrimer decorated gold nanoparticles could also promote smectic-like superamolecular organization on carbon-coated copper grids. But in this case the appearance of this smectic-like phase depends on the amount of dendrimers that are loaded on the surface of gold nanoparticles [120].

1.4 Aims and Objectives

The aim of this project is to investigate the self assembled nanostructures formed by pure liquid crystal systems as well as organic-inorganic hybrid systems. Small angle X-ray scattering (SAXS) will be carried out on powder samples with random orientation. These SAXS results can be used to determine the nanostructures including unit cell parameters, plane or space groups *etc*. Additionally, the SAXS technique is also used to obtain diffraction intensities for the reconstruction of electron density map of each structure. To further confirm these structures, grazing incidence small angle X-ray scattering (GISAXS) experiments are carried out, which are performed on thin film samples with improved orientation.

In the first part, T-shaped molecules, each has a rigid biphenyl core, functionalized at both ends by polar 2-diol groups, and a relative long lateral chain composed of aliphatic and fluorinated segments, were investigated. By slightly modifying the lateral chain, different phase sequences were obtained with the change of temperature. Structures of several complex mesophases were solved.

In the second part of this thesis attention will be paid to gold nanoparticle-liquid crystal hybrid system. In this part self assembled nanostructures, formed by liquid crystalline molecule functionalized gold nanoparticles, were determined. Different nanostructures were obtained from this hybrid system, including both 2D and 3D ones. These results were confirmed by simulations on the basis of core-shell models as well as reconstructed electron density maps. Particular attention has been paid to the effect of co-ligand volume on the mode of self-assembly for such systems, and the structural models are further supported by molecular dynamic simulations.

Finally, the morphologies of double layered gold nanoparticles, prepared *via* layer by layer method, were also studied using grazing incidence small angle X-ray scattering technique. The arrangement of gold nanoparticles within each layer and correlation between different layers were investigated. The size of gold nanoparticle, sideway distance and thickness between two gold layers *etc* were determined. The 2D GISAXS pattern was simulated qualitatively with program IsGISAXS, and good agreement between simulated and experimental diffraction patterns has been achieved.

Chapter 2 Experimental Methods

2.1 Basic Theory of X-ray Scattering

X-ray scattering is a non-destructive analytical technique which can reveal information of crystallographic structures and chemical compositions. As we know X-ray is an electromagnetic wave with wavelength at the order of angstrom which is almost the same dimension as interatomic distances in crystals. When an X-ray beam strikes material with a periodic structure, the electrons scatter X-ray into space and diffraction occurs only in some specific directions. Based on diffraction angles and relative intensities of reflections recorded in the diffraction pattern, the structure of material can be determined. According to Bragg's Law X-ray can be considered as being reflected from different sets of parallel lattice planes in a crystal. If a family of lattice planes reflects X-ray and gives a path difference equals integral number of the incident beam wavelength, then diffraction can be observed. As indicated in Figure 2.1 the parallel incident X-ray beam 1 and 2 are reflected by atoms located in two parallel lattice planes, which generate the reflected beam $1^{'}$ and $2^{'}$ with the path difference BC plus BD. Diffraction occurs only if $BC + BD = n\lambda$, which can be expressed as Bragg's Law:

$$n\lambda = 2d\sin\theta \qquad (2\text{-}1)$$

where λ is X-ray wavelength, θ is incident angle of the X-ray beam with respect to lattice plane, d is the interplanar distance (or d- spacing) and integer n is the diffraction order.

Considering the special relationship between d-spacings of lattice planes and the diffraction order, the Bragg equation is normally given by,

$$\lambda = 2d_{hkl}\sin\theta \qquad (2\text{-}2)$$

As comparing two sets of lattice plans with indices (*h, k, l*) and (*nh, nk, nl*) respectively, the *d*-spacing of lattice plans with indices (*h, k, l*) is *n* times that of the other one, *i.e.* the *d*-spacing of the first diffraction order of (*nh, nk, nl*) planes is the same as the *n*th order of (*h, k, l*) planes.
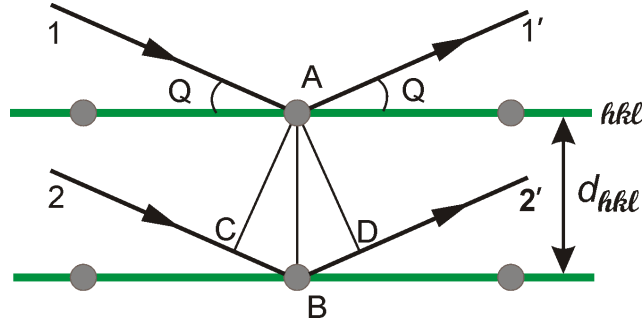
Figure 2.1. The incident X-ray beam scattered by a set of parallel lattice planes.

Figure 2.2a shows a monochromatic X-ray beam with wavelength λ incident on two scatterers, one of which is arbitrarily defined at origin and the other one is separated by vector *r* from it. The incident beam has a unit wave vector S_0 and the scattered beam has a unit wave vector *S*. The path difference between the two waves is give by

$$\delta = r \cdot (S - S_0) \qquad (2\text{-}3)$$

thus the phase difference can be written as

$$\phi = (\frac{2\pi}{\lambda})\delta = (\frac{2\pi}{\lambda})r \cdot (S - S_0) = q \cdot r \qquad (2\text{-}4)$$

where we define a vector *q*

$$q = (\frac{2\pi}{\lambda})(S - S_0) = 2\pi s \qquad (2\text{-}5)$$

$$s = \frac{S - S_0}{\lambda} \qquad (2\text{-}6)$$

25
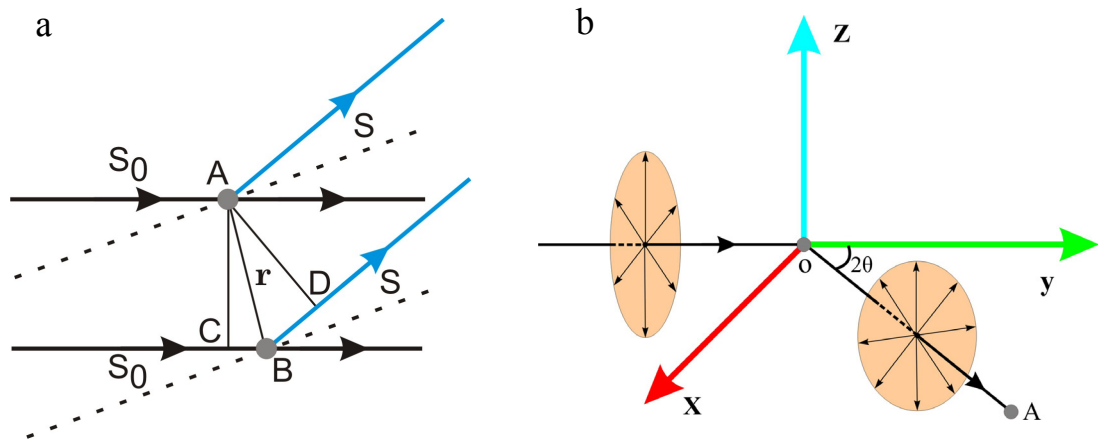
Figure 2.2. a) The incident beam S_0 strikes on two scaterers seperated by distance r, generating scatering beam S. The phase difference between two diffraction points can be expressed by $r \cdot (S - S_0)$. b) An electron located at origin O and the incident beam is along y axis. The scattered intensity at point A not only depends on the distance between it and the electron but also the scattering angle 2θ.

As for the occurrence of diffraction the Bragg's Law is satisfied, , the vector s is perpendicular to the bisector of the angle between vector S_0 and S with its magnitude given by [121-122]

$$s = \frac{2\sin\theta}{\lambda} \qquad (2\text{-}7)$$

Here 2θ is the diffraction angle under the Bragg's Law.

Then the q vector has the same direction as s with magnitude of

$$q = \frac{4\pi}{\lambda}\sin\theta \qquad (2\text{-}8)$$

This q is called reciprocal scattering vector.

When an X-ray beam bombards a charged particle, for example an electron, the electric field of the beam exerts its effect on the electron and makes it oscillating around a mean position. During this motion the electron continuously accelerates and decelerates and then emits electromagnetic wave, which is known as the scattering of X-ray by electron. This scattering happens in all directions around the electron. However, the intensity of scattered beam depends not only on the distance from the electron but also on the scattering angle. Figure 2.2b shows an incident X-ray beam along y direction encountering an electron which located at the origin O. Point A located at distance r away from this electron with an angle 2θ between OA and incident beam. According to the classical scattering theory the scattered intensity at point A can be described as,

$$I_e = I_0 (\frac{\mu_0}{4\pi})(\frac{e^4}{m^2 r^2})p = I_0 \frac{K}{r^2} p \qquad (2\text{-}9)$$

where μ_0 and e are constants, I_0 is the intensity of the incident beam, m is the mass of electron, p is the polarization factor which depends on the polarization of the incident X-ray source and scattering angle. For polarized and unpolarized X-ray beam, the polarization factor p can be expressed separately as:

$$p = \begin{cases} \sin^2\theta \cdots\cdots\cdots\cdots\cdots\cdots polarized\ in\ the\ plane\ of\ scattering \\ (1+\cos^2\theta)/2 \cdots\cdots\cdots\cdots unpolarized \end{cases} \qquad (2\text{-}10)$$

Since the electron distribution of each atom can be considered as electron cloud, if the electron density at a point O is $\rho(r)$ then the total number of electrons in a volume element is $\rho(r)dv$. In this case, based on the amplitude and phase angle, the wave scattered in 2θ direction can be expressed as:

$$F(\boldsymbol{q}) = \int_V \sqrt{I_e}\rho(\boldsymbol{r})\exp(i\boldsymbol{q}\cdot\boldsymbol{r})dv \qquad (2\text{-}11)$$

In the equation the value of I_e is almost constant, which can be ignored for small angle X-ray scattering, as only relative intensity is necessary for structure determination. Therefore, the total wave scattered in 2θ direction by the entire scatterer is

$$F(\boldsymbol{q}) = \int_V \rho(\boldsymbol{r}) \exp(i\boldsymbol{q} \cdot \boldsymbol{r}) dv \qquad (2\text{-}12)$$

Here, the integration is over the whole volume of the scattering body.

For a periodic structure in real space, $\boldsymbol{r}$ can be expressed on the basis of the unit cell vectors i.e. $\boldsymbol{r} = m_1\boldsymbol{a} + m_2\boldsymbol{b} + m_3\boldsymbol{c}$, where the m_1, m_2, m_3 are integers and cover all the lattice points in the real space. Then based on equation 2-6, constructive interference occurs only when $\boldsymbol{r} \cdot \boldsymbol{s} = n$, here n is integer, for all possible $\boldsymbol{r}$ on real lattice. This requires that $\boldsymbol{s}$ satisfies,

$$\begin{aligned} \boldsymbol{s} \cdot \boldsymbol{a} &= h \\ \boldsymbol{s} \cdot \boldsymbol{b} &= k \qquad (2\text{-}13) \\ \boldsymbol{s} \cdot \boldsymbol{c} &= l \end{aligned}$$

where the h, k, l are integers. The diffraction occurs when the equations 2-13 are satisfied. A general solution to these equations is

$$\boldsymbol{s} = h\boldsymbol{a}^* + k\boldsymbol{b}^* + l\boldsymbol{c}^* \qquad (2\text{-}14)$$

where $\boldsymbol{a}^*$, $\boldsymbol{b}^*$ and $\boldsymbol{c}^*$ define a new set of lattice vectors, which are related to the $\boldsymbol{a}$, $\boldsymbol{b}$, $\boldsymbol{c}$ by equations

$$\begin{aligned} \boldsymbol{a}^* \cdot \boldsymbol{a} &= 1, \boldsymbol{a}^* \cdot \boldsymbol{b} = 0, \boldsymbol{a}^* \cdot \boldsymbol{c} = 0 \\ \boldsymbol{b}^* \cdot \boldsymbol{a} &= 0, \boldsymbol{b}^* \cdot \boldsymbol{b} = 1, \boldsymbol{b}^* \cdot \boldsymbol{c} = 0 \qquad (2\text{-}15) \\ \boldsymbol{c}^* \cdot \boldsymbol{a} &= 0, \boldsymbol{c}^* \cdot \boldsymbol{b} = 0, \boldsymbol{c}^* \cdot \boldsymbol{c} = 1 \end{aligned}$$

This new lattice is referred to as the reciprocal lattice. Consequently *s* in equation 2-14 is a reciprocal lattice vector, and integers *h, k, l* are also the Miller indices of a plane (*hkl*) in the real space.

Since each diffracted X-ray that generated from a sample with periodic structure can be described as the sum of the contributions of all scatterers in the unit cell, for a structure, if there are *N* atoms in a unit cell and each of them has a fractional coordinate (x_j, y_j, z_j), there will be *N* scattered waves contributing to the scattering intensity in a given (*hkl)* direction, leading to the structure factor *F* given by

$$F(h,k,l) = \sum_{j=1}^{N} f_j \exp^{2\pi i(hx_j + ky_j + lz_j)} = \sum_{j=1}^{N} f_j \exp^{2\pi is \cdot r} \qquad (2\text{-}16)$$

In this equation, x_j, y_j, z_j are fractional coordinates in real space and f_j is the atomic scattering factor of the jth atom. According to equation 2-16, equation 2-12 can be written as

$$F(h,k,l) = \int_V \rho(x,y,z) e^{2\pi i(hx + ky + lz)} dv = \int_V \rho(x,y,z) e^{2\pi is \cdot r} dv \qquad (2\text{-}17)$$

In X-ray crystallography, the structure factors $F(h,k,l)$ are directly related to the diffraction intensity of the corresponding reflection (*hkl*). The X-ray diffraction intensity measures the square of the structure factor amplitude $|F(h,k,l)|^2$ only, which means from measured reflection intensities we can directly obtain the scalar magnitude $|F(h,k,l)|$ but not the whole information about the structure factor. The lost of the phase angle of the structure factor causes the well known "phase problem" in crystallography. Equation 2-17 indicates that *F* is the Fourier transform of electron density ρ. Since the Fourier transform operation is reversible, the electron density is in turn the inverse Fourier transform of structure factor. Therefore, ρ can be expressed as

$$\rho(x,y,z) = \sum_{h,k,l} |F(h,k,l)| \exp[-2\pi i(hx + ky + lz - \phi_{h,k,l})] \qquad (2.18)$$

where, $\phi_{h,k,l}$ is the phase angle of the structure factor. If a structure is centrosymmetric, then the electron density of $\rho(x, y, z)$ equals $\rho(-x, -y, -z)$ and the structure factor of any given (*h, k, l*) reflection is always real. Consequently, equation 2-18 can be simplified as:

$$\rho(x, y, z) = \sum_{h,k,l} |F(h, k, l)| \cos[2\pi(hx + ky + lz - \phi_{h,k,l})] \qquad (2.19)$$

In this case the phase angle $\phi_{h,k,l}$ should only be 0 or π, and this makes the phase determination much easier due to reduction of possible phase combinations to choose from.

2.2 Small Angle X-ray Scattering

2.2.1 Basic Introduction to Small Angle X-ray Scattering

In this thesis Small Angle X-ray Scattering (SAXS) is the main method used to investigate the liquid crystal structures, complemented by wide angle X-ray scattering (WAXS) method. For liquid crystal, periodic structures only exist at molecular scale rather than atomic scale because of the mobility and flexibility of molecules. Therefore, liquid crystal structures are always characterized by larger unit cells and sharp X-ray diffraction peaks observed at small *q* value, *i.e.* low diffraction angles, when compared to normal crystalline structures. Due to the limitation of minimum incident angle θ, the scattering information in the small *q* value region is not assessable with normal X-ray diffraction techniques. To overcome this problem we need access to lower X-ray diffraction angles, which leads to the Small Angle X-ray Scattering method. As a member of X-ray scattering techniques, SAXS has the unique advantage of delivering structural information of macromolecules ranging from nanometer to micrometer and the scattering intensity could be measured at scattering angle 2θ even very close to 0°. These features enable SAXS to be a powerful tool to explore the material structures involved in this thesis.

As a complementary tool Wide angle X-ray Scattering technique is used to confirm the liquid crystal feature. The scattering signals recorded at wide angle reflect the atomic scale information of the structures. If sharp diffraction peaks are observed in this region it means an

ordered crystalline structure is under investigation; otherwise, diffused scattering would indicate disorder on atomic scale which is a characteristic feature of liquid crystal structures.

2.2.2 The set-up of Small Angle X-ray Scattering

In this thesis both SAXS and GISAXS experiments were carried out using Synchrotron Radiation. As an electromagnetic radiation, the Synchrotron beam is generated by the acceleration of charged particles, normally electrons, in a curved path or orbit through magnetic field. When the high-energy particles are in rapid motion near the speed of light and accelerate, decelerate or change direction, photons are emitted with energies ranging from infra-red to short wavelength X-rays. Therefore, one of the unique properties of synchrotron radiation is its wide energy spectrum, from which beams with different wavelength can be selected for various applications. Another significant character of synchrotron radiation is the extremely intense X-ray it generated. Normally, this intensity is hundreds of thousands of times higher than traditional X-ray obtained from an X-ray tube. The extremely high intensity beam makes the use of synchrotron radiation a time-efficient way to conduct researches, for example the significant reduction of a single exposure time compared with conventional X-ray set-ups. This provides a powerful tool for exploring dynamic chemical reactions or real time monitoring of the system under investigation [123-126].

In the following study, SAXS was mainly used to obtain powder diffraction patterns from samples without orientation. From powder diffraction patterns we can accurately measure diffraction intensities which were then used to reconstruct electron density maps. The schematic drawing and the real X-ray setup are shown in Figure 2.3. The powder samples for SAXS are prepared in glass capillaries with 1mm diameter. During experiment the capillary is fixed on the dedicatedly designed Linkam™ hot hostage and the sample temperature can be controlled within ±0.2 ℃ in precision. Optionally, two ion chambers, one in front and one behind the sample, can be used to monitor the X-ray beam. The extremely intense direct beam is blocked by a beam stop just before the detector to prevent the detector from being damaged as indicated in Figure 2.3.
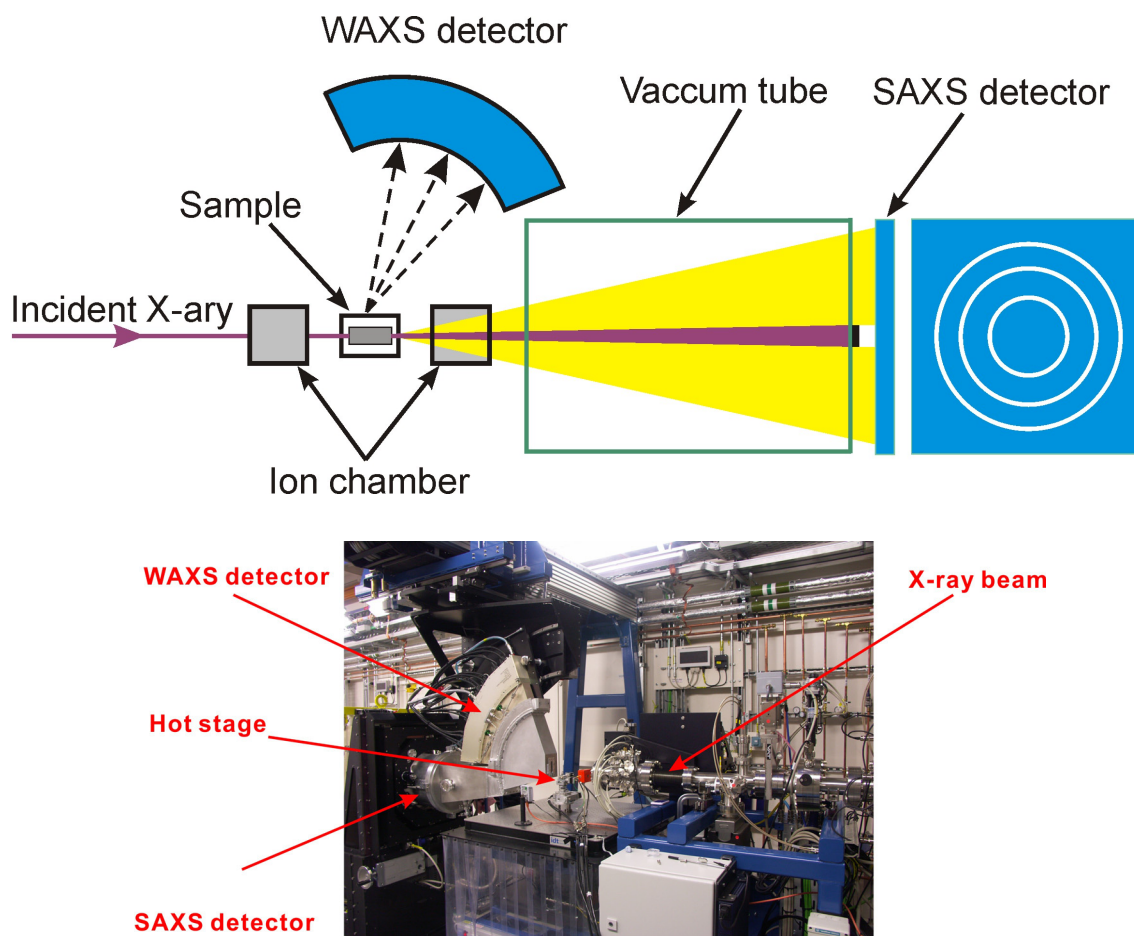
Figure 2.3. Schematically drawing and the real experimental set-up of Small Angle X-ray Scattering at station I22, Diamond, which is also equipped with a WAXS detector.

Two dimensional area detectors, which are especially useful for recording diffraction patterns from samples with known or unknown preferred orientations, are used to collect the scattering signals in small angle region. Thereafter, the 2D powder diffraction patterns are converted to 1D spectra using the FibreFix (CCP13) for measuring diffraction intensities with the help of the Peaksolve^{TM} software. During experiment the striking point of X-ray on the sample can be controlled by rotating or moving the capillary, so that diffraction patterns can be taken at different sample positions. Simultaneously, a curved linear position sensitive WAXS detector is used to collect wide angle scattering information (see Figure 2.3).

SAXS experiments involved in this thesis were carried out at station I22 at Diamond Light Source (United Kingdom) with beam wavelength of 0.995 Å and station ID02 at European Synchrotron Radiation Source (ESRF, France) with beam wavelength of 1.0 Å.

2.3 Grazing Incidence Small Angle X-ray Scattering

2.3.1 Basic introduction to Grazing Incident Small Angle X-ray Scattering

Grazing Incidence Small Angle X-ray Scattering (GISAXS) is a powerful tool for investigating surface, sub-surface and interface problems. As a hybrid technique, GISAXS combines the concepts of both transmission small angle X-ray scattering and surface sensitivity of grazing incident diffraction. For example, it covers form factor, structure factor and scattering geometry close to critical angle of thin film and substrate *etc*. From GISAXS experiments highly intense scattering patterns can be obtained even for very thin films, which are contributed by the sufficient long beam path through the sample at grazing incident angles. So this technique has been widely used for the investigation of electron density distributions on surfaces, sub-surfaces and interfaces [127].

When X-ray interacts with matter, the index of refraction for X-ray can be expressed as [128-129]

$$n = 1 - \delta - i\beta \qquad (2\text{-}20)$$

The parameters δ, β are called refractive index decrement and absorption index, respectively. The order of both δ and β is at bout 10^{-5} or even less, so the index of refraction n for X-ray is very close to but less than 1. This character provides a possibility to probe thin film or surface problems by employing the incident angle of X-ray beam near the critical angle of total external reflection.

When the incident X-ray beam strikes sample at grazing angles close to the critical angle of total external reflection at the air/sample interface, different conditions may occur for the emergent X-ray depending on the relationship between incident angle and the critical angle (see Figure 2.4). If incident angle is smaller than critical angle, the incident beam is totally reflected from the surface (red beam) leaving only a gradually vanishing evanescent wave (purple beam) travelling along the surface. In this case, due to the small penetration depth of

the evanescent wave the scattering pattern only contains the topmost structure information of the thin film. However, if the incident angle is larger than critical angle, then the scattering pattern provides the diffraction information from the bulk of the thin film (blue beam) due the increased penetration depth of X-ray beam.
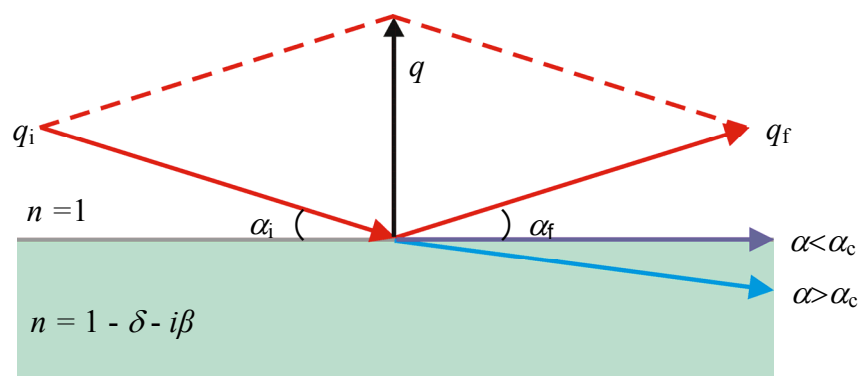
Figure 2.4. The grazing incidence X-ray scattering geometry [130].

Since the thin film sample of GISAXS experiment is prepared on the surface of substrate, therefore the second critical angle for total external reflection at the sample/substrate interface should be taken into account. If the incident angle is smaller than the critical angle at the air/sample surface, only evanescent wave travelling along the top surface of sample and no X-ray beam can reach the sample/substrate interface. If the incident angle is larger than both of the two critical angles, incident beam penetrates the thin film sample as well as the substrate. Consequently, the diffraction pattern comes from the scattering of primary beam. In the case that the incident angle is in between the two critical angles, the scattering pattern comes from both of the primary and the beam reflected from the substrate surface, as a result, the diffraction pattern might be characterized by splitting of diffraction peaks along the perpendicular direction.

Although the grazing incidence small angle X-ray scattering has become a powerful technique in the study of various areas [127, 131], there are only a few studies that using this method in liquid crystalline systems. For example, grazing incidence small angle X-ray scattering has been used to investigate the spin coated and Langmuir-Blodgett (LB) films of phthalocyanines [132], liquid crystalline side chain block copolymers [133], self-assembly of

block copolymer based supramolecules in thin films [134], and thermotropic liquid crystalline molecules of various shapes *etc.* [33]. For a recent review on this topic see [135].

In this thesis we will continue to describe the usefulness of grazing incidence small angle X-ray scattering method in investigations of complex surface aligned periodic liquid crystal structures, and the nanostructures formed by liquid crystalline molecules functionalized gold nanoparticles.

2.3.2 Experimental Set-up

GISAXS experiments were carried out on oriented thin film samples prepared on silicon substrates. During preparation, silicon wafer about 1cm×1cm was first cleaned by acetone followed by rinsing with deionised water and then dried. In the second step, the sample is melt on the surface of one silicon wafer and then covered with another one on top. The molten sample is then slightly pressed in between two silicon wafers before the two are separated. This is an easy and effective way to prepare oriented thin film sample for GISAXS experiments.

In this thesis GISAXS method was used to help index diffraction patterns and to confirm the structures decided from SAXS experiments. On the other hand, due to the additional structure information provided by the diffraction pattern of sample with special orientation, GISAXS is also a powerful tool used in this thesis to determine complex self-assembled structures which otherwise could not be solved easily based on only the SAXS results. GISAXS experiments were performed at two different Synchrotron Stations, one is the XMaS beamline at the European Synchrotron Radiation Facility (ESRF, France) with a MarCCD detector, and the other one is at station I16, Diamond Light Source (Oxford, United Kingdom) with a Pilatus 2M detector.

The schematic drawing and the real GISAXS experimental set-ups are shown in Figure 2.5. Samples were placed on a hot stage which is mounted on a goniometer with three free rotation axes. A thermocouple connected to the hot stage and a Eurotherm[TM] temperature controller was used to monitor and control the sample temperature during experiments. The sample position and X-ray incident angle with respect to the thin film surface can be easily controlled

via the goniometer. To reduce the background scattering, a helium gas filled tube was used in front of the detector. Direct and reflected beams were blocked by employing a beam stop which was attached to the back window of the tube. The scattering signals were recorded with an area detector.
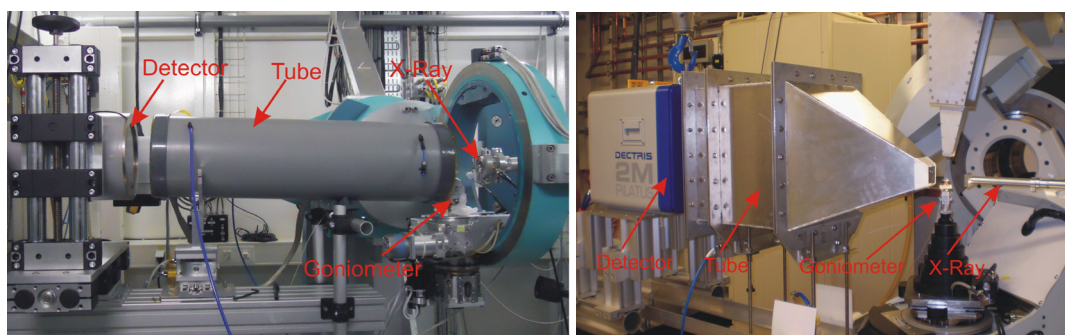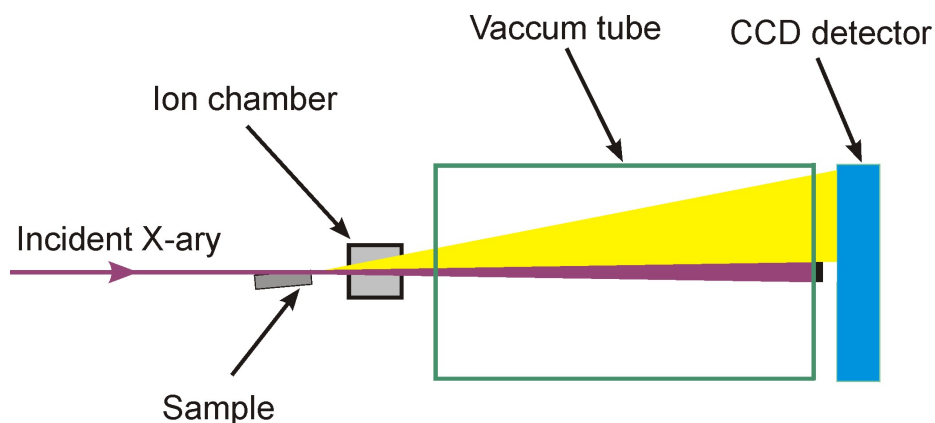
Figure 2.5. Sketch map (top) and the real experimental set-up for grazing incidence small angle X-ray scattering experiments at the XMaS, ESRF (bottom left) and I16, Diamond (bottom right).

2.4 Polarized Optical Microscopy

As one of the essential tools to characterizing mesogenic materials, Polarized Optical Microscopy (POM) is widely used to determine both the phase transition temperature and the phase type. This is realized by investigating the temperature dependent textures between crossed polarisers. A picture of the microscope (Olympus BX-50) used in this thesis is shown in Figure 2.6a, and a schematic diagram of the microscope with the names of main parts indicated as shown in Figure 2.6b.

a

b

Camera

Ocular

Analyser

Lambda plate

Objective

Hot stage and
sample

Rotation sage

Condensor

Polarizer

Mirror

Focus
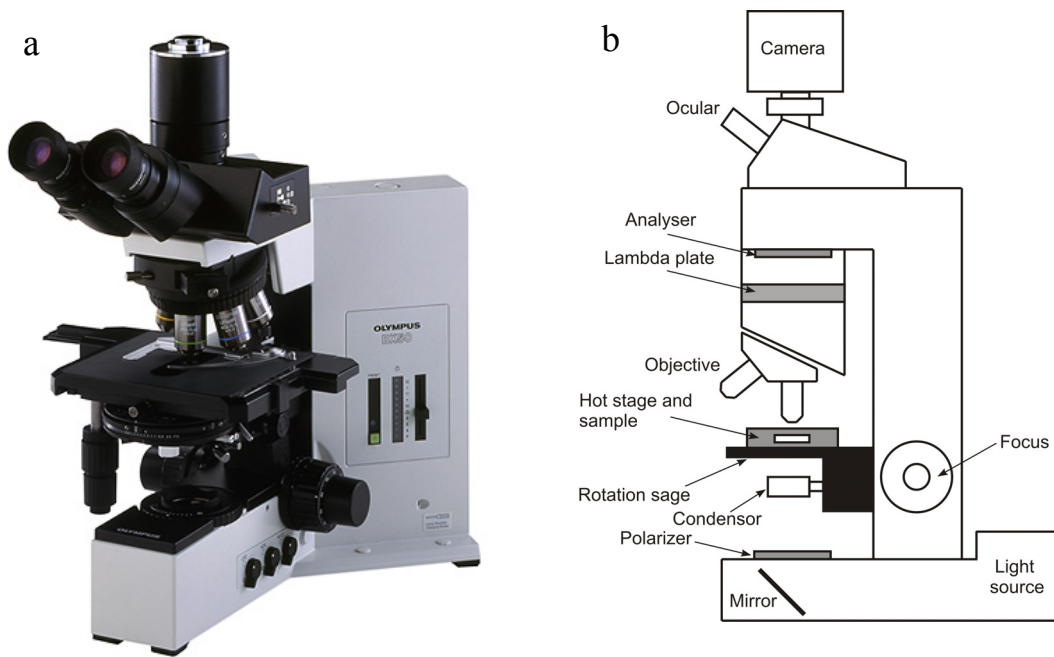
Light
source

Figure 2.6. a) The polarized optical microscope used in this thesis (Olympus BX-50), and b) its schematic diagram [136].

Light can not transmit through crossed polarizers, unless optically anisotropic (or birefringent) samples are inserted between the polarizer and the analyzer. In this case the polarization state of the light will be changed by the samples, so that it will pass through the analyser. Liquid crystals are such anisotropic materials, *i.e.* in liquid crystals the index of refraction is dependent of the polarization direction of the incident light beam. Most liquid crystal phases are uniaxial, in which case the incoming light beam will be split into two components. These two light beams are perpendicular to each other in polarization and propagate with different velocities through the birefringent medium. In the simplest situation where the incident beam is perpendicular to the sample surface, such as the condition used in normal POM study, the two rays will carry on in the same direction with a phase difference between them. If the two rays experience different indices of refraction n_o and n_e respectively, then the retardation δ between them is given by [136]

$$\delta = \frac{2\pi}{\lambda}(n_e - n_o)d \qquad\qquad (2\text{-}21)$$

Where λ is the vacuum wavelength of incident light beam and *d* is the beam travel distance in the medium.

Normally, the incident linearly polarized light can be converted to elliptically polarized light after encountering birefringent liquid crystal, leading to a component that can pass through the crossed analyser. As a result, the sample appears bright. The measured intensity I after light going through a birefringent material is given by [137]

$$I = I_0 \sin^2 2\theta \sin^2 \frac{\delta}{2} \qquad (2\text{-}22)$$

where I_0 is the intensity of light emerging from the polarizer, θ is the angle between the polarizer and the optical axis of anisotropic sample. As equation 2-22 indicates, the intensity is dependent of the angle θ, which means the brightness changes when rotating the sample. For example, in homeotropically oriented nematic or SmA phase $\theta = 0°$ and the measured intensity is always zero, while for uniform planar alignment the intensity is maximum for $\theta = 45°$ and minimum for $\theta = 0$ and $90°$.
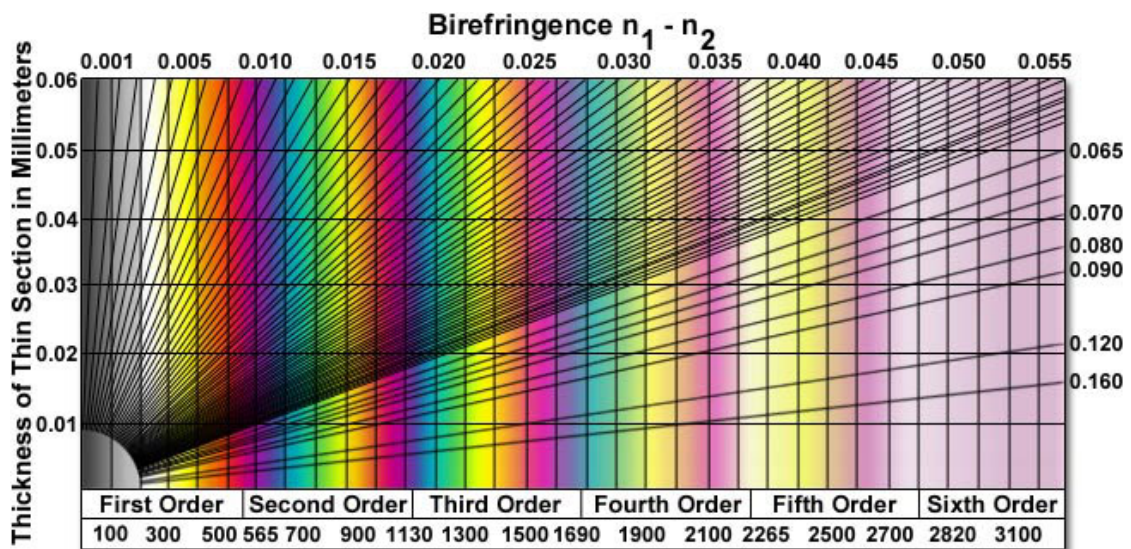
Figure 2.7. The interference colour chart. The interference colour can be correlated with the actual retardation (bottom horizontal axis), thickness (left hand vertical axis), and birefringence (top and right hand axes) of the sample. If two of the three variables are known, the remaining one can be determined by drawing a line from the lower left hand corner to the upper and right hand boundaries [138].

In order to control the background illumination or improve the contrast as well as visibility in weakly birefringent samples, and to figure out the orientation of the molecules by examining

the slow and fast X-ray travel directions in the sample, a retardation plate was introduced to investigate liquid crystal textures [139]. This retardation plate is composed of optically anisotropic materials, for example quartz, mica *etc*, and is placed above the objective rear focal plan but beneath the analyser. By convention, the direction of this retardation plate will be northeast-southwest and this direction will be marked as "slow", which means due to the existence of retardation plate the light beam polarized along this direction will be slowed down. In the case of POM using an incandescent source, light of different frequencies are present at the same time causing the appearance of interference colours. For all possible retardations, the interference colours can be plotted on a chart as shown in Figure 2.7. Depending on the amount of retardations, these interference colours are divided into "orders" with the end of each order marked by a red colour representing one full wavelength retardation. The first order starts with black, followed by yellow and orange hues and ends with red at about 550 nm. The second order has intense blue, green, yellow, orange, and finally red at about 1100 nm. So in the case of a 1-λ retardation was introduced, if this direction is parallel to the slow direction of the sample, then additional retardation which equals to one wavelength (about 550 nm) will be produced for the wave vibrating in the slow direction. Consequently, the first-order gray interference colour between crossed polarizers may present second-order blue. On the contrary, if the slow direction of retardation plate is parallel to the fast direction of the sample, then the previously fast wave will be slowed down by one wavelength and the previously slow wave will overtake it. In this case, the interference colour may become first-order yellow.

Therefore, with the help of retardation plate the fast and slow direction in the specimen can be determined by comparing observed interference colour with the colour chart. Since the fast and slow axes correspond to the perpendicular and parallel directions of the rod-like aromatic cores of the T-shaped liquid crystalline molecules respectively, the POM textures thus obtained can provide us with more details of molecular arrangement in the liquid crystal phase.

The microscope used in this thesis is an Olympus BX-50 which is equipped with a retardation wedge, with choices of retardation from 1λ to 4λ. The light source is incandescent. A digital camera and the Image-Pro Plus software from MediaCybernetics are used to capture and process the liquid crystal textures.

2.5 Molecular Dynamics Simulation [140]:

Molecular dynamics simulation is a computational method which calculates the time dependent behaviour of a molecular system. This method is widely used to investigate the microscopic interaction behaviour between atoms and molecules [141-143]. During this simulation the conformation, thermodynamic properties and dynamic behaviour of molecules in a system are investigated by calculating the motion of all atoms contained, including position, velocity and acceleration *etc*.

In this thesis molecular dynamic simulation is used to evaluate the models proposed on the basis of reconstructed electron density maps. The simulation was carried out using Materials studio (Accelrys), which contains advanced materials simulation and modelling tools, and is used in various research areas ranging from chemistry, material and engineering *etc*. For an entire modelling and simulation process three main steps are involved.

First of all, a starting crystal structure is built, using cell parameters and the number of molecules per unit cell as determined from experimental results. For structures of mesogen functionalized gold nanoparticles, each unit cell contains one gold particle which is covered by a certain number of mesogenic ligands and co-ligands. For the structure of *c2mm* phase formed by T-shaped molecules, the simulation was based on a hypothetic 3D structure with the third dimension equals to the thickness of a single molecule layer *i.e.* the diameter of the rigid aromatic core, which is approximate 0.45 nm.

The second step is geometry optimization. Since the modelling process in the first step often creates molecules in a high energy configuration and such un-optimized structure may lead to erroneous simulation results. So in this step energy and geometry optimization is applied to the unit cell to minimize the strain energy of molecules, and this is accomplished by altering the atom positions to optimal geometry. This process is monitored by reducing the magnitude of calculated forces and stresses until they become smaller than the defined convergence tolerances. Therefore, the final optimization quality can be controlled by presetting the convergence tolerance parameters at different levels.

Finally, dynamics simulation is conducted with repeat heating and cooling cycles to further reduce the stress on molecules and to optimize conformation. Normally, during this process the Universal Forcefield [140, 144] is used with the thermodynamic ensemble of NVT which means constant volume/constant temperature dynamics. 30 temperature cycles were used running between the initial temperature 300 K and the mid-cycle temperature 700 K. Again different simulation quality levels, annealing cycles and temperature ranges can be selected.

2.6 Analysis Procedure

To determine the structure of a given phase several steps will be involved. First of all, the diffraction pattern needs to be indexed. Powder sample composed of numerous very small crystallites can be considered as completely randomly oriented, so normally powder diffraction pattern is characterized by a series of continuous concentric rings. Generally speaking, the more rings observed the more structure information can be obtained from powder diffraction pattern, as each of them corresponds to a certain set of lattice planes. However, this information is only confined on the q value of each ring. For structures with large unit cells there might be many diffraction rings in small q value region with a narrow q-range. This may cause the overlap of rings which are generated from lattice planes with almost equivalent interplanar distances. What's more, the presence of the extra reflections due to the contamination or impurity of sample will also make the interpretation of diffraction patterns difficult or even impossible. These problems can often be solved with the help of GISAXS method. Generated from thin film sample with improved orientation, GISAXS patterns are characterized by isolated spots rather than a series of continuous rings. These spots not only carry the information of q values but also the positional information of each reflection in the reciprocal space. Therefore, the combination of SAXS and GISAXS is an effective way to index diffraction patterns and determine material structures, especially for complex ones. With the diffraction pattern indexed, the unit cell parameters can be determined and then space group can be identified by combining these information with the extinction rules which could be found in the *International Tables for Crystallography.*

With the determined structure information we can progress to reconstruct an electron density map of the structure. In this step diffraction intensity of each observed reflection is required and this can be accomplished by fitting 1D powder diffraction spectra with the Peaksolve$^{\text{TM}}$

software, which is a powerful tool for intensity integration and resolving overlapping peaks. To get rid of the domains effect on the intensities, the sample containing capillary was often rotated during the collection of powder diffraction patterns. In some cases, to minimize the background effect contributed by the capillary itself, a diffraction pattern of empty capillary was also recorded for background subtraction later on.

An electron density map of each structure is reconstructed using the unit cell information, space group and diffraction intensities. If the origin of the structure is also an inversion centre, which is commonly the case for liquid crystal systems, then the quantitative calculation of electron density distribution can be based on equation 2-19, where the (h, k, l) in the equation is the index of each reflection observed in diffraction pattern, (x, y, z) is the fractional coordinate of a motif in the unite cell determined by the space group, $\phi_{h,k,l}$ is phase angle which can't be obtained directly from X-ray diffraction pattern and is known as "phase problem" in X-ray crystallography. So the determination of a correct phase combination is a crucial step to obtain a reasonable electron density map.

Generally speaking, if the number of reflections used to reconstruct electron density map is n, there will be 2^n possible phase combinations. However, these phase combinations can be reduced by half due to the phase inversion, for example the high and low electron density regions are simply reversed for phase combinations (0000) and ($\pi\pi\pi\pi$). Further reduction can be achieved by *e.g.* arbitrary choice of the lattice origin.

In this thesis several methods were used for reliable selection of the correct phase combination. First of all, for a centrosymmetric structure the possible phase angle of $\phi_{h,k,l}$ is restricted to either 0 or π, which makes it possible to generate electron density maps from all possible phase combinations, and selection is carried out after a thorough comparison between these maps. This selection is based on the physical merits of electron density map and the existing knowledge about the system, for example the symmetry of the lattice, the dimensions of molecule and the electron distribution within each molecule *etc*. Normally in liquid crystal system the right phase combination should always give well defined high and low electron density regions [145]. The quality of the reconstructed electron density map can also be monitored using the electron density histogram which is a comparison of the volume fraction that located at different electron density regions. To obtain this volume fraction *vs.* electron

density histogram, the unit cell is divided into a huge number of small volume elements and at the mean time the calculated electron density is also divided into a certain number of segments (which can be controlled manually but usually this value is set to be 100) between minimum and maximum values. The program then calculates the number of volume elements within each intensity interval and then plots the histogram of volume fractions against electron density. For a given molecule, we can calculate the volume and electron density of each part of it with the help of Materials Studio (Accelrys) or Cerius2 software. So for an ideal structure, from the histogram we can identify the boundaries between high, medium and low electron density regions and this is also one of the basic rules to evaluate reconstructed electron density maps.

Since the lower order reflections determine the main feature of the electron density map, for structures with many reflections appeared in diffraction pattern, electron density maps can be first reconstructed using only the low order ones with all the possible phase combinations. The best one is then selected based on the merits of the reconstructed maps. With phase angles of low diffraction orders fixed, the phases of high diffraction orders can be determined in a similar way by adding them to the reconstruction.

Another method employed to determine the phase combination is theoretical calculation of the form factors. The simulation of diffraction intensities was carried out on mesogen functionalized gold nanoparticles, as in this case the diffraction intensity can be considered as the product of structure factor $S(q)$ and the form factor $[F_{nano}(q)]^2$ of nanoparticle, taking a core/shell model to describe the decorated gold nanoparticle. The structure factor is determined by the lattice, while the form factor amplitude $F_{nano}(q)$ of a core-shell model can be expressed as [146]:

$$F_{nano}(q) = 3(\rho_{gold} - \rho_{org})V_{nano}[\sin(qR) - qR\cos(qR)]/(qR)^3 \quad (2\text{-}23)$$

Where ρ_{gold}, ρ_{org} are the electron density of gold and the surrounding organic molecules respectively, q is reciprocal space scattering vector and R is the radius of gold core. The detailed information about this equation can be found in appendix A1. Considering the thermal fluctuation of gold nanoparticle position, a Debye-Waller factor was included during simulation. Therefore, the final expression of intensity in terms of form factor is given by

$$I(q) = M(q)S(q)\exp(- <u^2> q^2/3)[F_{nano}(q)]^3 \qquad (2\text{-}24)$$

Where $<u^2>$ is the mean square displacement of the centre position of gold nanoparticle, and *M(q)* is multiplicity of the reflection. According to this calculation the structure factor phase angle of each reflection can be obtained directly.

Based on reconstructed electron density maps it is possible to propose a structure model to describe the arrangement of molecules in each mesophase. As the electron density maps clearly show the electron density distribution within each structure, and this distribution is caused by the electron density difference between different parts of molecule, for example in T-shaped molecule, the flexible lateral chain, the rigid aromatic core and terminal groups possess high, medium and low electron density respectively. By comparing the electron density distribution in a single molecule with the reconstructed electron density map we can know how the molecules arranged in the unit cell and then structure model can be proposed. Finally, for some mesophases, molecular dynamic simulation is used to evaluate the models that are proposed on the basis of reconstructed electron density maps.

Chapter 3 Mesophases Formed by T-shaped Molecules

3.1 Introduction

Traditional liquid crystal phases are formed by molecules with simple shapes, for example rod-like or disk-like molecules. Rod-like molecules prefer to organize into layer structures and form smectic phases, while for disk-like molecules columnar phases are the most dominant structures. If we modify the conventional liquid crystalline molecules by adding extra functional groups to different positions of the rigid cores, for example T-shaped molecules, then the symmetry and free rotation of the molecules (rod-like) along their long axes will be restricted, and consequently different liquid crystal phases can be obtained [147]. T-shaped ternary bolaamphiphilic molecules are composed of three incompatible parts: a rod-like core, two terminal polar groups and a lateral chain. Due to the incompatibility of different molecular segments, the new liquid crystal phases formed by these molecules are dominated by polygonal cylindrical structures. In such structures the rigid rod-like cores that form the walls of these cylinders are connected by the hydrogen bonding networks provided by the polar groups, and the interior space of each cylinder is filled by the lateral chains. The balance between the space required by the lateral chains and the circumference provided by the cylinder frame determines the shape of these cylinders, leading to structures with different symmetries [48, 54, 148].

3.2 Compounds

In this chapter, some novel liquid crystal structures formed by T-shaped ternary bolaamphiphiles will be discussed. The basic molecular structure of these compounds is shown in Figure 3.1, in which the rigid biphenyl core of the molecule is terminated by polar 1, 2-diol units. A laterally attached relatively long chain R composed of aliphatic segment (spacer) and fluorinated end is positioned off-centre from the biphenyl core. Normally these molecules form honeycombs of different shapes at low temperature depending mainly on the lateral chain length. For example square, pentagonal, hexagonal phases, and giant hexagonal phases which contain 8 molecules and 10 molecules on each cylinder cross section, have been

found [48, 54, 149-150], as discussed in chapter one. In these structures the rigid cores of molecules are perpendicular to the cylinder axes with the lateral chains filling the inner space. At high temperatures these T-shaped molecules exclusively form lamellar phases. However, in this thesis more complicated phases which were observed in the region between honeycomb and lamellar phases will be discussed. The sample name, the constituents of lateral chain *R* and the phase behaviour of each sample are listed in Table 3.1. By only slightly modifying the lateral chain structure, different liquid crystal phases have been obtained including both 2D and 3D structures. These liquid crystal structures were investigated *via* small angle X-ray scattering and grazing incidence small angle X-ray scattering methods.
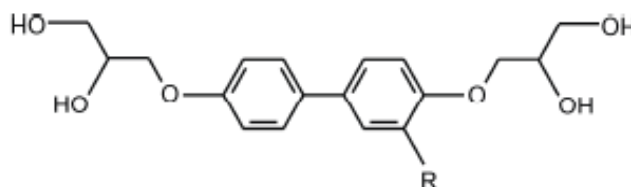
Figure 3.1. The basic molecular structure of T-shaped bolaamphiphiles. *R* represents the lateral chain which was varied during this study.

For sample T-C_1($OC_{11}F_8$), the relatively long lateral chain of the molecule is composed of a branched hydrocarbon spacer with a methyl branch and a perfluorinated end segment. Different mesophases were found at different temperatures according to small angle X-ray scattering and grazing incidence small angle X-ray scattering experiments. A new mesophase was found (new high-T phase) between the low temperature *c2mm* phase and high temperature lamellar phase. The phase transition temperature is shown in table 3.1.

For sample T-C_3($C_{11}F_8$), the lateral chain of the molecule was modified slightly. In this compound the oxygen in the hydrocarbon spacer of the lateral chain was removed, and the -CH_3 branch of the lateral chain was changed to -C_3H_7 group. Three mesophases including two new ones were confirmed in this sample. The new phase found between 65 ºC and 74 ºC was called the new low-T phase. This phase was followed by another new phase, which turned out

to be the same new high-T phase as found in sample T-C_1($OC_{11}F_8$), at slightly higher temperature between 75 ºC and 84 ºC. Between 85 ºC and 95 ºC a lamellar phase was found.

Table 3.1. Name of each sample, components of lateral chains and phase behaviour of each compound including phase sequence and phase transition temperatures.*

Samples	Lateral chain R	Phase transition(T/ºC)
T-C_1($OC_{11}F_8$)	O(C_2H_3)(CH_3)-O(CH_2)$_{11}C_8F_{17}$	Cr 53 Col$_{rec}$/$c2mm$ 68 New high-T phase 93 Lam 138 Iso
T-C_3($C_{11}F_8$)	O(C_2H_3)(C_3H_7)-(CH_2)$_{11}C_8F_{17}$	Cr 65 New low-T phase 74 New high-T phase 84 Lam$_{Sm}$ 95 Iso
T-C_4F_{10}	O(CH_2)$_6C_{10}F_{21}$	Cr 60 Undecided phase 72 New high-T phase 102 Lam$_{Sm}$ 166 Lam$_{Iso}$ 195 Iso

* Abbreviations: Cr=crystalline solid; Colrec/$c2mm$= rectangular columnar phase with plane group $c2mm$; New high-T phase = new phase found at relatively high temperatures; New low-T phase = new phase found at relatively low temperatures; Lam$_{Sm}$ = lamellar smectic phase; Lam$_{Iso}$ = lamellar isotropic phase; Lam = lamellar phase; Iso = isotropic liquid state.

Comparing with the first two samples, for T-C_4F_{10} the entire lateral chain is shorter even though the fluorinated segment is slightly longer, as the aliphatic segment here is much shorter than those of the other two compounds. Also there is no short branch attached to the hydrocarbon spacer. Three different mesophases existing at different temperatures were confirmed by experimental results. The structure of the lowest temperature phase, observed between 60 ºC and 72 ºC, has not been determined yet. The high temperature lamellar phase was observed between 102 ºC and 195 ºC, and between these two is a new mesophase which is the same new high-T phase as found in the other two samples.

3.3 Results and discussion

According to SAXS and GISAXS experimental results, each of these samples has three mesophases existing at different temperatures. As the molecular structures of these compounds are quite similar to each other, the obtained phase sequences of these samples can be easily related to each other. At low temperature a 2D rectangular columnar phase with plane group *c2mm* and a new low-T phase were found in sample $T-C_1(OC_{11}F_8)$ and $T-C_3(C_{11}F_8)$, respectively. For sample $T-C_4F_{10}$ the low temperature mesophase has not been decided yet. However, the new mesophase (new high-T phase) at higher temperature was found to be the same in all of the three samples and it is followed by lamellar structures with further increase of temperature. Details of each structure will be discussed in the following sections.

3.3.1 Low Temperature Rectangular Columnar Phase

The molecular structure of compound $T-C_1(OC_{11}F_8)$ is shown in Figure 3.2a. Different mesophases were found at different temperatures as indicated in the SAXS diffractograms (Figure 3.2b). These SAXS diffractograms were recorded at a continuous cooling run with cooling rate of 2 ℃/min and the interval between each frame is 30 seconds. Three mesophases appeared one after another with the continuous changing of temperature in the range between 138 ℃ and 53 ℃ before it crystallizes.

1D SAXS spectrum of the low temperature rectangular columnar phase, recorded at 61 ℃, is shown in Figure 3.2c. The sharp diffraction peaks observed indicate highly ordered arrangement of molecules, and are indexed to a 2D rectangular lattice with plane group *c2mm*. The unit cell parameter *a* and *b* are determined to be 82.8 Å and 66.9 Å, respectively. The observed and calculated *d*-spacings of diffraction peaks are compared in Table 3.2, and a good agreement between these two is achieved. To confirm this indexing scheme, grazing incidence small angle X-ray scattering experiments were carried out on an oriented thin film sample which was prepared on silicon substrate. Since a GISAXS pattern can provide additional positional information of each reflection in reciprocal space, it is easier and more reliable in determining the lattice and symmetry of a crystal structure. The GISAXS pattern of

this mesophase is shown in Figure 3.2d and it confirms that indeed it has a rectangular lattice. The same reflections as in powder SAXS pattern were observed, and the 2D rectangular lattice (white grid) can be easily recognized and reflections readily indexed in the GISAXS pattern (Figure 3.2d)
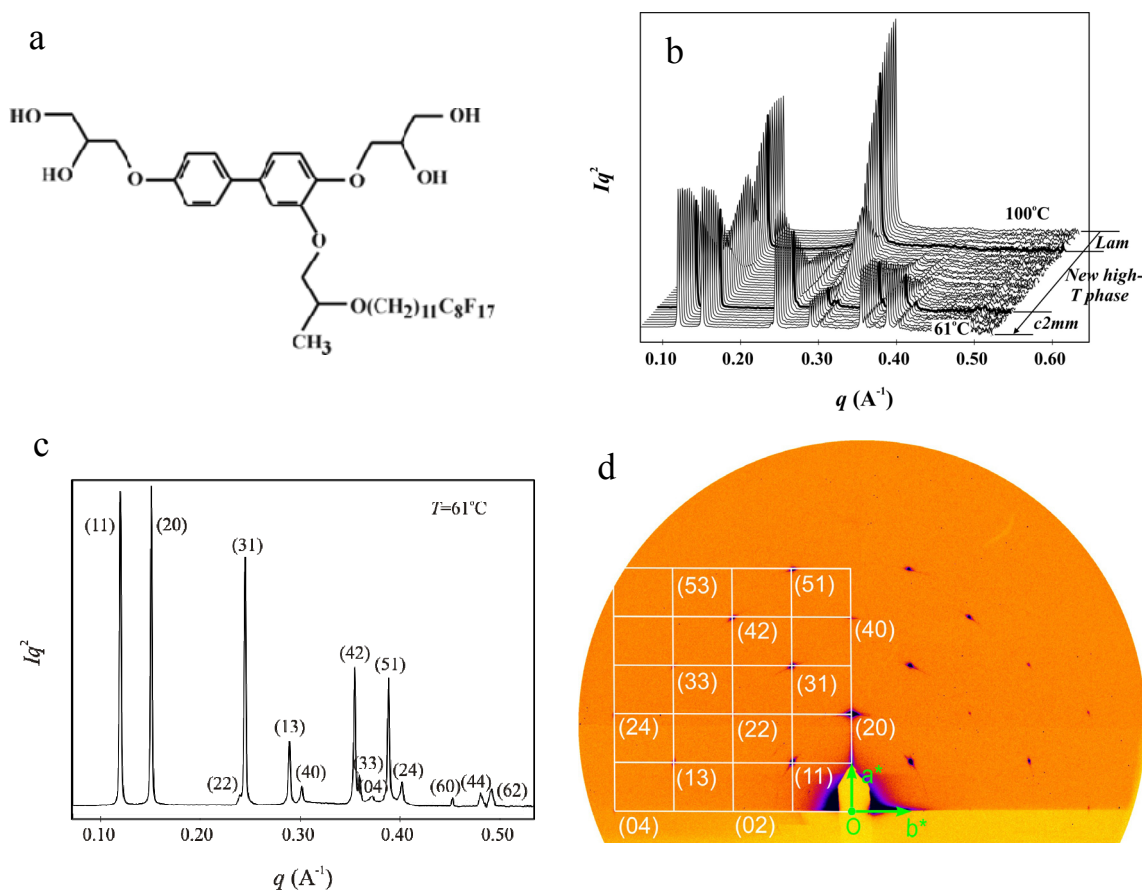
Figure 3.2. a) Molecular structure of compound T-$C_1(OC_{11}F_8)$. b) Powder diffractograms recorded by SAXS at continuous cooling run with cooling rate of 2 °C/min. c) SAXS pattern and d) GISAXS pattern of the 2D $Col_{rec}/c2mm$ phase recorded at 61 °C.

Reconstruction of electron density map was carried out using the diffraction intensities and phase angles given in Table 3.2. The diffraction intensity of each reflection was measured from the high-resolution powder diffraction pattern (Figure 3.2c). In the reconstructed electron density map (Figure 3.3a) the electron density is visualized by spectral colours, where the red and purple represent the lowest and the highest electron density, respectively as shown by the colour bar on the left hand side of the map. This electron density map clearly

shows the columns with elliptical cross sections. The central high electron density region (blue/purple) of each column is contributed by the fluorinated segments of the lateral chains. This high density region is surrounded by a shell of low electron density as presented by the yellow/red colours which contains the aliphatic spacers of the lateral chains. The high electron density cores and the low electron density shells are walled off from their neighbours by green colour regions which indicate the medium electron density areas contributed by the biphenyl cores and diol groups of the molecules.

Table 3.2. Experimental and calculated *d*-spacings, relative integrated intensities, and phases used in the reconstruction of electron density map for the Col$_{rec}$/*c2mm* phase. All intensity values are Lorentz and multiplicity corrected.

(*hk*)	$d_{obs.}$ (Å)	$d_{calc.}$ (Å)	*I(hk)*	$\varphi(hk)$
(11)	52.0	52.0	55.3	0
(20)	41.4	41.4	100.0	0
(22)	26.1	26.0	2.8	0
(31)	25.6	25.5	41.5	0
(13)	21.6	21.5	12.3	π
(40)	20.7	20.7	6.2	0
(42)	17.6	17.6	24.7	π
(33)	17.4	17.3	5.3	π
(04)	16.7	16.7	3.2	0
(51)	16.1	16.1	21.4	π
(24)	15.5	15.5	3.9	0
(60)	13.8	13.8	2.4	0
(44)	13.0	13.0	2.3	0
(62)	12.7	12.8	4.0	π
a = 82.8 Å, *b* = 66.9 Å				

Judging by the size of the column cross section and the dimension of the molecules, the honeycomb has a shape of a stretched hexagon in which four sides have approximate twice the length of the other two. This can be further confirmed by the details of the reconstructed

electron density map. As we seen within the medium electron density area (green regions) there are slightly higher electron density areas (light blue regions as indicated by the ellipses on the top-right corner of Figure 3.3a) which are contributed by the biphenyl cores of the molecules. There are two of these local maxima along the longer sides but only one along the shorter sides of the stretched hexagonal cross section. Therefore, totally there are ten molecules in each of these column cross sections. Moreover, the electron density of the positions occupied by the hydrogen-bonding networks is slightly reduced, for example, positions at the nodes of the hexagons and in the middle of the longer sides. It was found in a previous publication that in this structure the biphenyl cores of the molecules are perpendicular to column axis [150]. This arrangement is additionally confirmed by the size of the unit cell and the dimension of the molecules. As the average diameter of the biphenyl units is about 4.5 Å, the number of molecules in a hypothetical 3D unit cell is defined by the lattice parameters and a height of molecule thickness (4.5 Å). According to calculation there are approximately 19.2 molecules in each unit cell (see appendix A4). Therefore, there are 10 molecules arranged on the circumference around each of the core-cell columns. Considering the packing style of these columns, there should be on average two molecules side-by-side in the wall of polygonal honeycomb. This result is in line with the width of this area which is calculated to be 9.0-10.0 Å, corresponding to approximately twice the average diameter of a biphenyl unit (4.5 Å). Figure 3.3b shows a snapshot of a molecular dynamics simulation after annealing using the experimental unit cell with periodic boundary conditions and a height of single molecular layer; the simulation result confirms the efficient space filling and phase separation achieved in this structure.

A sketch of the organization of molecules in this mesophase is shown in Figure 3.3c and Figure 3.3d. The blue column centre and the green shell are formed by the fluorinated ends and aliphatic spacers of the lateral chains respectively. The yellow columns are formed by the polar groups of the molecules, and the white rods represent the rigid biphenyl cores. As discussed above, the circumference of each stretched hexagonal is composed of 10 molecules, where the four longer sides each contains a pair of end-to-end connected molecules while the two shorter sides each contains one. The nodes of the hexagons and the middle of the longer sides are occupied by the hydrogen-bonding networks which form separate columns. Molecules belong to neighbouring columns are arranged side by side in the walls of the polygonal honeycombs.
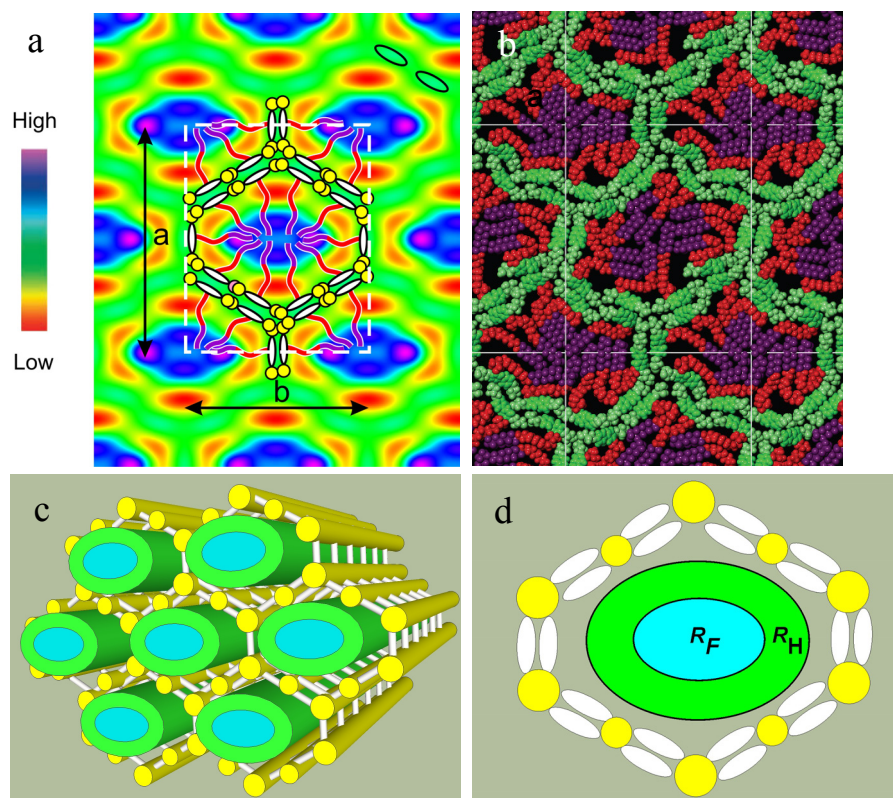
Figure 3.3. a) Reconstructed electron density map of the $Col_{rec}/c2mm$ phase found in sample $T-C_1(OC_{11}F_8)$. The colour scale is shown on the left. b) Snapshot of molecular simulation. The blue/purple = perfluorinated end groups R_F, red = aliphatic chains R_H, green = biphenyl and diol groups. c) and d) sketch of the molecules organization in this mesophase.

Usually, the column cross section in a honeycomb structure formed by T-shaped molecules is composed of six molecules with a regular hexagonal shape, or stretched 8-molecule hexagonal shape with two long sides and four short sides, but in this columnar phase each hexagon is composed of 10 molecules. The same structure has been previously found for compounds with similar molecular structure [151]. The number of molecules that form the polygon is determined by both lateral chain volume and the interior space of the hexagon. With the increase of the lateral chain volume the molecules tend to form larger hexagons composed by more molecules. In this mesophase all the incompatible parts of the molecules segregate into their own subspaces, leading to the formation of this unique and complex four compartment structure.

3.3.2 New Low-T Phase

The molecular structure of the compound T-C$_3$(C$_{11}$F$_8$) is shown in Figure 3.4a. Small angle X-ray scattering experiment was carried out on a powder sample which was prepared in a glass capillary with diameter of 1mm. However, the phase transition in a powder sample is very slow and very sensitive to temperature. As a result, the diffraction patterns are always that of a mixture and no pure phase could be obtained. It might be that the mobility of the molecules in the powder sample is confined by their ambient environment, and the molecules cannot move freely to form their equlibrium arrangement. To overcome this problem grazing incidence small angle X-ray scattering experiments were conducted on oriented thin film sample.
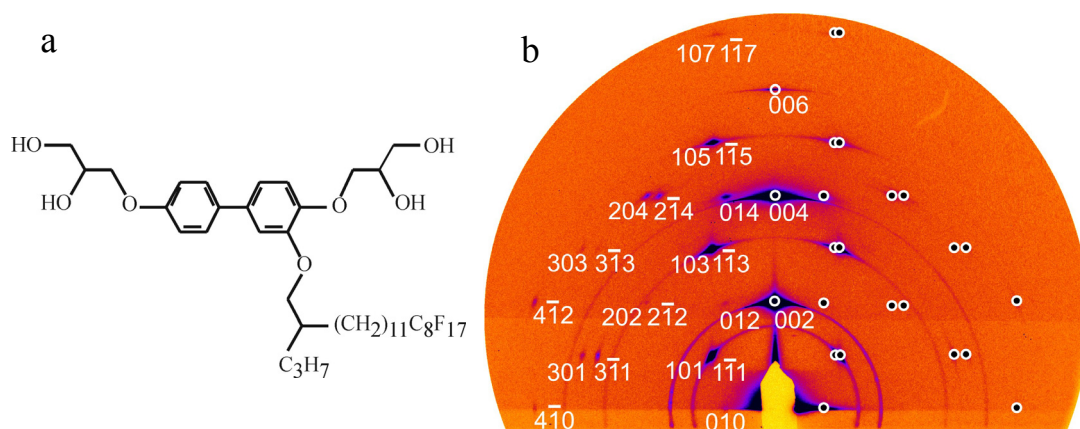
Figure 3.4. a) Molecular structure of compound T-C$_3$(C$_{11}$F$_8$). b) Grazing incidence small angle X-ray scattering pattern recorded at 70 ºC. The white circles show the simulated diffraction positions of the observed reflections on the 2D pattern.

The GISAXS pattern of the new low-T phase of this compound is shown in Figure 3.4b. According to the position of each reflection in reciprocal space and the q ratios between them, this diffraction pattern can be indexed based on a 3D monoclinic lattice. The simulated peak positions are overlaid on top of the GISAXS pattern (Figure 3.4b), showing a nearly perfect fit to the experimental data. The unit cell parameters are a = 73.1 Å, b = 93.4 Å, c= 80.1 Å, and γ = 115.4º. According to the reflection conditions, hkl: $h+l$ = 2n, $hk0$: h = 2n, $0kl$: l = 2n, $h0l$: $h+l$ = 2n, $00l$: l = 2n, $h00$: h = 2n, the space group with highest symmetry that meets the

experimental observation is $C2/m$. Because of the high mobility of the liquid crystalline molecules a structure with higher symmetry is always preferred, we suggest the most likely space group for this monoclinic phase is $C2/m$. The index of each reflection is shown in the diffraction pattern, and the observed along with the calculated d-spacings are listed in Table 3.3. Detailed information about the simulation of diffraction peaks can be found in appendix A2.

An electron density map of the monoclinic phase was reconstructed using the diffraction intensities measured from grazing incidence small angle X-ray scattering pattern. To obtain the diffraction intensities the FibreFix (CCP13) and the PeakSolve[TM] software were used. The 1D diffraction spectrum of each reflection was first obtained by the FibreFix (CCP13) from the GISAXS pattern, and afterwards these 1D spectra were used to get diffraction intensities using the PeakSolve[TM] software. Due the fibre-like feature of the GIXAXS thin film sample, intensities of the off meridian reflections were corrected by multiplying by its q_{xy} value prior to the reconstruction of electron density map, while the as measured intensities were used for the reflections on the meridian. The final diffraction intensities are listed in Table 3.3.

Table 3.3. Experimental and calculated d-spacings, relative integrated intensities, and phases used in the reconstruction of electron density map for the monoclinic phase of sample T-C_3($C_{11}F_8$) at T=75 ºC. All intensity values are Lorentz and multiplicity corrected.

(hkl)	$d_{obs.}$ (Å)/GISAXS	$d_{calc.}$ (Å)	$I(hkl)$	$\varphi(hkl)$
(010)	84.4	84.4	13.12	0
($1\bar{1}1$)	51.9	51.9	3.38	0
(101)	50.9	50.9	13.10	π
(002)	40.1	40.1	50.00	π
(012)	36.2	36.2	0.36	0
($2\bar{1}2$)	26.9	27.0	0.06	π
(202)	25.4	25.5	0.30	π
(103)	24.7	24.7	17.03	0
($1\bar{1}3$)	24.8	24.8	3.70	0
($3\bar{1}1$)	22.8	22.9	2.49	π

(301)	21.1	21.2	1.18	0
(004)	20.0	20.0	40.00	0
(014)	19.4	19.4	-	-
$(3\bar{1}3)$	17.8	17.8	-	-
$(4\bar{1}0)$	17.7	17.7	-	-
$(2\bar{1}4)$	17.4	17.5	-	-
(204)	17.0	17.1	-	-
(303)	16.9	17.0	-	-
$(4\bar{1}2)$	16.1	16.1	-	-
(105)	15.5	15.6	-	-
$(1\bar{1}5)$	15.6	15.6	-	-
(006)	13.4	13.4	-	-
(107)	11.3	11.3	-	-
$(1\bar{1}7)$	11.2	11.3	-	-
a = 73.1 Å, b = 93.4 Å, c = 80.1 Å, α = 90.0º, β = 90.0º, γ = 115.4º				

Figure 3.5a and Figure 3.5b show the electron density maps which were reconstructed using the structure factor phase angles in Table 3.3. Figure 3.5a presents the column cross sections formed by the molecules and two iso-electron density surfaces are used here. The elliptical cross sections with green colour represent the relatively high electron density areas, inside which are the highest electron density regions occupied by the fluorinated ends of the lateral chains. The discontinuous green blocks in the middle of the two column layers indicate the medium electron density regions containing the biphenyl cores and diol groups. The blue colour in between the high and medium electron density regions shows the low electron density areas where the aliphatic spacers of the lateral chains are located. According to subsequent calculations, the circumference of each column is composed of ten end to end connected molecules as indicated in the map and the structure model (Figure 3.5c).
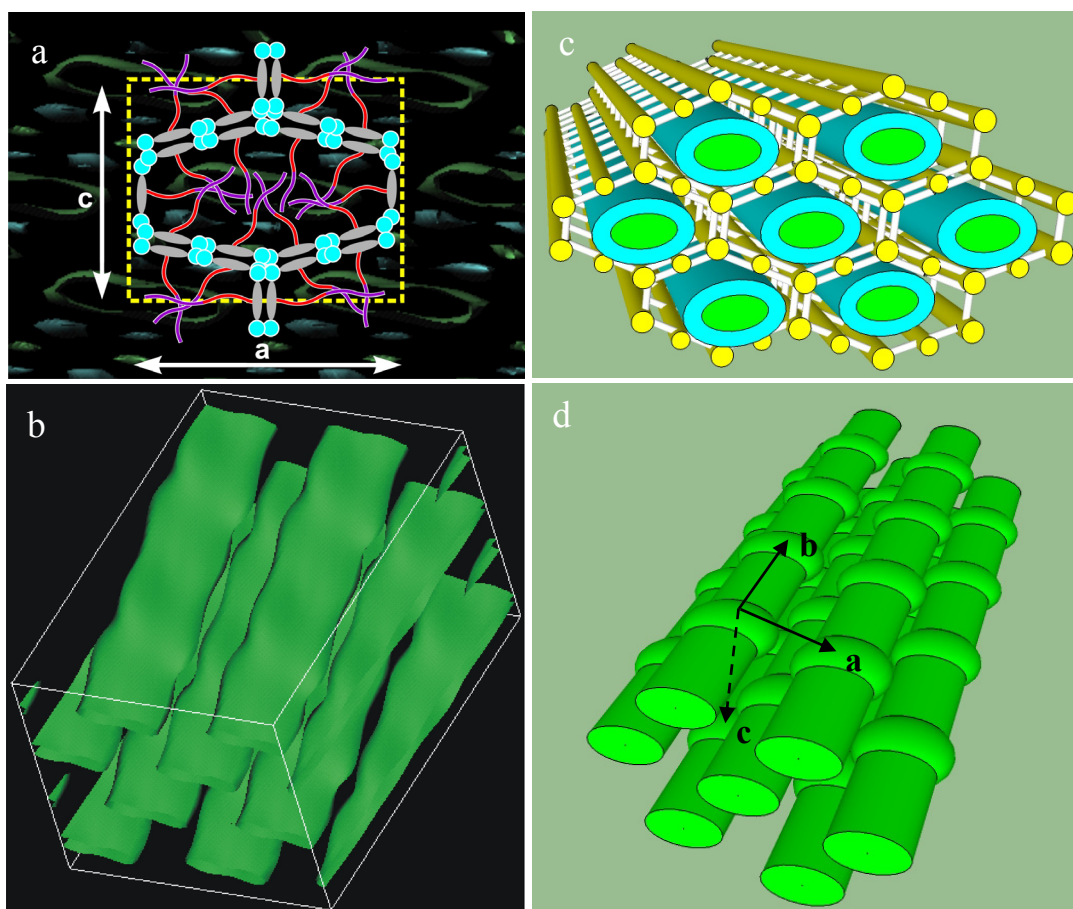
Figure 3.5. Reconstructed electron density map and proposed structure model of the monoclinic new low-T phase of sample T-$C_3(C_{11}F_8)$. a) Reconstructed electron density map view along the column direction. Green and blue isoelectron surfaces enclose relatively high and low electron density regions of the unit cell respectively. The molecular arrangement around the columns is schematically drawn on top. b) The unevenly distributed high electron density regions (fluorinated chain ends) along the column direction. c) and d) the corresponding model of the reconstructed electron density maps, the colour code used is the same as in Figure 3.3.

In order to see the electron density distribution along column direction only the high iso-electron density surface is shown in Figure 3.5b which clearly shows the electron density fluctuation inside each column. This fluctuation is suggested to be caused by the local aggregation of the fluorinated segments of the lateral chains, as at higher temperature the lateral chains expanded more and need more space inside each column. It is envisaged that the expanded lateral chains cannot be fitted within the interior area of the hexagon and they are partly squeezed out of the hexagon plane as indicated in Figure 3.6b which shows the side view of a single hexagon (Figure 3.6a). In this monoclinic structure each column is formed by

the 10-molecule composed hexagons piling up along column direction. With the increase of this piling distance more and more lateral chains will be squeezed out the hexagonal plane, and finally, to maintain the column-like molecule arrangement these lateral chains need to gather at some points in the column where the discontinuous piling of the hexagonal frame appears as depicted in Figure 3.6c. In this figure the red ellipses indicate the local aggregation of the lateral chains, the green and light blue colour show core-shell feature of electron density distribution inside the column. Such arrangement of molecules is an effective way to cope with the volume expansion of lateral chains while keep the columnar structure intact.
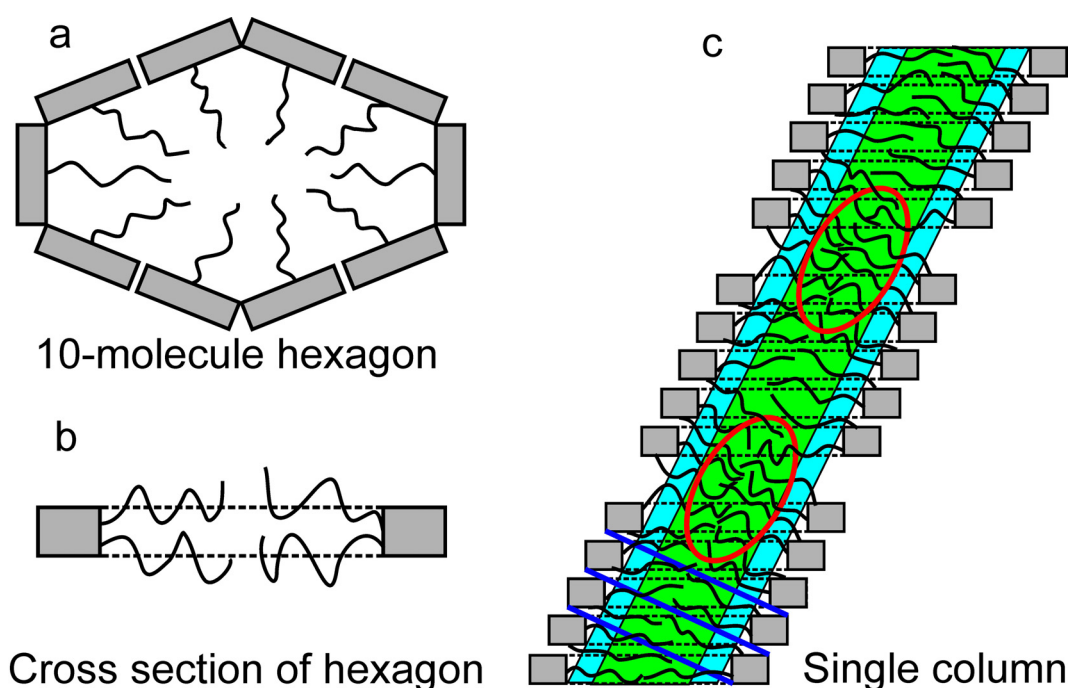
Figure 3.6. a) The 10-molecule composed hexagon in the monoclinic structure. b) The cross section of a single hexagon, which shows the sideway expanded lateral chains. c) Sketch of molecule arrangement during the formation of a single column.

Another feature of this monoclinic structure is that the rigid biphenyl units are no longer perpendicular to the column axes as in the *c2mm* phase. Since the molecular configuration is temperature dependent, at elevated temperature the lateral chain expanded sideways which means the cross section of each lateral chain becomes larger, at the same time the length of the lateral chain becomes shorter. So it is harder or even impossible for these lateral chains to reach the centres of the hexagons, especially for the chains attached to molecules which form

the short sides of the hexagons (see Figure 3.6a). Therefore, to fill the interior space of each column, the piling up style of these hexagons is not exactly one on top another, but they shift gradually along their long axes which is the most difficult direction for the lateral chains to reach the column centre. With this kind of arrangement, the central space of one hexagon can be filled easily by the chains belong to the hexagons above and/or below it as shown in Figure 3.6c. In this case the lateral chains can be considered as lying in the planes indicated by the blue lines which are nearly perpendicular to the column axis.

The number of molecules lie on the circumference of each column was calculated based on the arrangement of the rigid cores and an average stacking distance along column direction. This distance was chosen as 4.5 Å which is the approximate diameter of a biphenyl unit. The molecular number was determined to be 18.5 on average (see appendix A4), which means there are ~10 molecules around each column cross section, as one unit cell contains two columns. The end to end linked 10 molecules form the wall of the column embracing the lateral chains inside as indicated in the electron density map (Figure 3.5a). The gray rods represent the rigid aromatic cores, the blue circles means the polar groups which provide the hydrogen bonding networks to connect these molecules. The shape formed by these 10 molecules is a stretched hexagon with 4 long sides having approximately twice the length of the other two, and each side is composed of one or two rigid biphenyl units depending on the length of it.

In both the low temperature $c2mm$ phase formed by sample T-C_1(O$C_{11}F_8$) and this monoclinic phase a centred lattice is formed. This can be interpreted by the packing style of the columns. The formation of both structures can be considered as a repeat packing of column layers in a A-B-A-B style. The difference between these two structures only comes from the electron density distribution inside each column. In $c2mm$ phase due to the evenly distributed electron density, no correlation was formed along the column direction. However, in this monoclinic phase the electron density fluctuation caused by the aggregations of fluorinated segments leads to the third dimension correlation, consequently a 3D lattice.

3.3.3 New High-T Phase

For sample T-$C_1(OC_{11}F_8)$, a new set of sharp diffraction peaks were recorded by small angle X-ray scattering (SAXS) experiment at the temperature between 69 ºC to 93 ºC as previously shown in Figure 3.2, suggesting the existence of a different mesophase in this temperature range. The powder diffraction pattern of this phase recorded at 90 ºC is shown in Figure 3.7a. The inset shows wide angle X-ray scattering feature, the broad peak confirms the liquid crystal nature of this phase. In order to index this pattern, grazing incidence small angle X-ray scattering experiments were carried out on oriented thin films and the same diffraction peaks were observed (Figure 3.7b). With the knowledge of the q ratios between these peaks observed in the powder diffraction pattern and the positional information of each peak in reciprocal space provided by the GISAXS result, this new phase can be indexed on a triclinic lattice with space group $P\bar{1}$. The unit cell parameters a, b, c are determined to be 81.6 Å, 73.2 Å, 53.6 Å and α, β, γ, are 57.4º, 63.8º, 72.0º respectively. The two sharp peaks with indices (01) and (02) in powder diffraction pattern correspond to the first and second order of the higher temperature lamellar phase. As stated at the beginning of this chapter the phase sequence of this sample was recorded under a cooling run, and at this temperature the lamellar phase remains and co-exists with this new triclinic phase.
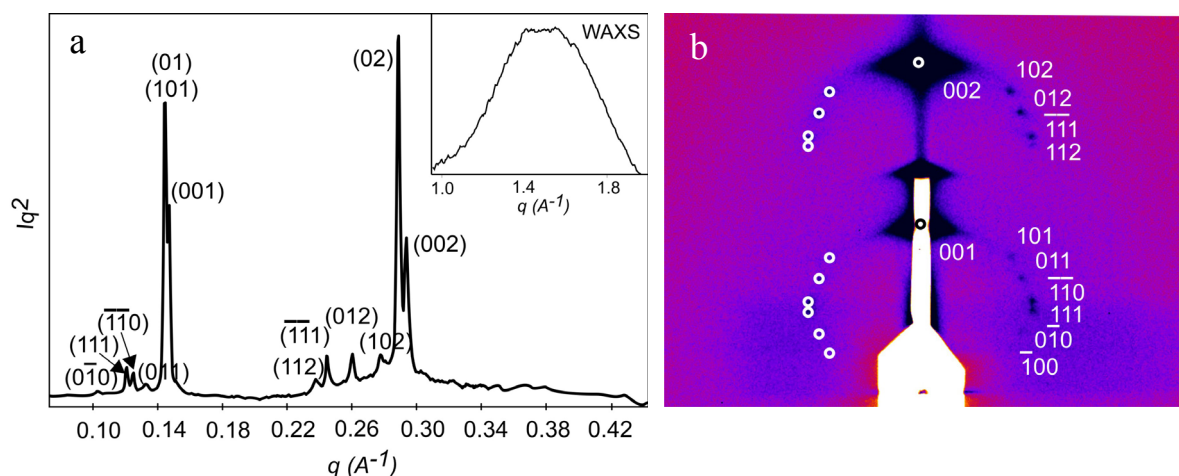

Figure 3.7. X-ray diffraction pattern of the triclinic phase of sample T-$C_1(OC_{11}F_8)$ a) The 1D SAXS spectrum, converted from 2D powder SAXS pattern. The inset is the wide angle X-ray scattering feature. b) GISAXS pattern from an oriented thin film prepared on silicon substrate.

Table 3.4. Experimental and calculated *d*-spacings, relative integrated intensities, and phases used in the reconstruction of electron density map for the triclinic phase of sample T-$C_1(OC_{11}F_8)$. All intensity values are Lorentz and multiplicity corrected.

(*hkl*)	$d_{obs.}$ (Å)	$d_{calc.}$ (Å)	*I(hk)*	$\varphi(hk)$
$(0\bar{1}0)$	61.4	61.4	2.59	0
(111)	51.3	51.1	15.72	π
$(\bar{1}\bar{1}0)$	49.3	49.3	11.79	0
(011)	46.7	46.7	3.30	0
(101)	43.9	43.8	2.47	π
(001)	42.5	42.5	100	π
(112)	26.2	26.1	8.40	0
$(\bar{1}\bar{1}1)$	25.5	25.4	16.94	π
(012)	23.9	23.8	18.55	0
(102)	22.7	22.6	10.45	π
(002)	21.3	21.2	93.83	0
a = 81.6 Å, *b* = 73.2 Å, *c* = 53.6 Å; *α* = 57.4º, *β* = 63.8º, *γ* = 72.0º				

The observed and calculated *d*-spacings are compared in Table 3.4 and a good agreement is achieved between those two sets of data. Diffraction intensities measured by the PeakSolve[TM] software from powder diffraction pattern were used to reconstruct the electron density maps (Figure 3.8) of this triclinic phase with the phase combination listed in Table 3.4. The electron density maps suggest that, the same as its lower temperature columnar *c2mm* phase of this sample, in this 3D structure the molecules are also arranged into columns. The wall of each column is formed by the medium electron density part *e.g.* the biphenyl cores and diol groups; the centre of each column is occupied by the fluorinated segments of the lateral chains which provide the highest electron density, and the area between the column wall and the centre is the low electron density region contributed by the aliphatic spacers. Figure 3.8a shows the cross sections of the core-shell like columns, where the green elliptical iso-electron density surfaces embrace the centre of each column *i.e.* the highest electron density regions. The green blocks in the middle of two column layers mean the medium electron density regions

and the blue colour which separates the high and medium density regions corresponds to the low electron density areas.
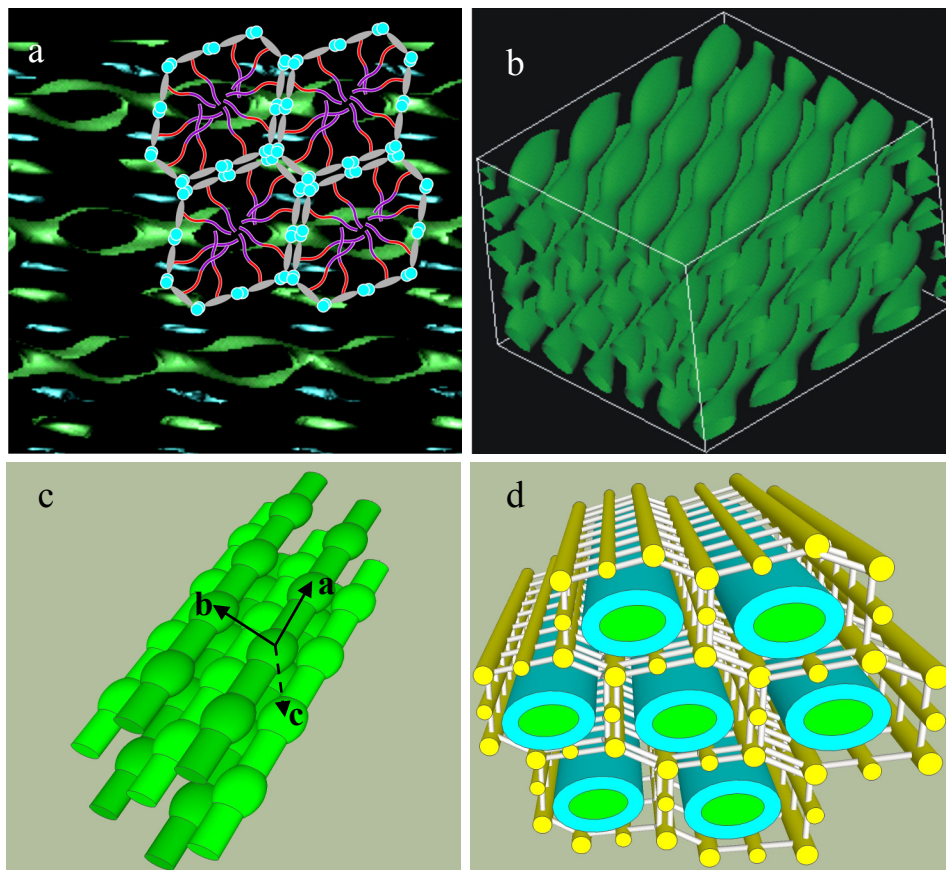

Figure 3.8. Reconstructed electron density map and structure model of the triclinic phase of sample T-$C_1(OC_{11}F_8)$. a) Reconstructed electron density map view along column axis, and two iso-electron density surfaces are used. The green and blue colour represents high and low density region respectively. b) Reconstructed electron density map. Only high iso-electron density surface is used which shows electron density fluctuation along column direction. c) and d) The proposed structure model. c) The central high electron density feature inside columns. d) Sketch of the organization of the molecules in this mesophase. The colour code is the same as in Figure 3.3.

The electron density feature along the column direction is shown in Figure 3.8b, where only the high iso-electron density surface of Figure 3.8a is used. The unevenly distributed electron density caused by the aggregations of fluorinated ends of lateral chains can be clearly seen. The same as stated before, this feature is induced by the sideway expansion of the lateral chains at elevated temperature. As a consequence of coping with the increased lateral chain volume without collapsing the columns, these lateral chains need to form aggregations along

column direction. Due to the shrinkage of the lateral chain length at higher temperature, to fill the centre space of each column, the rigid biphenyl units of the molecules tilted at an angle with respect to the column axes. It was found that in this case the rigid parts of the molecules are arranged along the *b* axis as indicated in Figure 3.8c.

According to calculation, which is based on the arrangement of the rigid units of the molecules and their average stacking distance (4.5 Å) along column direction, the number of molecules lie on the circumference of each column is 10.8 on average (here one unit cell contains only one column), suggesting again that ten molecules form a stretched hexagon with four long sides having approximately twice the length of the other two. Each long side is composed by two rigid biphenyl units, while each short side has the length of one rigid biphenyl unit. The 10-molecule hexagons are depicted in Figure 3.8a, where different parts of molecules are indicated by different colours. The gray rods connected by blue circles represent the rigid aromatic cores that form the wall of the column. The red and purple colour of the lateral chain represents aliphatic spacer of the fluorinated segment respectively.

Figure 3.8c and Figure 3.8d are the schematic models showing the electron density distribution and the arrangement of molecules in this triclinic phase. Comparing with lower temperature columnar phase, the 10 molecules composed hexagons here are distorted due to the expansion of the lateral chains at elevated temperature. Similar to in the new low-T monoclinic phase, the hexagons shift sideways to ensure the lateral chains reach the centre of columns easily and guarantee the space filling. The column model formed by the molecules is similar to the one shown in Figure 3.6.
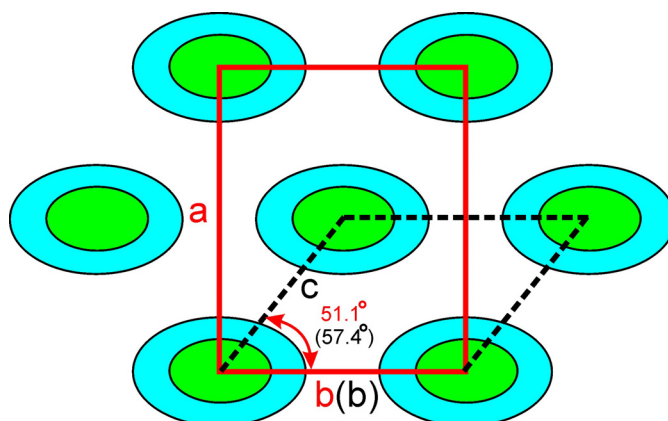

Figure 3.9. Schematic drawing of the relations between the rectangular columnar phase and the triclinic phase of sample T-C_1($OC_{11}F_8$).

More intimate relations can be found between the low temperature rectangular phase and the triclinic phase of this sample, if we compare the unit cells of the two structures. In Figure 3.9 the red line indicates the unit cell of the *c2mm* phase and the black dashed line represents the projection of *b, c* axes of the triclinic phase. In the unit cell of *c2mm* phase the distance between the centre column and the one at the origin is calculated to be 53.2 Å and this distance can be considered to form the unit cell parameter *c* (53.6 Å) of this triclinic phase during phase transition. The length of unit cell parameter *b* in triclinic phase is 73.2 Å which can be corresponded to the unit cell parameter *b* (66.9 Å) in *c2mm* phase. The angle between *b* and *c* in triclinic phase is 57.4º, and its counterpart in *c2mm* phase is 51.1º. The slight difference between the lengths and angles might be caused by the shift of columns along their axes. So from this point of view, the relation between this *c2mm* and triclinic phase can be interpreted as a phase transition from a centred lattice to a primitive one accompanied by column shift in the third dimension.
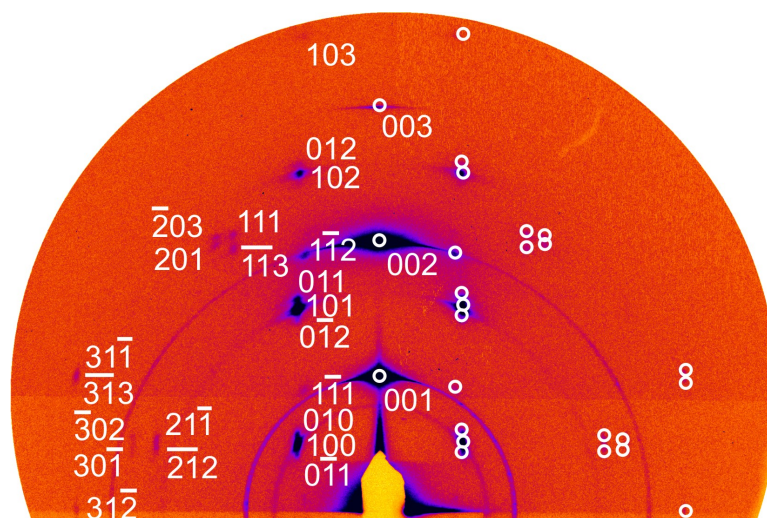
Figure 3.10. Grazing incidence small angle X-ray scattering pattern of the triclinic phase of sample T-$C_3(C_{11}F_8)$ recorded at 75 ºC. The white circles indicate the simulated diffraction positions of all the observed reflections in the 2D pattern.

For sample T-$C_3(C_{11}F_8)$, the same triclinic structure was found at temperature between 75 ºC and 84 ºC. Grazing incidence small angle X-ray scattering pattern of this phase recorded at 75 ºC is shown in Figure 3.10. The unit cell parameters were determined as *a*, *b*, *c* equals 74.2 Å, 67.6 Å and 43.9 Å, *α*, *β*, *γ* equals 75.1º, 79.1º and 53.6º, respectively. The observed and

calculated *d*-spacings are listed in Table 3.5. The 2D simulated diffraction pattern is also shown in Figure 3.10 as indicated by the white circles. Detailed information about this simulation can be found in the appendix. The diffraction intensity and phase angle of each reflection in Table 3.5 were used to reconstruct electron density maps of this mesophase.

Table 3.5. Experimental and calculated *d*-spacings, relative integrated intensities, and phases used in the reconstruction of electron density map for the triclinic phase of sample $T\text{-}C_3(C_{11}F_8)$ at T=75 ℃. All intensity values are Lorentz and multiplicity corrected.

(*hkl*)	$d_{obs.}$ (Å)/GISAXS	$d_{calc.}$ (Å)	*I(hkl)*	*φ(hkl)*
$(0\bar{1}1)$	53.5	53.6	0.52	0
(100)	50.6	50.6	13.12	0
(010)	47.5	47.5	0.91	0
(001)	39.9	39.9	50	π
$(1\bar{1}1)$	37.5	37.5	1.14	π
$(0\bar{1}2)$	25.5	25.6	0.31	π
(101)	24.4	24.4	13.69	π
(011)	23.6	23.5	19.1	0
$(\bar{2}\bar{1}2)$	22.8	22.8	2.3	π
$(2\bar{1}\bar{1})$	22.8	22.8	2.3	π
$(\bar{3}02)$	20.7	20.8	0.1	π
$(30\bar{1})$	20.7	20.7	0.1	0
$(1\bar{1}2)$	20.1	20.0	1.82	0
(002)	19.8	19.9	40	0
$(\bar{1}\bar{1}3)$	17.8	17.8	-	-
$(31\bar{2})$	17.5	17.5	-	-
(111)	17.1	17.1	-	-
(201)	17.1	17.1	-	-
$(\bar{2}03)$	16.8	16.7	-	-
$(31\bar{1})$	16.1	16.0	-	-
$\bar{3}1\bar{3}$	16.0	16.0	-	-

(102)	15.3	15.4	-	-
(012)	15.1	15.0	-	-
(003)	13.2	13.2	-	-
(103)	11.1	11.1	-	-
$a = 74.2$ Å, $b = 67.6$ Å, $c = 43.9$ Å, $\alpha = 75.1°$, $\beta = 79.1°$, $\gamma = 53.6°$				

The reconstructed electron density map (Figure 3.11a) clearly shows the columnar feature of this structure. Similar to the previous triclinic phase found in compound T-C_1(O$C_{11}F_8$), the T-shaped molecules in this triclinic structure form separate columns and each column is walled off from its neighbours by rigid biphenyl units. The interior areas of the columns are filled by the lateral chain of the molecules, contributing to the highest electron density regions which correspond to the areas embraced by the green elliptical iso-electron density surfaces. The blue colour in this map represents low electron density regions containing the aliphatic spacers of molecules. Based on theoretical calculation, the cross section of each column has a shape of stretched hexagon with 10 molecules lying on the circumference as illustrate in the electron density map. Figure 3.11b shows the electron density distribution feature along column direction caused by the unevenly distributed fluorinated segments of the lateral chains. The models of the molecules arrangement and electron density fluctuation correspond to the reconstructed electron density maps are shown in Figure 3.11c and Figure 3.11d respectively.

The phase transition from low temperature monoclinic phase to high temperature triclinic phase of this sample is quite similar to the transition from *c2mm* phase to triclinic phase found in sample T-C_1(O$C_{11}F_8$). The further distorted hexagons provide larger space to accommodate the volume increased lateral chains without collapsing the columns. Due to the space filling requirement, the rigid units of the molecules are arranged along *a* axis (Figure 3.11d) which tilts at an angle with respect to the column axes. The aggregations of the fluorinated ends cause the electron density fluctuation inside each column and the relative shift of the columns along their axes destroyed the A-B-A-B packing style of column layers in monoclinic phase, leading to the transition to triclinic phase. During this phase transition the distance between column layers is almost kept the same: 39.0 Å in the triclinic phase and 40.1 Å in the monoclinic phase, and these values correspond to the layer distance of the lamellar phase at higher temperature, the structure of which will be discussed later.
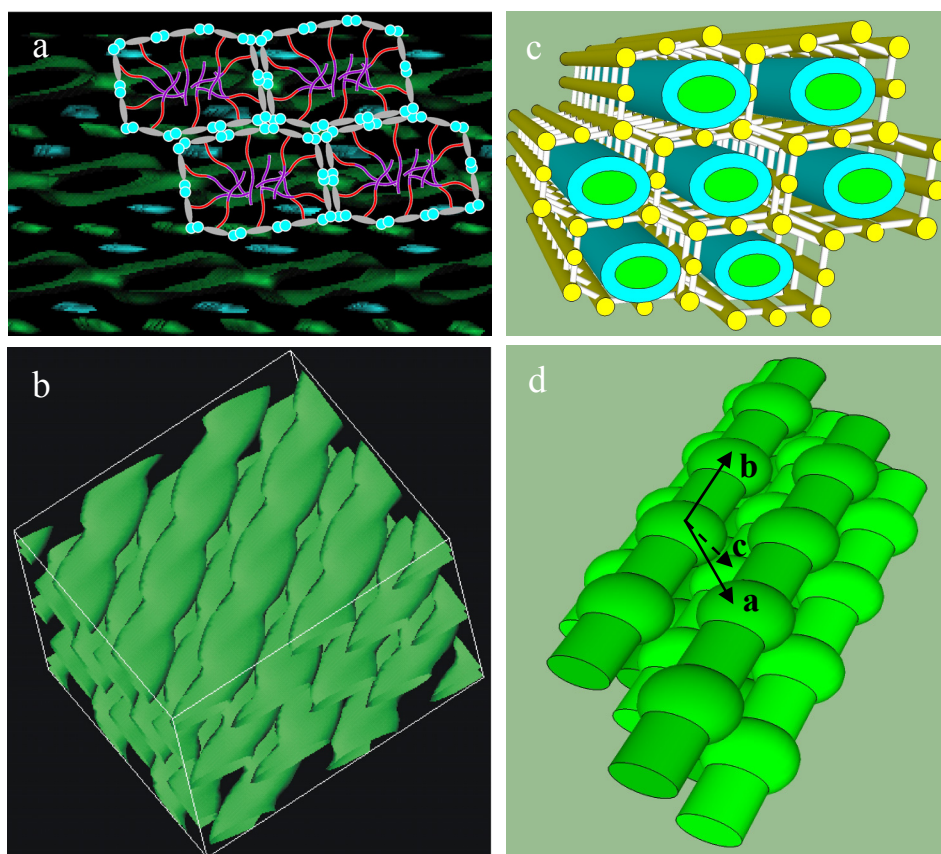
Figure 3.11. Reconstructed electron density map and proposed structure model of the triclinic phase of sample T-C_3($C_{11}F_8$). a) The column cross sections and the molecule arrangement on the circumference of each cross section. b) The unevenly distribute electron density along column direction. c) and d) the corresponding model of the reconstructed electron density maps. The colour code is the same as Figure 3.3.

The same triclinic structure was also found in compound T-C_4F_{10}, the chemical structure of which is shown in Figure 3.12a. The 1D diffraction spectra of SAXS shown in Figure 3.12b were recorded at a continuous heating run from 60 ℃ to 115 ℃ with a heating rate 2 ℃/min and a interval of 30 seconds between each frame. Three different mesophases are indicated. The triclinic phase exists at relatively higher temperature below the lamellar phase.

The powder SAXS pattern of this triclinic phase along with the index of each reflection is shown in Figure 3.12c. Grazing Incidence small angle X-ray scattering experiments were also carried out on oriented thin film sample to help index and confirm this structure. The same diffraction peaks plus some higher order ones were observed in the GISAXS pattern (Figure

3.12d). According to experimental results, the unit cell parameters *a*, *b*, *c* are determined to be 76.9 Å, 76.4 Å, 53.1 Å and *α*, *β*, *γ*, are 121.7º, 118.1º, 71.5º respectively.
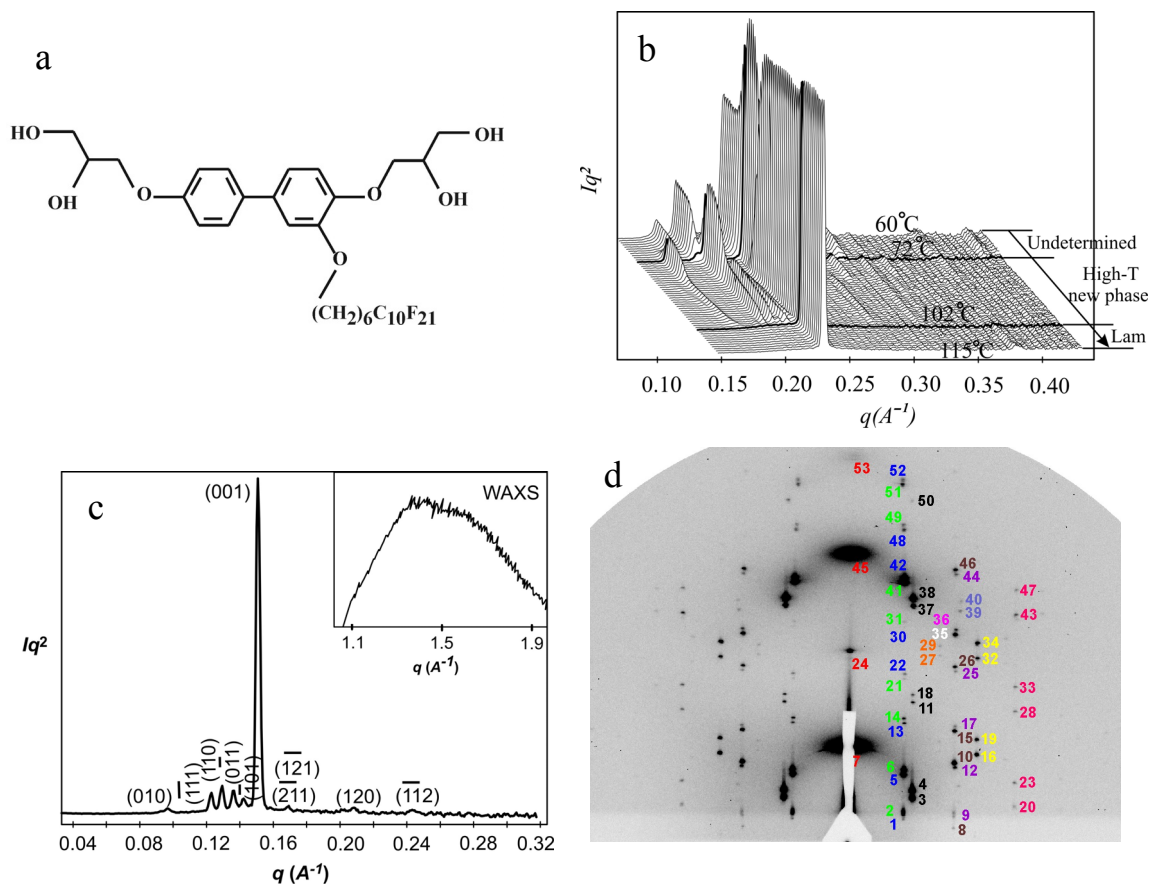

Figure 3.12. a) Chemical structure of compound T-C$_4$F$_{10}$. b) The diffraction spectra recorded under a heating run from 60 ºC to 115 ºC with a heating rate 2 ºC/min. The diffractograms were recorded every 30 seconds. Three mesophases are indicated in this picture. c) The 1D SAXS spectrum of triclinic phase, converted from 2D powder SAXS pattern taken at 90 ºC. The inset is the wide angle X-ray scattering feature. d) GISAXS pattern from an oriented thin film prepared on silicon substrate.

With improved orientation of thin film sample on substrate surface, numerous reflections can be observed in this GISAXS pattern. To see the reflections clearly, only a simple number is used to mark each reflection in the diffraction pattern and the index corresponds to each number is listed separately in Table 3.6, where the observed and calculated *d*-spacings are also given. The simulation pattern and detailed information is given in appendix A2. The good agreement between the experimental and simulated pattern confirms the triclinic structure.

Table 3.6. Experimental and calculated d-spacings, relative integrated intensities, and phases used in the reconstruction of electron density map for the triclinic phase of sample T-C_4F_{10} at T=90 ºC. All intensity values are Lorentz and multiplicity corrected.

No.	(hkl)	$d_{obs.}$ (Å)	$d_{calc.}$ (Å)	$I(hkl)$	$\varphi(hkl)$
1	(100)	67.5	67.5	0.14	0
2	(010)	64.7	64.7	3.14	0
3	$(\bar{1}\bar{1}1)$	50.9	50.8	9.11	π
4	(110)	48.9	49.0	12.06	0
5	$(0\bar{1}1)$	45.8	45.7	8.84	π
6	$(\bar{1}01)$	43.8	43.7	4.21	π
7	(001)	41.8	41.8	100	π
8	$(\bar{1}\bar{2}1)$	37.0	37.0	1.17	π
9	$(\bar{2}\bar{1}1)$	37.0	36.9	1.17	0
10	(120)	30.2	30.3	6.36	0
11	$(\bar{1}\bar{1}2)$	25.9	25.8	-	-
12	(210)	31.2	31.1	-	-
13	(101)	30.6	30.7	-	-
14	(011)	29.6	29.6	-	-
15	$(\bar{1}22)$	25.5	25.7	-	-
16	$(\bar{2}\bar{2}2)$	25.5	25.4	-	-
17	$(\bar{2}\bar{1}2)$	25.0	25.1	-	-
18	(111)	25.0	25.1	-	-
19	(220)	24.5	24.5	-	-
20	$(23\bar{1})$	23.3	23.5	-	-
21	$(0\bar{1}2)$	23.3	23.2	-	-
22	$(\bar{1}02)$	22.4	22.5	-	-
23	$(\bar{2}\bar{3}2)$	22.4	22.4	-	-
24	(002)	21.0	20.9	-	-
25	(211)	20.2	20.1	-	-
26	(121)	19.5	19.6	-	-

27	$(1\bar{1}2)$	19.5	19.4	-	-
28	(230)	18.9	19.0	-	-
29	$(\bar{1}12)$	18.4	18.5	-	-
30	(102)	18.0	18.1	-	-
31	(012)	17.6	17.7	-	-
32	$(\bar{2}\bar{2}3)$	17.6	17.6	-	-
33	$(\bar{2}\bar{3}3)$	17.2	17.3	-	-
34	(221)	17.2	17.1	-	-
35	$(\bar{1}\bar{2}3)$	16.9	17.0	-	-
36	$(\bar{2}\bar{1}3)$	16.7	16.7	-	-
37	$(\bar{1}\bar{1}3)$	16.4	16.3	-	-
38	(112)	16.0	16.0	-	-
39	$(0\bar{2}3)$	15.5	15.6	-	-
40	(202)	15.5	15.4	-	-
41	$(0\bar{1}3)$	15.0	15.1	-	-
42	$(\bar{1}03)$	14.7	14.8	-	-
43	(231)	14.2	14.3	-	-
44	(212)	14.2	14.1	-	-
45	(003)	13.9	13.9	-	-
46	(122)	13.9	13.8	-	-
47	$(\bar{2}\bar{3}4)$	13.0	13.1	-	-
48	(103)	12.6	12.7	-	-
49	(013)	12.6	12.5	-	-
50	(113)	11.7	11.6	-	-
51	$(0\bar{1}4)$	11.1	11.1	-	-
52	$(\bar{1}04)$	11.1	11.0	-	-
53	(004)	10.4	10.4	-	-
$a = 76.9$ Å, $b = 76.4$ Å, $c = 53.1$ Å; $\alpha = 121.7º$, $\beta = 118.1º$, $\gamma = 71.5º$					

The electron density map of this triclinic phase is reconstructed using the diffraction intensities measured from powder diffraction pattern and phase angles listed in Table 3.6.

Figure 3.13a shows the cross sections of the columns formed by these T-shaped molecules. The high electron density regions contributed by the fluorinated ends of lateral chains are embraced inside each column, the rigid aromatic parts arranged on the circumferences of the columns, and the low electron density aliphatic spacers lie in between those two. However, due to the relatively short spacer of the lateral chain in this sample, the biphenyl cores and aliphatic segments cannot separate properly to form their own subspaces. So the well defined high-medium-low electron density distribution observed in previous triclinic phases is not shown here, only the high and low density regions can be seen in Figure 3.13a. The same feature was also observed for the high temperature lamellar phase of this sample.
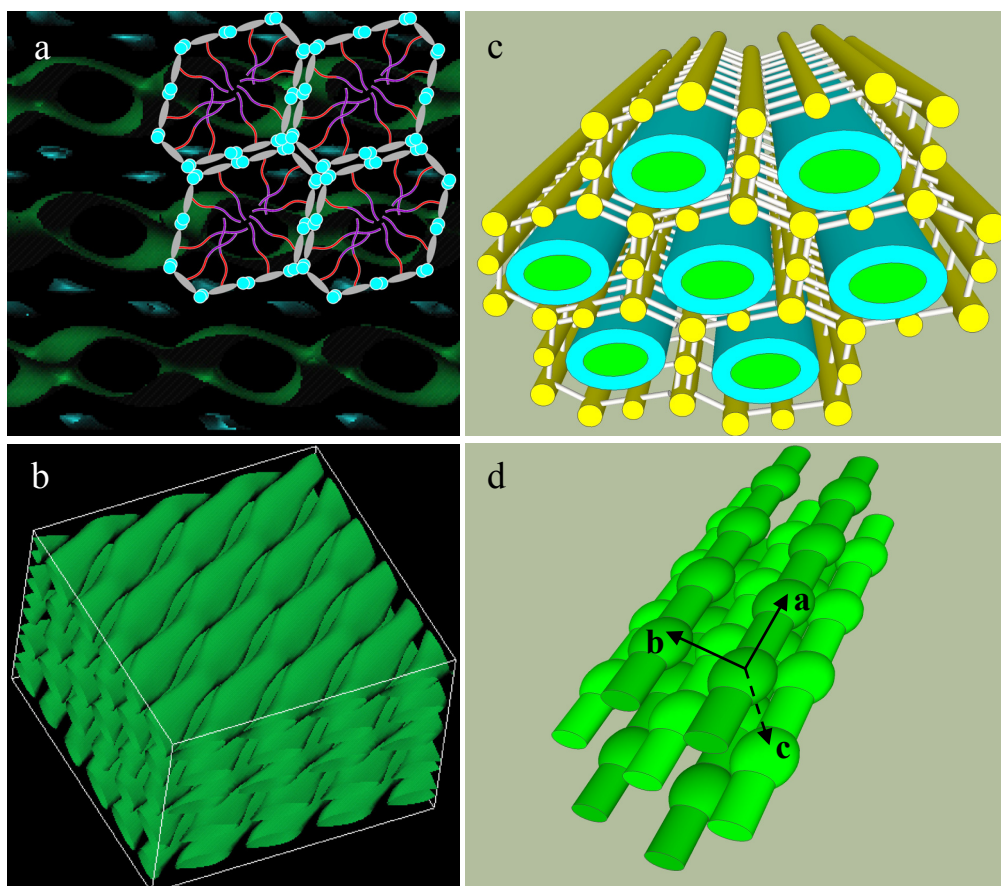

Figure 3.13. Reconstructed electron density map and proposed structure model of the triclinic phase of sample T-C$_4$F$_{10}$. a) The column cross sections and the molecule arrangement on the circumference of each cross section. b) The unevenly distribute electron density along column direction. c) and d) the corresponding model of the reconstructed electron density maps. The colour code used in these models is the same as in Figure 3.3.

The number of molecules on the circumference of each column cross section is 10 which are calculated on the basis of arrangement of biphenyl units and a height of 4.5 Å along column direction. The arrangement of the molecules is shown in the electron density map (Figure 3.13a) and the colour code used is the same as before. Figure 3.13b shows the unevenly distributed electron density along column direction. The corresponding models of the reconstructed electron density maps are shown in Figure 3.13c and Figure 3.13d.

3.3.4 High Temperature Lamellar Phase

X-ray scattering patterns of the highest temperature phase of these three compounds were recorded and show very similar features. Figure 3.14a shows the SAXS diffratogram of T-$C_1(OC_{11}F_8)$. It is characterised by the first and the second order reflections of a layer structure with a layer thickness of 43.3 Å. The same structure was also confirmed by GISAXS experiments (Figure 3.14b). Figure 3.14c shows that the same lamellar structure is observed for sample T-C_4F_{10}, as confirmed by X-ray diffraction experiments on both powder (the 1D spectrum) and oriented thin film (inset GISAXS pattern) samples. Here the layer thickness was found to be 41.1 Å. The GISAXS pattern of T-$C_3(C_{11}F_8)$, recorded at 90 ºC, is show in Figure 3.14d. Two sharp reflections observed at meridian can be indexed as the first and the second diffraction orders of a lamellar structure with layer thickness of 39.3 Å. The indices, experimental and calculated d-spacings of the observed reflections of these lamellar phases are listed in Table 3.7, Table 3.8 and Table 3.9 respectively.

It should be noted here that in the GISAXS pattern of sample T-$C_3(C_{11}F_8)$ (Figure 3.14d), two other reflections were also observed. These two additional reflections are believed to come from the in-plane correlation and provide the information of ordered molecule arrangement within each layer. Thus this lamellar phase can be specified as lamellar smectic phase (Lam$_{Sm}$). In lamellar smectic phase molecules also possess positional and orientational order which is similar to the traditional smectic liquid crystal phases. But one of the most significant differences between them is that in smectic liquid crystal phases the rigid cores of the molecules are perpendicular to the layer planes. On the contrary, in lamellar smectic phases they are parallel to the layer planes. The diffraction peaks at meridian reflect the distance between layers and this distance is mainly determined by the length of lateral chain. While the other two reflections observed in this diffraction pattern come from the positional order of the

molecules within each sublayer, and the horizontal positions of them depend on the length of the biphenyl core and the diol groups at each end of it. This Lam_{Sm} phase is also confirmed by the polarized optical microscopy. A typical paramorphotic mosaic-like texture [46] of this phase is shown in Figure 3.15a. In the micrographs taken with a λ-plate (Figure 3.15b), the yellow and blue colours define the orientation of the high-index axis as radial rather than tangential within fans or "spherulites". The schematic drawing of this lamellar smectic phase is shown in Figure 3.15c. Since the layers are known to be tangential, and the high-index axis is parallel to the biphenyl long axis, it follows that in this Lam_{Sm} phase the biphenyl cores are along the layer growing direction and perpendicular to the layer normal (Figure 3.15d).
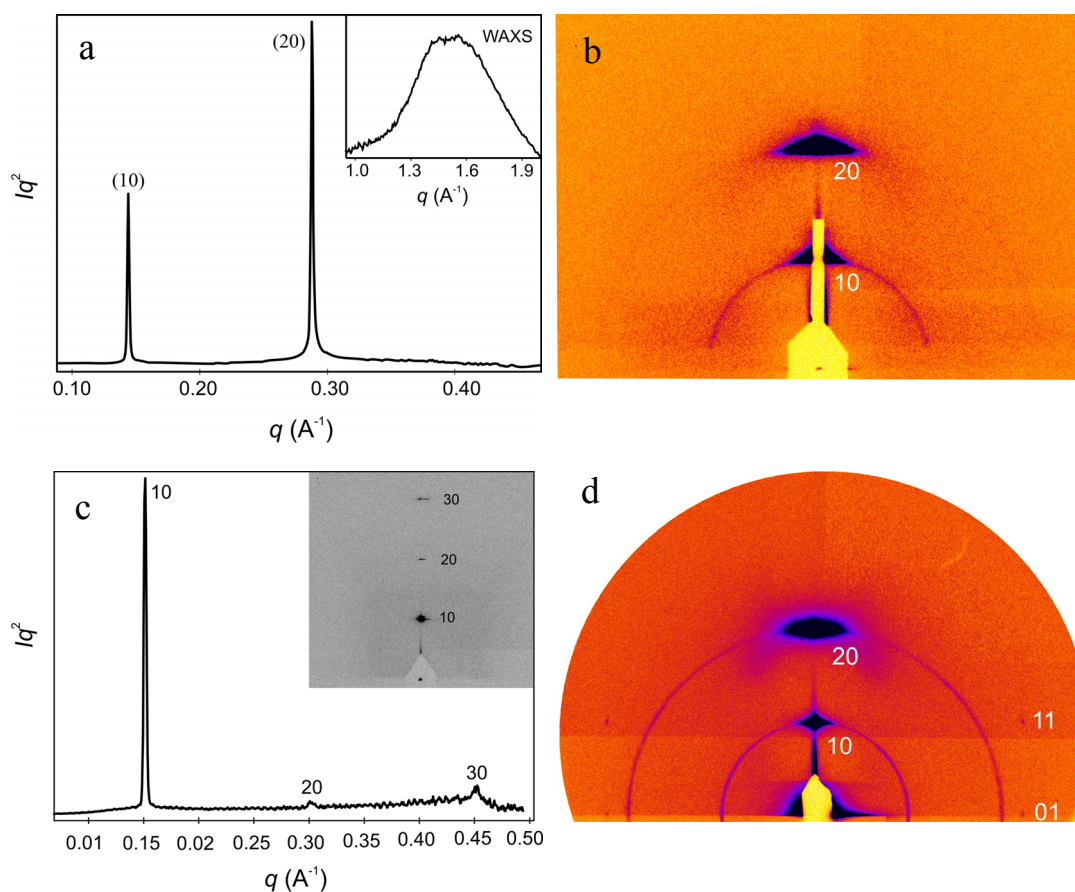

Figure 3.14. Small angle X-ray scattering patterns and grazing incidence small angle X-ray scattering patterns of high temperature lamellar phases of the three samples. a), b) SAXS and GISAXS pattern of sample $T\text{-}C_1(OC_{11}F_8)$ recorded at 115 ℃. The inset shows the wide angle X-ray scattering feature. c) SAXS spectrum of sample $T\text{-}C_4F_{10}$. The inset is the GISAXS pattern of this sample recorded at 100 ℃. d) GISAXS pattern of sample $T\text{-}C_3(C_{11}F_8)$ recorded at 90 ℃.

If we consider this layer structure as a lamellar smectic phase which possess a long range periodicity correlation in adjacent layers, then this lamellar phase can be alternatively interpreted as a two dimensional structure with plane group *p2mm* [152]. In this case the other two reflections can be assigned indices (01) and (11) respectively as shown in Figure 3.14d.
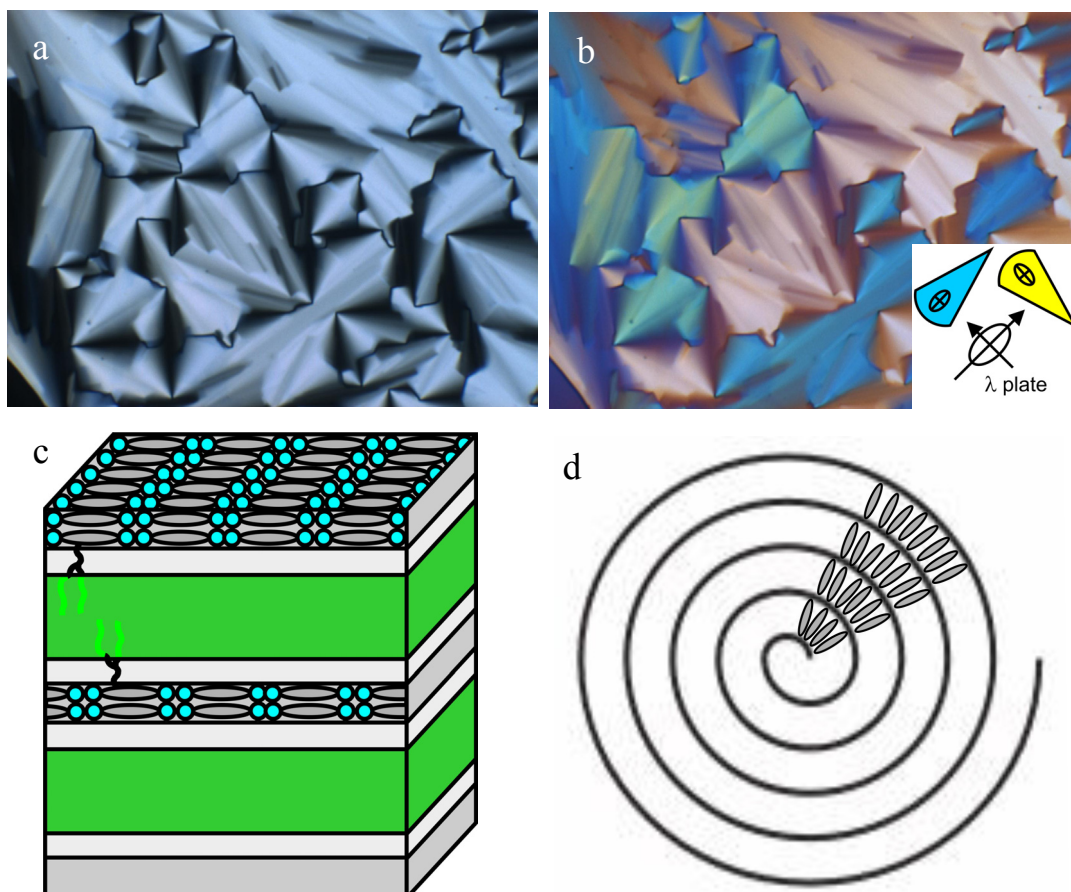

Figure 3.15. a) Texture of the lamellar smectic phase of sample $T-C_3(C_{11}F_8)$ under crossed polarizers recorded at 140 ºC. b) The same phase recorded at the same temperature with λ-plate retarder. The indicatrix orientation in the λ-plate and in the two types of fans is shown in the inset. c) The schematic drawing of lamellar smectic phase. d) The orientation of molecules in the smectic layer.

Table 3.7. Experimental and calculated *d*-spacings, relative integrated intensities, and phases used in the reconstruction of electron density map for the lamellar phase of sample $T-C_1(OC_{11}F_8)$. All intensity values are Lorentz and multiplicity corrected.

(*hk*)	$d_{obs.}$ −spacing (Å)	$d_{cal.}$ −spacing (Å)	*intensity*	*phase*
(10)	43.3	43.3	43.7	π
(20)	21.7	21.7	100.0	0
a = 43.3 Å				

Table 3.8. Experimental and calculated d-spacings, relative integrated intensities, and phases used in the reconstruction of electron density map for the lamellar phase of sample T-C_4F_{10} at 100 ºC. All intensity values are Lorentz and multiplicity corrected.

(hk)	$d_{obs.}$ –spacing (Å)	$d_{cal.}$ –spacing (Å)	intensity	phase
(10)	41.1	41.1	100	0
(20)	20.5	20.5	6.8	π
(30)	13.7	13.7	8.8	0
$a = 41.1$ Å				

Table 3.9. Experimental and calculated d-spacings, relative integrated intensities, and phases used in the reconstruction of electron density map for the lamellar phase of sample T-$C_3(C_{11}F_8)$ at 90 ºC. All intensity values are Lorentz and multiplicity corrected.

(hk)	$d_{obs.}$ –spacing (Å)	$d_{cal.}$ –spacing (Å)	intensity	phase
(10)	39.3	39.3	37.37	π
(20)	19.7	19.7	100.0	0
$a = 39.3$ Å				

The electron density maps of these lamellar phases were reconstructed using the intensities in the Table 3.7, Table 3.8 and Table 3.9 correspondingly. Since the reconstructed electron density maps of sample T-$C_1(OC_{11}F_8)$ and sample T-$C_3(C_{11}F_8)$ are extremely similar, here only one of them, sample T-$C_3(C_{11}F_8)$, is chosen as an example to describe the lamellar structure. Both 2D and 3D reconstructed electron density maps of the layer structure of this sample are shown in Figure 3.16a and b. In these reconstructions the high electron density regions (purple/blue) are attributed to the fluorinated ends, the low electron density regions (red/yellow) contain the aliphatic segments of the lateral chains, and the green/light blue stripes represent the biphenyl core layers which are the medium electron density regions. So in this lamellar phase the molecules form a triply segregated layer structure and each sublayer corresponds to a certain part of the molecules as indicated in the electron density map. The gray rods and light blue circles represent the biphenyl units and polar groups of the molecules respectively, while the two segments of lateral chain are distinguished by different colours.
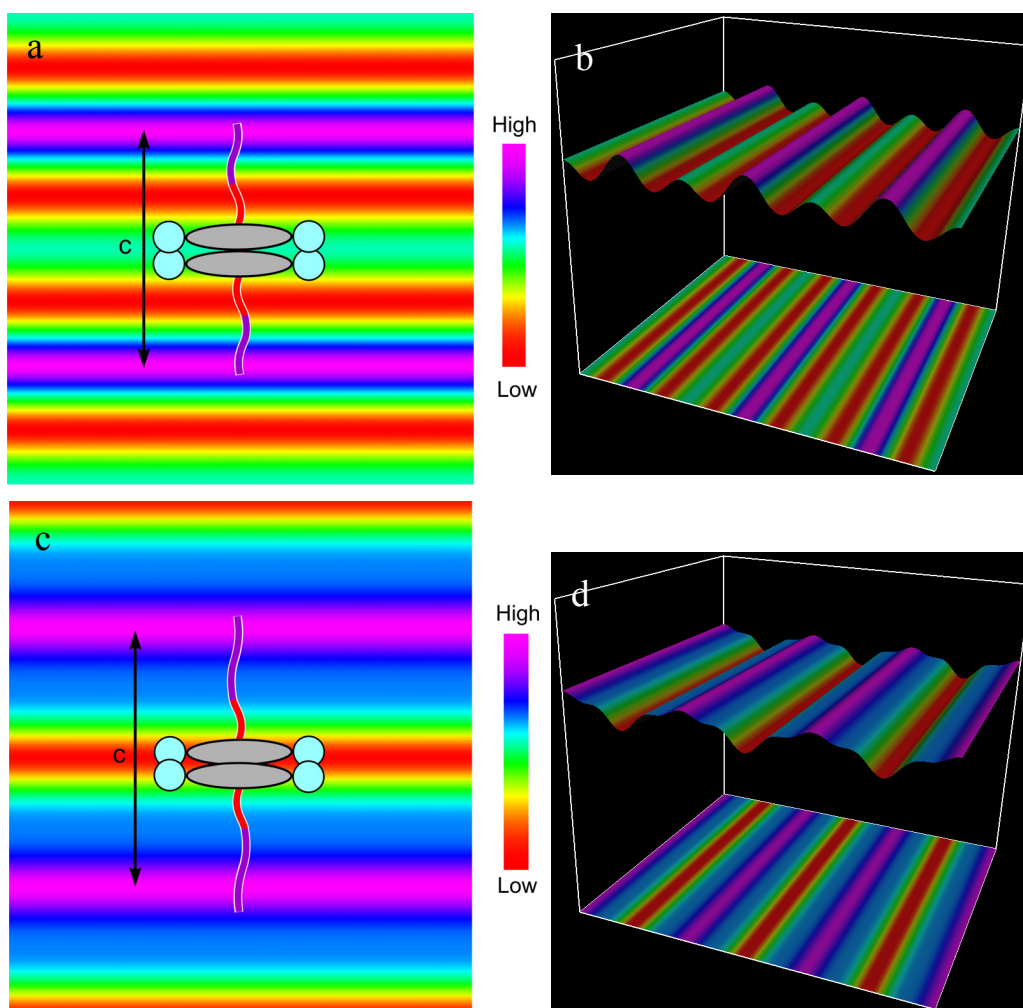
Figure 3.16. Reconstructed electron density maps of the lamellar phases. a) 2D reconstructed electron density map with indication of molecule arrangement in this lamellar phase of sample T-C$_3$(C$_{11}$F$_8$). b) The corresponding 3D reconstructed electron density map of this lamellar phase. c) 2D reconstructed electron density map with indication of molecule arrangement in this lamellar phase of sample T-C$_4$F$_{10}$, and the corresponding 3D reconstructed electron density map.

Figure 3.16c and d show the 2D and 3D reconstructed electron density maps of sample T-C$_4$F$_{10}$. The colour code is the same as described above. However, comparing with the lamellar phase of sample T-C$_3$(C$_{11}$F$_8$), in this lamellar phase only two sublayers can be clearly recognized corresponding to the high and low electron density regions. This is because the length of the aliphatic spacer of the lateral chain in this compound is not long enough to separate itself from the biphenyl core. On the other hand, the electron density difference between the aliphatic spacer and biphenyl core is not so significant; therefore they mix

together and form the low electron density sublayers, while the fluorinated ends of the lateral chains form the high electron density sublayers.
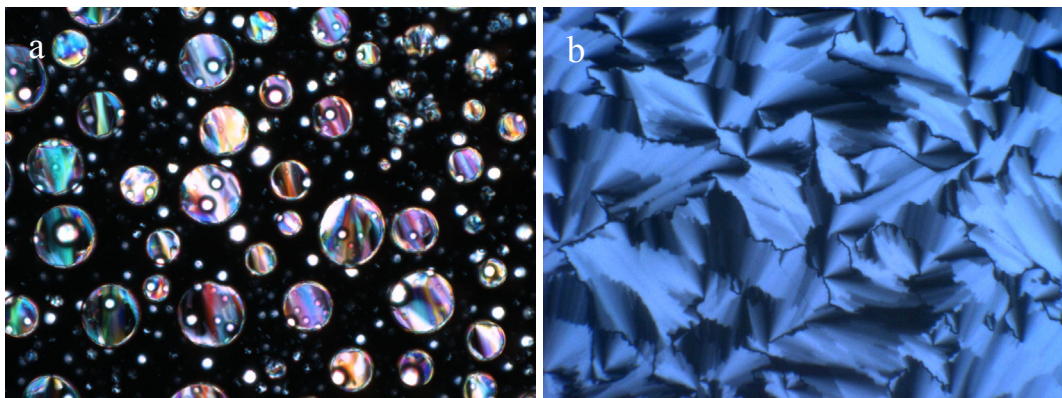

Figure 3.17. Texture of the lamellar phase of sample T-C$_4$F$_{10}$ under crossed polarizers. a) Texture of lamellar isotropic phase recorded at 175 ºC. b) Texture of lamellar smectic phase recorded at 130 ºC.

According to polarized optical microscopy, sample T-C$_4$F$_{10}$ shows two different lamellar phases, lamellar smectic phase (Lam$_{Sm}$) and lamellar isotropic phase (Lam$_{Iso}$). The typical Lam$_{Iso}$ optical texture which contains some oily streaks and other defects, along with that of the Lam$_{Sm}$ phase are shown in Figure 3.17. In both lamellar phases the layers are mostly parallel to the glass surface and perpendicular to the incident light. As in the Lam$_{Iso}$ phase the biphenyl backbones of molecules have no preferred in-plane orientation, unlike in the Lam$_{Sm}$ phase. Consequently under POM the texture of Lam$_{Iso}$ phase is mostly black. The bright and coloured areas as seen in Figure 3.17a are caused by the nonperfect alignment of the layers *i.e.* the layers are not exactly parallel to the glass surface. In this case the birefringence originated from whether the polarization of the light is parallel or normal to the layer surfaces. Lamellar isotropic and lamellar smectic phases, plus lamellar nematic phase have been previously reported for compounds with similar structures [46, 48-49, 153-154]. Normally, from low to high temperature Lam$_{Sm}$ phase forms first, in which the aromatic units arrange parallel to the layer plane and within each layer the molecules possess a SmA-like in-plane order. At increased temperature this in-plane order of the aromatic cores disappeared and only orientational order is left in each layer, leading to the formation of the Lam$_N$ phase. Finally, with a further increase of temperature the third lamellar phase which is a lamellar isotropic phase can be formed. In this case the rigid cores of the molecules are completely disordered

within each sublayer. However, due to the electron density modulation in each sublayer is much lower than that perpendicular to the layers[46, 49], these different lamellar phases cannot be distinguished easily by X-ray diffraction techniques, so they are generally called lamellar phase only.

3.4 Conclusion

In summary, mesophases formed by compounds with T-shaped molecular structure were investigated by small angle X-ray scattering and grazing incidence small angle X-ray scattering methods. Novel structures and phase sequences have been obtained. Although the molecular structures of the compounds under study are quite similar to each other, different phase behaviours are observed. The formation of these ordered liquid crystalline structures is driven by the special molecular shape and the segregation of incompatible parts of the molecules. For compound T-$C_1(OC_{11}F_8)$ the phase sequence is a 10-molecule giant hexagonal phase ($Col_{rec}/c2mm$ lattice) $\rightarrow$ triclinic phase ($P\bar{1}$) $\rightarrow$ lamellar phase. Compound T-$C_3(C_{11}F_8)$ has a phase sequence of monoclinic phase ($C2/m$) $\rightarrow$ triclinic phase ($P\bar{1}$) $\rightarrow$ lamellar phase, here the lamellar phase can be specified as lamellar smectic (Lam_{Sm}) phase. The low temperature phase of compound T-C_4F_{10} has not been decided yet, but the other two at higher temperatures are the triclinic and the lamellar phases, respectively. In all of these obtained mesophases, except the high temperature lamellar ones, molecules form cylindrical columns. The centre of each cylinder is occupied by the long lateral chains, while the rigid biphenyl units connected by the polar groups form the wall of each cylinder. Different electron density fluctuation features along column direction were found, depending on the distribution of the fluorinated ends of the lateral chains. If the lateral chains distribute evenly inside each column and there is no electron density fluctuation along column direction, 2D rectangular columnar phase ($Col_{rec}/c2mm$ lattice) is obtained. Otherwise, the local aggregation of the fluorinated ends leads to the formation of the third dimension order, and then 3D structures are formed.

In previously reported columnar phases formed by T-shaped bolaamphiphiles with similar molecular structures, it was found that normally each cylinder is composed of six molecules/sides with a regular hexagonal shape, or 8-molecule hexagonal phase which has

two long sides and four short sides. The latter one can be considered as a normal hexagon stretched along one pair of its opposite corners as indicated by the black arrows in Figure 3.18. However, the cylinders in all the structures reported here are composed of ten molecules with four long sides and two short sides. The 10-molecule giant hexagon can be obtained by elongating a normal hexagon perpendicular to one pair of its opposite sides as indicated by the red arrows in Figure 3.18. With the increase of molecule number on the circumference of a hexagon the interior area of it also increases, thus a larger volume of lateral chains can be fitted inside.
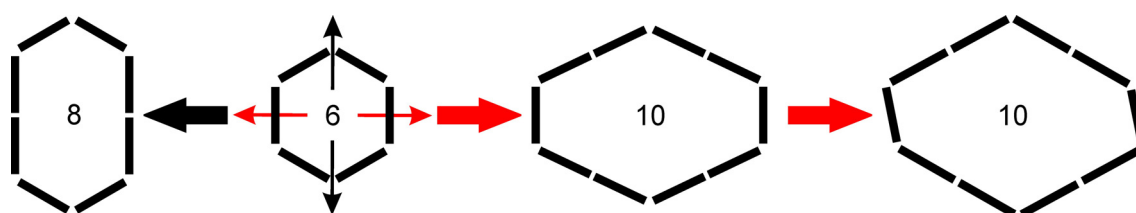

Figure 3.18. Stretching of a regular hexagonal cylinder of Col_{hex} phase along different directions gives two distinct cylinders. The 8-molecule hexagonal cylinder can be obtained by elongating along diagonal direction, while the 10-molecule hexagon can be obtained by elongating along two opposite sides. The 10-molecule hexagon can be further distorted as well for the compounds studied in this chapter.

Due to relative positions of different functional groups in bolaamphiphiles, the frame of the hexagon in columnar phase is shaped by the rigid biphenyl units and the polar groups of the molecules. This makes the perimeter of a hexagon that contains a certain number of molecules almost independent of temperature, as the biphenyl units and short polar groups cannot expand significantly with the changing of temperature. Therefore, the hexagon is quite sensitive to the size of lateral chains which have to fill the interior of the cylinders properly, and even a slight change of lateral chain might affect the hexagon shape or the number of molecules it contained. If the volume of the lateral chains cannot be fitted with the limited space, a larger hexagon is needed, hence the observed conversion from regular hexagonal cylinders to larger stretched 8-molecule hexagon, which is further followed by 10-molecule giant hexagon, is due to the increase of the lateral chain length.
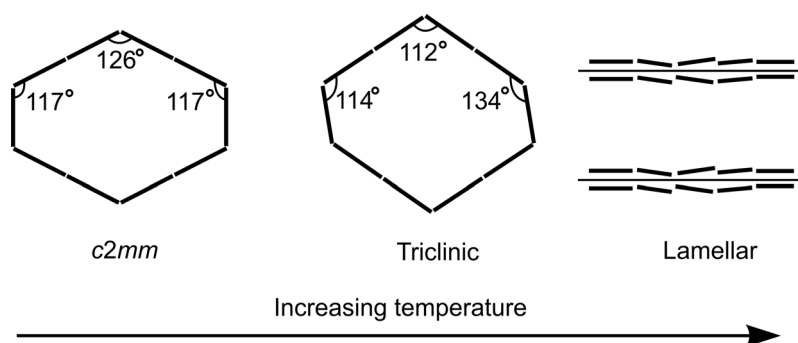
Figure 3.19. The change of cylinder cross section with the increasing of temperature.

Here we found that, for the 10-molecule hexagons, with the transition from low temperature phase to triclinic phase the hexagons can change their shapes to accommodate the increase in volume of lateral chains (Figure 3.18). Taking sample T-C_1($OC_{11}F_8$) as an example, the two hexagons in Figure 3.19 are the cross sections of the cylinders in *c2mm* phase and the triclinic phase, respectively. We can see after the phase transition the 10-molecule hexagon is further distorted. During this process the perimeter of the hexagons is almost the same, but the shape of the hexagons has changed as well as the interior area, by the expansion along two pairs of opposite corners along the short and long axis directions of the stretched hexagon. According the angles and the length of molecule, it was calculated that this area increased about 2.5 % after distortion. However, the volume of the lateral chains can keep expanding with increasing temperature, while the area of a hexagon with a fixed perimeter has an upper limit. Consequently further increase of the lateral chain volume causes the collapse of the cylinders and the transition to the lamellar structure (Figure 3.19).

As a final note, this is the first time that 3D monoclinic and triclinic phases are obtained from self-assembly of T-shaped molecules, and in fact first of its kind in any liquid crystal systems. The results indicate that novel complex structures can be achieved by appropriately designed molecules containing different incompatible groups.

Chapter 4 Nanostructures Formed by Mesogen Functionalized Gold Nanoparticles

4.1 Introduction

In this chapter, nanostructures formed by liquid crystalline molecule functionalized gold nanoparticles will be discussed. These structures were investigated by small angle X-ray scattering and grazing incidence small angle X-ray scattering. The gold nanoparticles are synthesized using the well established Brush-Schiffrin method. A simple schematic drawing of a decorated gold nanoparticle is shown in Figure 4.1.
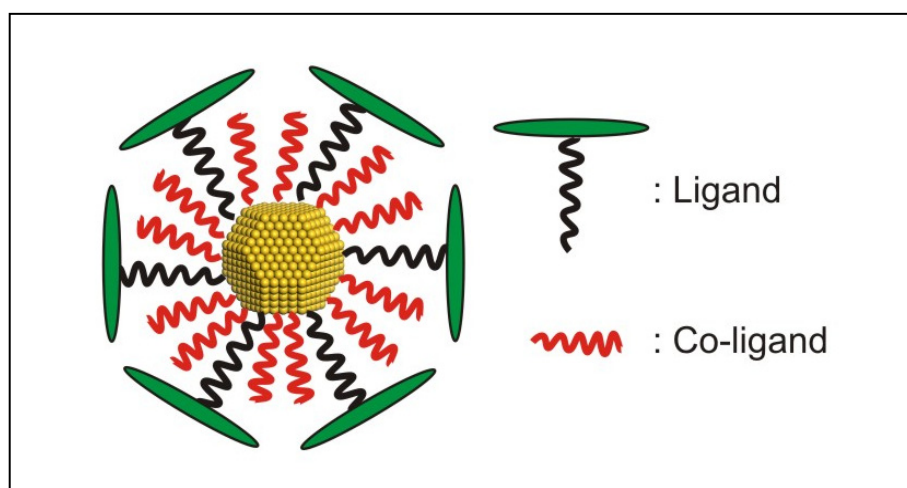

Figure 4.1. Sketch of a gold nanoparticle functionalized by mesogenic ligands and alkyl chain co-ligands.

In this model, the rigid part of the liquid crystalline molecule (ligand) indicated by the green rod is normally referred to as the mesogen which plays a crucial role for the formation of mesophases, while the flexible hydrocarbon terminal ends (which are omitted in the sketch model) increase the mobility of the molecule. In pure liquid crystal systems, the parallel alignment of the anisometric mesogens and the free movement of the flexible chains provide the driving forces for self-assembly, and the optimum balance of these two parts leads to the formation of liquid crystal phases. It has been found that by attaching anisometric mesogenic ligands to gold nanoparticles they display long range order on the mesoscale [155-156]. Gold nanoparticles covered by a mixture of laterally attached four-ring mesogens and unsubstituted

alkylthiol chains can form 3D and 2D structures [157]. These mesophase structures formed were effectively strings of nanoparticles surrounded by a sheath of axially aligned mesogens. In this thesis we continue to explore the effect of mesogen length (three-ring mesogens), type and the proportion of co-ligands on the self-assembly of GNPs. More examples will be shown in this chapter that the self-assembled ordered superstructures can be induced by the attachment of such liquid crystalline molecules.

4.2 Sample List

Table 4.1. The sample code name, molecular structures of ligands and co-ligands of each gold nanoparticle sample studied.
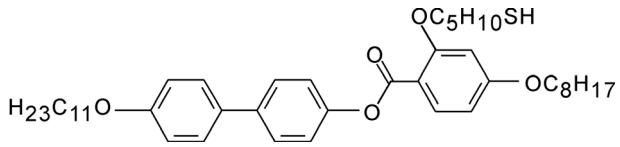
Mesogen property	Sample code name	Mesogenic ligand structure	Co-ligand
Normal liquid crystalline molecules	AuL3		None
	AuL3C6		$C_6H_{13}SH$
	AuL3C12		$C_{12}H_{25}SH$
Chiral molecule	AuCholC6		$C_6H_{13}SH$
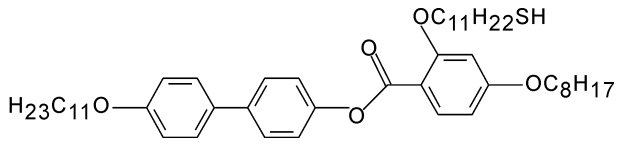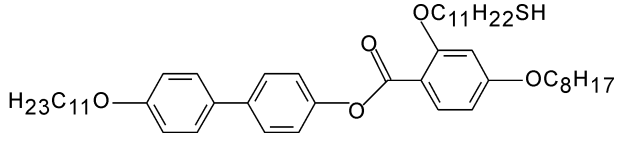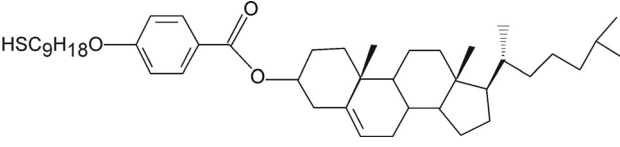
Table 4.1 lists all the gold nanoparticle samples studied and shows the molecular structures of ligands and co-ligands for each sample. As indicated, for sample AuL3, AuL3C6 and AuL3C12 the ligands have the same rigid aromatic core and terminal ends. The ligand

molecules themselves normally show the nematic phase. In sample AuL3 gold nanoparticles are functionalized only by ligands and no co-ligands were used. The 5-carbon chain alkylthiol spacer in this sample is the shortest among all the samples. In sample AuL3C6 a hexylthiol co-ligand chain was introduced and at the same time the length of spacer was increased from 5 to 11-carbon chain. In sample AuL3C12 the ligand molecule used is exactly the same as in sample AuL3C6, but the length of co-ligand is doubled. Finally, a completely different mesogen ligand is used in sample AuCholC6, while the co-ligand is the same as used in sample AuL3C6. In AuCholC6 the ligand used is a chiral molecule which shows a cholesteric nematic phase by itself. While for the first three samples liquid crystalline molecules are attached to gold nanoparticles laterally, for sample AuCholC6 the ligands are end-attached.

4.3 Nanostructures Formed by GNPs Covered with Nematic Forming Mesogens

For sample AuL3, the gold nanoparticles are functionalized only by mesogens which are laterally attached *via* short alkylthiol spacers. From room temperature to 105 ºC, sharp diffraction peaks are observed in small angle X-ray scattering (SAXS) experiments and no birefringence was observed under polarized microscopy. Above 105 ºC, these diffraction peaks disappear and only diffuse peaks are observed, suggesting the formation of isotropic phase which is confirmed by the lack of birefringence. For measurement of diffraction intensities, the 2D powder diffraction pattern (Figure 4.2a) was converted to 1D spectrum (Figure 4.2b) using FiberFix (CCP13), and then Lorentz corrected. As we can see from the powder diffraction pattern, three strong and four weak sharp diffraction peaks are observed for the ordered mesophase.

To help index the diffraction pattern, grazing incidence small angle X-ray scattering experiments using an area detector were carried out on a well oriented thin film sample, which was prepared on silicon substrate. The same diffraction peaks were observed in the GISAXS pattern (see Figure 4.2c). However, with the sample being oriented, diffraction spots (instead of rings) were observed. Compared to the powder SAXS pattern, this provides the critical extra information on the spatial relationship between diffraction peaks in reciprocal space. According to the q ratios and relative position of each observed reflection, this mesophase can be indexed easily on a 3D hexagonal lattice with space group *P6/mmm*, with

the hexagonal axis perpendicular to the substrate surface in the thin film sample. The corresponding index of each reflection is show in both SAXS and GISAXS diffraction patterns. The unit cell parameters a and c are determined to be 41.0 Å and 40.0 Å respectively. The experimental observed and calculated d-spacings are listed in Table 4.2. No change in peak positions is observed between room temperature and 105 ºC. A TEM image along [001] axis of the $P6/mmm$ phase in Figure 4.2d shows the clear hexagonal packing feature of the nanoparticles.
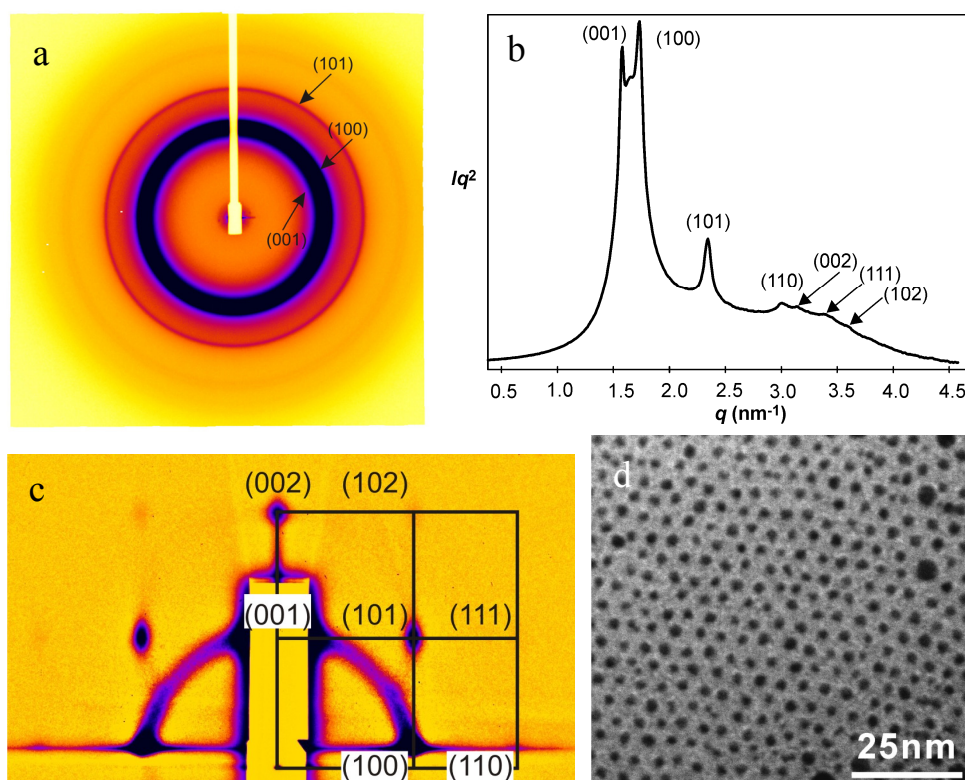

Figure 4.2. a) 2D powder SAXS pattern of sample AuL3 taken at 30 ºC b) 1D spectrum converted from a). c) GISAXS pattern from an oriented thin film sample prepared on silicon substrate. d) TEM of a ca. 50 nm thick film in the $P6/mmm$ phase of AuL3, viewed along [001] axis (Contributed by R. Zhang).

Diffraction intensities (see Table 4.2) measured at 30 ºC using the PeakSolve^{TM}, combined with unit cell parameters and the space group information, were used to reconstruct the electron density map of this structure. During this process the multiplicities of different reflections were taken into account and they are given in Table 4.2 along with the phase combination used for this reconstruction. The electron density map is shown in Figure 4.3a. The high electron density regions (enclosed within green spheres in 3D map, yellow-red in 2D

projections) denote the gold nanoparticles. They are located only at the corners of the hexagonal unit cell as supported by the TEM image of AuL3 (Figure 4.2d). Note that the distances between the GNPs along the six-fold axis (*c*) and normal to it (*a*) are almost the same. Thus one can view the GNP arrangement equally as layers (normal to *c*) or columns (along *c*). This is in contrast to the previously studied systems with mesogens, which form, depending on the length of the co-ligand alkyl chain, either 2D-ordered hexagonal columnar or 3D-ordered rhombohedral superstructure. There the distance between particles along the hexagonal axis is significantly smaller than normal to it.

Table 4.2. Experimental and calculated *d*-spacings and diffraction intensities, including multiplicities and structure factor phase angles. Measured at 30 ºC for the 3D hexagonal phase of sample AuL3.

Peaks (*hkl*)	*d*-spacings (Å)		Intensities		Mult.	Phase angle ϕ
	Exp.	Calc. P6/mmm a=41.0 Å c=40.0 Å	Exp.	Model D_{sphere}=17.9 Å $\sqrt{\langle u^2 \rangle}$ =8.6 Å $\Delta = 4.17*$		
(001)	40.0	40.0	42.39	43.32	2	0
(100)	35.5	35.5	100.00	98.19	6	0
(101)	26.6	26.5	68.76	68.77	12	0
(110)	20.6	20.5	6.92	6.53	6	0
(002)	20.0	20.0	1.29	1.70	2	0
(111)	18.3	18.2	10.13	4.14	12	0
(102)	17.4	17.4	2.07	2.17	12	0

$$*\Delta =100(\sum_{i}\left|I_i^{exp} - I_i^{calc}\right|)/(\sum_{i} I_i^{exp}) .$$

In the GISAXS diffraction pattern the (100) and (110) peaks are observed in the equatorial direction, while the (001) and (002) peaks are seen in the meridional direction. These features indicate that in the oriented thin film the gold nanoparticle columns are perpendicular to the

substrate surface. With the increase of temperature, sharp peaks disappeared and only broad ones are left above 105 ºC, indicating the loss of the positional order of gold nanoparticles and the formation of the isotropic phase.
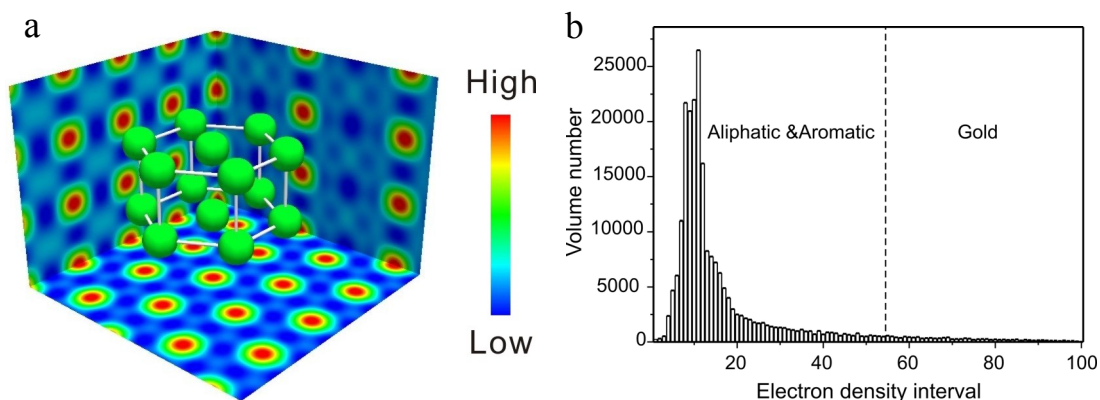

Figure 4.3. a) Reconstructed electron density maps of the *P6*/*mmm* phase in AuL3. b) The corresponding histogram of the electron density map. In this histogram the calculated electron density is divided into 100 segments between minimum and maximum values. The number of volume elements within each intensity interval is calculated as explained in chapter 2.

To determine the size of gold core, chemical analysis was conducted. The elemental analysis result of AuL3 shows the wt % of C, H, S and Au is 36.39 %, 4.38 %, 2.27 % and 51.0 % respectively. Assuming the number of mesogens per Au atom being *n*, then we can calculate the wt % of each element. By comparing with the experimental result we got best fit value *n* = 0.272. According the FCC lattice parameter 4.08 Å of the gold crystal, the volume of each Au atom is 17 Å^3. The volume of each mesogen molecule is 1148 Å^3, taking the density to be 1.0 g cm^{-3}. Thus the volume of each atom with its corresponding mesogens is 329 Å^3. As the unit cell volume for the *P6*/*mmm* phase is 58,230 Å^3, and within which only one nanoparticle is contained. So there are 177 Au atoms in each gold nanoparticle having a corresponding sphere diameter of 17.9 Å, with 48 mesogen molecules attached to it.

The volume fraction *vs.* electron density histogram of the reconstruction is shown in Figure 4.3b and it can be used to monitor the quality of the corresponding reconstructed electron density map. This histogram feature is very reasonable for this hybrid system, as most of the space in a unit cell is taken up by the organic component. The well defined peak at low electron density region is attributed to the organic molecules. Based on the decided gold core

diameter and the size of unit cell, the volume ratio between gold particle and organic part is calculated to be 0.05:0.95 as indicated by the dashed line in the figure.

With the reconstructed electron density map and determined gold nanoparticle size, we proceed to simulate the observed diffraction intensities. To do this a simple 2-level core shell model is built, in which the gold nanoparticles are assumed to be spherical with high electron density surrounded by a continuum of organic part with low electron density. Calculation based on mass density gives the electron densities of gold core, in unit of electrons per Å^3, 4.65; aliphatic, 0.31 and aromatic 0.34. From these results we see the electron density difference between gold and the organic molecule is much larger than the electron density fluctuation between the two organic parts. During simulation, the size of the gold nanoparticle was fixed to the determined diameter 17.9 Å, and a Debye-Waller factor was used to reflect the deviations of gold nanoparticles from their mean positions. The best-fit simulation intensities are compared with the experimental ones in Table 4.2, and clearly this model fits the observed diffraction intensities very well. The mean square displacement of a nanoparticle $\sqrt{\langle u^2 \rangle}$ was found to be 8.6 Å in the best-fit model. The deviation between experimental and simulated intensities was evaluated by equation:

$$\Delta = 100(\sum_i \left| I_i^{exp} - I_i^{calc} \right|)/(\sum_i I_i^{exp}) \qquad (4\text{-}1)$$

where I^{exp} is the experimental intensity measured from the powder diffraction pattern, I^{calc} is the simulated intensity on the basis of core-shell model.

According to the electron density maps, a molecular model of the decorated gold nanoparticles in this self-assembled structure is proposed and schematically shown in Figure 4.4b. As stated before, for this nanoparticle the gold core is functionalized only by mesogenic ligands. These ligands are grafted onto the gold nanoparticle surface *via* short spacers, and this means that the ligands can not go far away from the gold core and hence must follow the curvature of the gold nanoparticle surface. For the previously studied samples AuL4C6 and AuL4C12, the ordered structures can be described as consisting of columns of nanoparticles surrounded by a sheath of axially aligned mesogens, and the interparticle distance along column direction is determined by the length of the co-ligands [157]. However, due to the

lack of co-ligands in AuL3, to fill the space around gold nanoparticles, the ligands should also cover the gaps between neighbouring gold nanoparticles along column direction. As the laterally attached rod-like mesogens have a strong tendency to orient, it is unlikely that the molecules would distribute completely randomly around gold particles. Instead, it is envisaged that they form box-like shell which is composed of vertically parallel aligned mesogens around the equator of the gold core and horizontally aligned mesogens on the top and bottom as indicated in Figure 4.4a and b, and this makes the decorated gold nanoparticles appear almost isotropic. This model is in line with the determined unit cell parameters *i.e.* the almost equivalent intracolumnar (40.0 Å) and the intercolumnar (41.0 Å) gold nanoparticle distances. Also the model proposed here agrees well with the observed lack of the birefringence in this sample under polarized microscope.
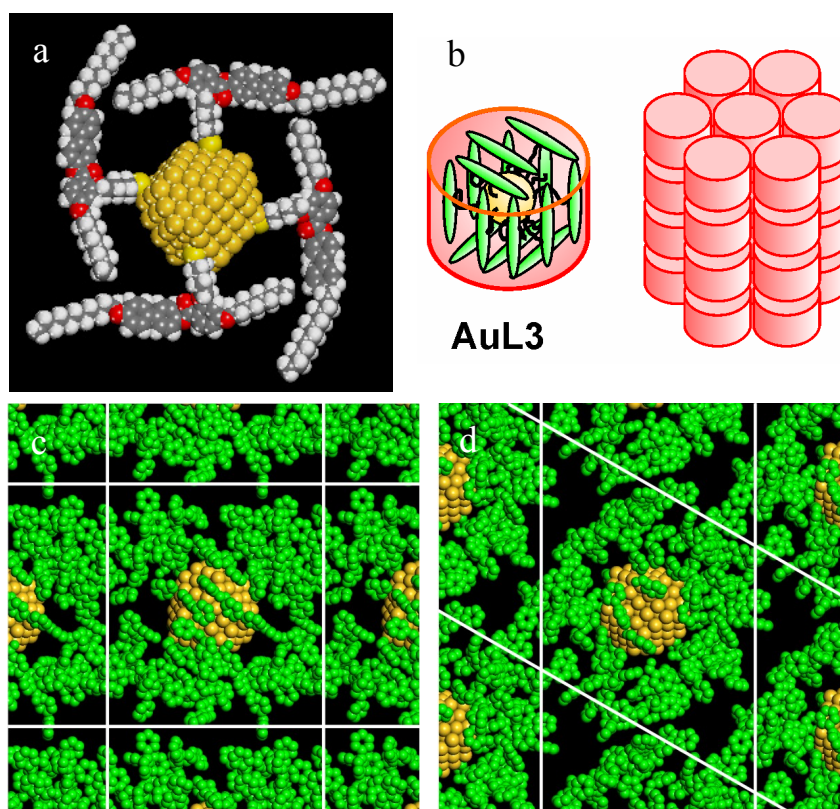
Figure 4.4. a) The mesogen functionalized gold nanoparticle AuL3. b) The schematic model of the arrangement of ligand molecules around a single gold nanoparticle and how such gold nanoparticles self-organize into a 3D hexagonal structure. c) MD annealed molecular model viewed along the [010] axis (side view) and d) along the hexagonal [001] axis (top view). The aromatic cores of the mesogen ligands are shown in green, surrounding the gold nanoparticle; the aliphatic parts are omitted for clarity.

To confirm the arrangement of the mesogenic ligands around the nanoparticles, a molecular model of the *P6/mmm* phase has been constructed and molecular dynamic simulation was carried out following the three steps introduced in chapter 2. The model after dynamic annealing is shown in 4.4c and d. The mesogens surround gold particles with local parallel alignment can be seen and this is in accordance with the model we have proposed.

For sample AuL3C6, gold nanoparticles are functionalized by both mesogenic ligands, and alkyl chain co-ligands. Powder and oriented thin film samples were investigated by small angle X-ray scattering and grazing incidence small angle X-ray scattering methods respectively. Below 45 ℃, three sharp diffraction peaks were observed in the SAXS pattern. The q^2 ratios of these peaks are 1:3:4, and they can be easily assigned to the (10), (11) and (20) diffraction orders of a 2D hexagonal structure with plane group *p6mm*. The unit cell parameter is determined to be 42.3 Å. Along with the three sharp diffraction peaks, a broad hump is observed at *q*-value in between peaks (10) and (11) as shown in Figure 4.5a and b. In the sample partly oriented by shearing, the intensity maximum of the hump is along the shearing direction (horizontal), while the sharp Bragg peaks have maximum in the vertical direction. The same peaks are observed by GISAXS on thin films with improved orientation, with sharp Bragg peaks observed on the equator (horizontal) and the broad hump on the meridian (vertical). (see Figure 4.5c). Under polarized microscope this mesophase shows distinctive nematic texture after annealing at 40 ℃ overnight (Figure 4.5d).

The experimental and calculated *d*-spacings of the observed reflections are listed in Table 4.3. Electron density map of this 2D hexagonal structure is reconstructed using the diffraction intensities measured from powder SAXS pattern. The phase combination used for this reconstruction is also given in Table 4.3. The electron density map (Figure 4.5e) indicates that the GNPs form columns that pack on a hexagonal lattice without long-range correlation along the column axis. In this reconstruction the electron density distribution is visualized by different colours. The purple-blue regions are the high density areas contributed by the gold cores, around which are the low electron density continuum (red colour) containing the organic parts of the particles. In the electron density map the hexagon lattice formed by the gold nanoparticles can be clearly seen, which is also confirmed by the TEM image as shown in Figure 4.5f.
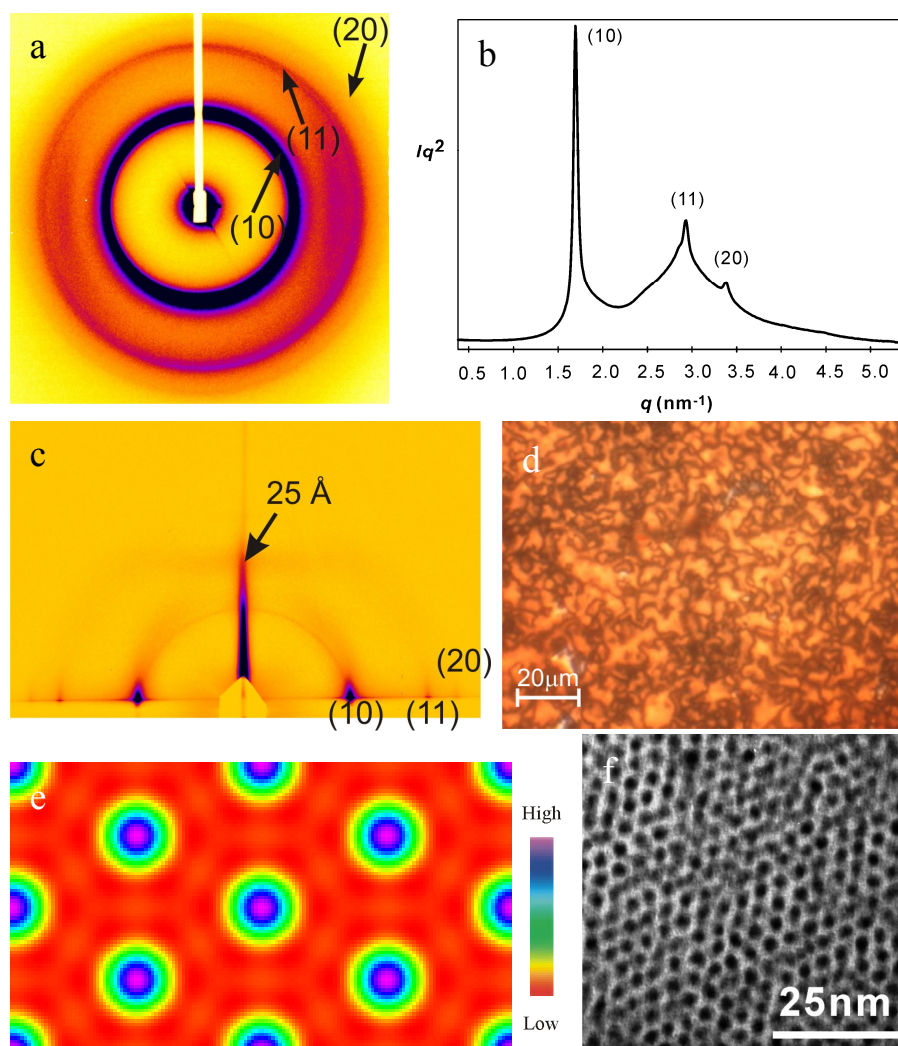
Figure 4.5. a) Small angle X-ray scattering pattern of AuL3C6, slightly oriented by shear and recorded at 30 ºC (shear direction horizontal). b) 1D spectrum converted from a). c) GISAXS pattern from an oriented thin film. d) Micrograph of AuL3C6 between crossed polarizers at 25 ºC, after annealing at 40 ºC overnight, showing a typical nematic Schlieren texture. e) Reconstructed electron density map – view along the columns of GNPs (purple-blue-green regions GNP, red organic). f) TEM of a ca. 50 nm thick film of the *p6mm* phase, showing the hexagonal packing of nanoparticle columns (Contributed by R. Zhang).

In the GISAXS pattern all the Bragg peaks (10), (11) and (20) situated on the equator, which means in thin film sample the nanoparticle columns are oriented perpendicular to the substrate surface. Besides these sharp peaks, one weak diffuse scattering maximum is observed in the meridional direction. The central position of it corresponds to a *d*-spacing of 25.0 Å, representing the average distance between neighbouring gold nanoparticles in the same column *i.e.* the intracolumnar particle distance.

Table 4.3. Experimental and calculated *d*-spacings and diffraction intensities, including multiplicities and structure factor phase angles of the 2-D hexagonal phase in AuL3C6 at 30 ºC.

Peaks (*hk*)	*d*-spacings (Å)		Intensities		Mult.	Phase angle ϕ
	Exp.	Calc. *p6mm* a=42.3 Å	Exp.	Model D_{sphere}=16.2 Å $\sqrt{\langle u^2 \rangle}$ = 6.9 Å Δ = 1.64*		
(10)	36.6	36.6	100.00	100.25	6	0
(11)	21.1	21.1	16.11	16.59	6	0
(20)	18.3	18.3	7.61	6.31	6	0

*Δ= $100(\sum_i \left| I_i^{exp} - I_i^{calc} \right|)/(\sum_i I_i^{exp})$.

Elemental analysis, combined with NMR data, indicate that for the AuL3C6 there are 0.189 mesogens and 0.189 co-ligands per Au atom. According to molecular weight, assuming density of 1.0 g cm^{-3}, the volume of a mesogen and a co-ligand is 1287 Å^3 and 196 Å^3 respectively. Thus the volume of each gold atom with its corresponding mesogens and co-ligands is 297 Å^3. As the unit cell volume is 38738 Å^3, there are 130 Au atoms in each gold nanoparticle corresponding to a sphere diameter 16.2 Å, with 25 mesogen and 25 co-ligand molecules attached. Simulation of the diffraction peaks has been carried out based on a core-shell model which is the same as mentioned before, giving the simulated intensities listed in Table 4.3. In the simulation of the diameter of gold core was fixed at 16.2 Å, as calculated above. Best-fit is achieved for a mean displacement of the nanospheres of 6.9 Å, *i.e.* 16 % of the intercolumnar spacing.

In AuL3C6, the structural model of the ordered phase suggests that the ligands and co-ligands can redistribute around the GNP surface, particularly if the system is annealed at elevated temperatures, where breakage and re-establishment of S-Au bonds becomes frequent. We suggest that in the hexagonal columnar phase of AuL3C6 the ligands congregate around the equator of the gold nanosphere, thereby allowing the uniaxial nematic-like alignment of the aromatic mesogens. At the same time the co-ligands aggregate near the north and south poles as indicated in Figure 4.6a and b, which is consistent with the molecular model after dynamic

simulation (Figure 4.6c and d). This enables the nanoparticles to align in strings wrapped in the sheaths of uniaxially oriented mesogens, and packed on a hexagonal lattice. As expected, the center-to-center distance between nanoparticles within a column is significantly shorter (observed 25.0 Å) than that between neighbouring columns (observed 42.3 Å).
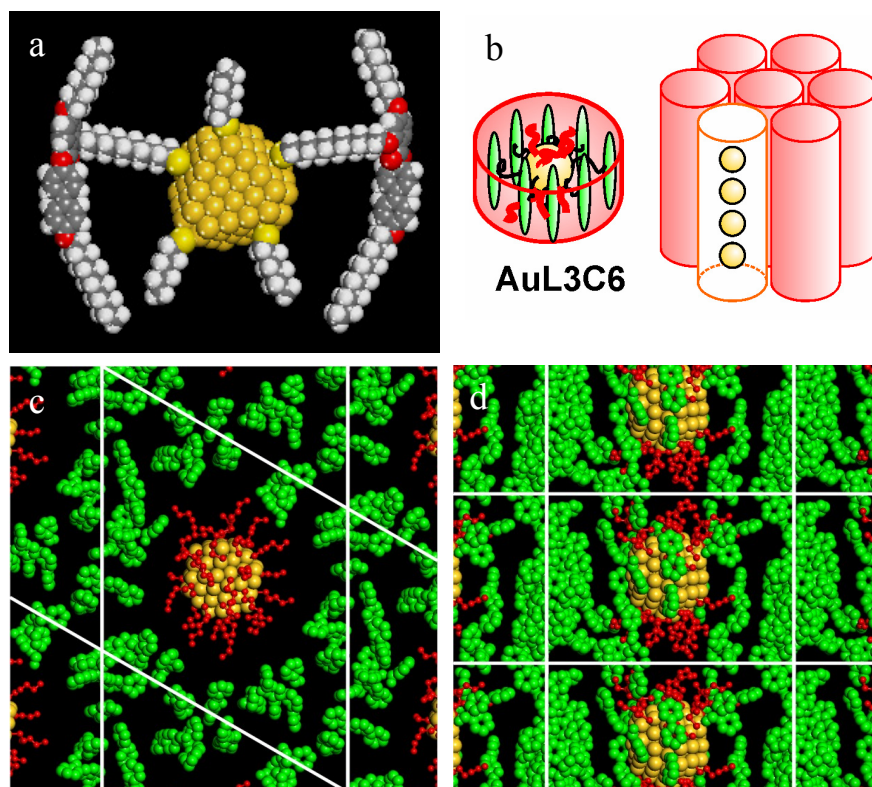

Figure 4.6. Structure models of sample AuL3C6. a) Mesogenic ligand and alkyl chain co-ligand functionalized gold nanoparticle. b) Model of the arrangement of ligands and co-ligands around a single gold nanoparticle and how such gold nanoparticles form the 2D hexagonal structure. c) MD annealed molecular model viewed along GNP columns (top view) and d) along the hexagonal [10] axis (side view). Aromatic cores of the mesogen ligands are shown in green (CPK) and the co-ligands are shown in red (ball-and-stick), surrounding the gold nanoparticle; the aliphatic parts of the ligands are omitted for clarity.

This model of wrapped GNPs forming strings is similar to the experimental results observed earlier for GNPs functionalized with longer mesogens and containing either hexyl or dodecyl ligands [157]. The lack of true long range order along the columns could be due to the presence of some polydispersity of the nanoparticles; because of the particles along the string nearly touching, the unevenness in size may result in aperiodicity along the columns.

Above 45 ºC, AuL3C6 loses birefringence and long-range columnar order. In SAXS only two diffuse peaks are observed, with the corresponding *d*-spacings centred around 36.0 and 21.0 Å. As this ratio is close to $3^{1/2}$, it is likely that fragments of GNP columns still persist, with local hexagonal arrangement.

Sample AuL3C12 is functionalized by the same mesogenic ligands as in sample AuL3C6 but different co-ligands. In this case the co-ligands are changed from hexylthiol to dodecylthiol. The as-prepared AuL3C12 sample shows no birefringence at all. The powder SAXS spectrum (Figure 4.7a) is very similar to that of AuL3C6 above 45 ºC with two rather broad peaks around 41.2 Å and 24.0 Å. The ratio is again $\sim 3^{1/2}$ corresponds to the relationship of (10) and (11) in hexagonal structure with plane group *p6mm* and unit cell parameter 47.6 Å. No improvement in order occurred after annealing at temperatures up to 170 ºC. This X-ray diffraction feature suggests that the gold nanoparticles probably form short columns with a local hexagonal packing. A reconstructed electron density map, using powder diffraction intensities and the phase angles in Table 4.4, is shown in Figure 4.7b. The high electron density regions of the electron density map are indicated by purple-blue colour and are contributed by gold cores, around which is the low electron density continuum of the organic parts. No diffraction information could be obtained about the order along column direction. Based on chemical analysis (details will be given later) the diameter of the gold core was calculated to be 22.7 Å.
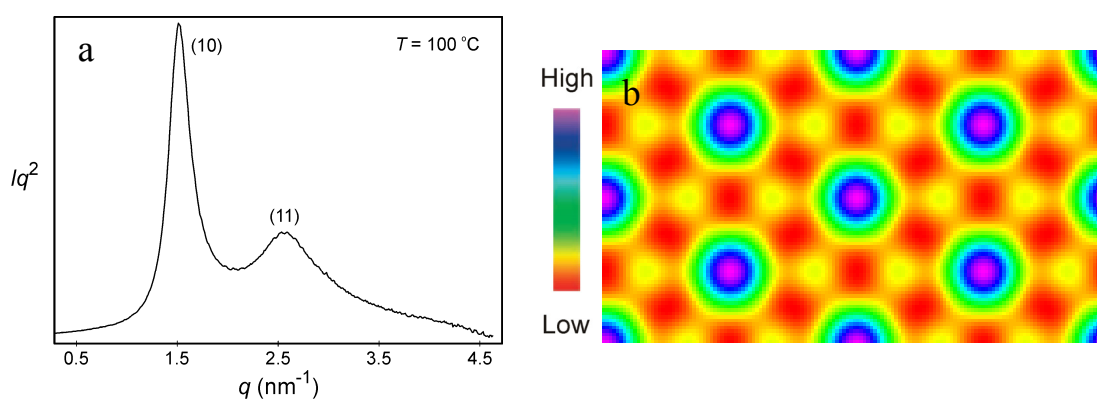

Figure 4.7. a) Powder Diffraction pattern of sample AuL3C12, and b) the reconstructed electron density map of the 2D hexagonal structure.

Table 4.4. Experimental and calculated d-spacings and diffraction intensities, including multiplicities and structure factor phase angles of the 2D hexagonal phase of AuL3C12 at 100 ºC.

Peaks (*hk*)	d-spacings (Å)		Intensities		Mult.	Phase angle ϕ
	Exp.	Calc. *p6mm* a=47.6 Å	Exp.	Model D_{sphere}= 25.7 Å $\Delta = 5.8$*		
(10)	41.2	41.2	100.0	99.9	6	0
(11)	24.0	23.8	20.5	13.1	6	0

*$\Delta=100(\sum_i \left| I_i^{exp} - I_i^{calc} \right|)/(\sum_i I_i^{exp})$.

Since no long range ordered phase was found in powder and in normally annealed thin film, vapour annealing is used to help develop order in the thin film sample prepared on silicon substrate. In this case, the sample was first dissolved in chloroform with weight concentration of 1 %. Thin film is then prepared on the surface of silicon wafer by drop casting followed by annealing in chloroform vapour for 24 hours. After the solvent completely evaporated a thin film of nanoparticles formed on top of the substrate surface. The GISAXS pattern of the film thus treated, recorded at 120 ºC, is shown in Figure 4.8a. In addition to the diffuse scattering rings at the same q-values as in the powder SAXS, sharp Bragg diffraction peaks are prominent (spots superposed on Debye rings).

The q^2 ratios of these sharp GISAXS reflections are 3: 4: 8: 11: 12, which indicate a face centre cubic (FCC) structure. According to the d-spacings the best-fit unit cell parameter a is 76.4 Å. These observed diffraction peaks fully obey the reflection conditions that h, k, l are permutable with *hkl*: $h + k$, $h + l$, $k + l = 2n$; *0kl*: k, $l = 2n$; *hhl*: $h + l = 2n$ and *h00*: $h = 2n$. The space group with the highest symmetry whose extinction rules agree with the experimental observation is $Fm\overline{3}m$. Since for liquid crystal system the molecules with high mobility always have the tendency to form structure with the highest symmetry, the space group $Fm\overline{3}m$ is assigned to this cubic phase. The different index colours shown in the diffraction pattern represent two different orientations of domains. The black ones come from the orientation

with [111] lattice planes parallel to the substrate surface, while the blue ones come from the orientation with [220] lattice planes parallel to the substrate surface.
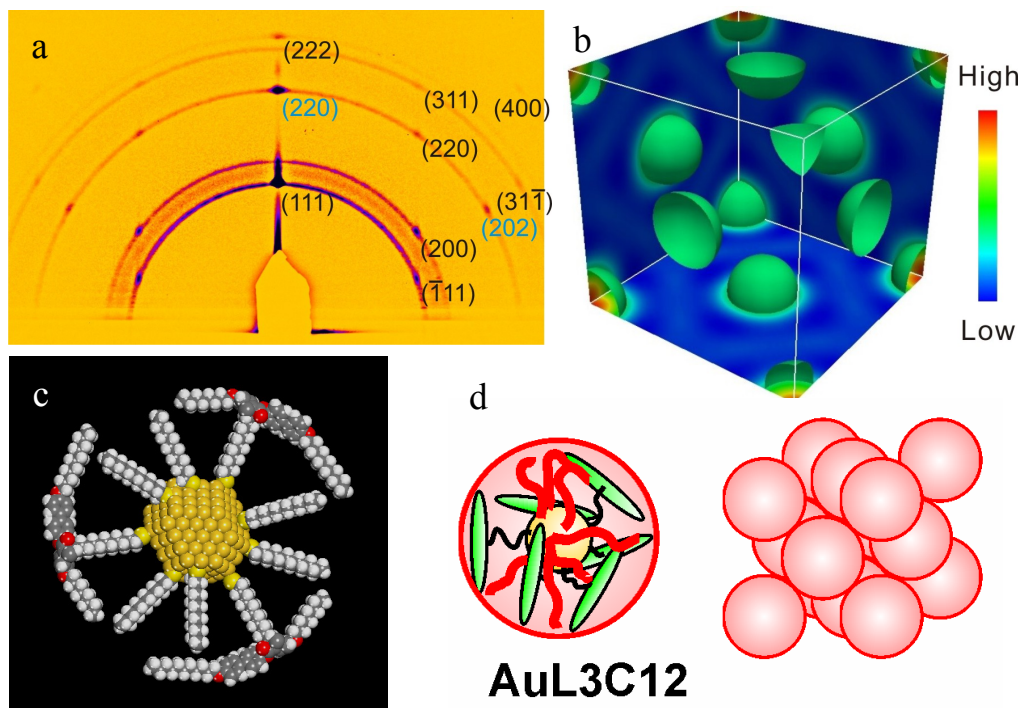

Figure 4.8. a) GISAXS diffraction pattern of a solvent vapour-annealed thin film of AuL3C12 recorded at 120 ºC. Sharp Bragg diffraction maxima can be indexed to an FCC lattice. b) Reconstructed electron density map of the FCC phase, the iso-electron surfaces enclosing the high electron density region of gold nanoparticles. c) Mesogenic ligand and alkyl chain co-ligand functionlized gold nanopartilce. d) Model of arrangement of ligands and co-ligands around a single gold nanoparticle and how they arrange to form the FCC phase.

With diffraction pattern indexed and space group determined, the electron density map of this structure can be reconstructed using measured diffraction intensities. In the case of GISAXS pattern, the 1D diffraction spectrum of each reflection can be obtained separately with FibreFix (CCP13). These spectra can then be used to obtain diffraction intensities by employing the PeakSlove^{TM} software. Since the fibre-like feature of the thin film sample, intensity of each reflection was corrected by multiplying its value by q_{xy} prior to the reconstruction of electron density map. The final intensities and phase angles listed in Table 4.5 were used to reconstruct electron density maps (Figure 4.8b). This reconstruction clearly

shows the face centre cubic structure, in which the gold nanoparticles are located at the corners and face centres of the cubic unit cell.

Table 4.5. Experimental and calculated *d*-spacings and diffraction intensities, including multiplicities and structure factor phase angles of this face centre cubic structure of sample AuL3C12.

Peaks (*hkl*)	*d*-spacings (Å)		Intensities		Mult.	Phase angle ϕ
	Exp.	Calc. $Fm\bar{3}m$ a=76.4 Å	Exp.	Model D_{sphere}= 22.7 Å $\sqrt{\langle u^2 \rangle}$ = 4.4 Å $\Delta = 5.36^*$		
(111)	44.1	44.1	100	100.0	8	0
(200)	38.3	38.2	53.7	59.6	6	0
(220)	27.0	27.0	45.1	43.5	12	0
(311)	23.0	23.0	34.1	37.0	24	0
(222)	22.1	22.1	11.7	9.0	8	0

$$* \ \Delta=100(\sum_i \left| I_i^{exp} - I_i^{calc} \right|)/(\sum_i I_i^{exp}).$$

Element analysis of AuL3C12 shows the wt % of C, H and S are 34.53 %, 4.65 % and 1.85 %, respectively. Assuming the number of mesogens per Au atom being *n* and the number of co-ligand per Au atom being *m*, from NMR the *m/n* was found to be 0.64, then based on the wt% of these elements the best fit gives *n* = 0.1840, *m* = 0.1178. According to thermo gravimetric analysis (TGA), the weight percentage of Au is 53 %. With the knowledge of the density of Au 19.3 g cm^{-3} and taking organic part density 1.0 g cm^{-3}, we know the volume ratio of Au is 5.52 %. Since the unit cell parameter of the FCC structure is 76.4 Å and there are four nanoparticles in each unit cell, so the volume of each nanoparticle including the organic parts is 111486 Å^3, which means the volume of each gold nanoparticle is 6154 Å^3 corresponding to sphere diameter 22.7 Å, with the numbers of ligand and co-ligand molecules per gold nanoparticle are thus 67 and 43, respectively.

In the simulation of the diffraction pattern of AuL3C12 the GNP diameter was fixed at 22.7 Å as calculated above. The resulting best-fit mean square displacement of the nanospheres is 4.4 Å, *i.e.* 8 % of the nearest interparticle distance. Fairly good fit between the calculated and experimental intensities is achieved. Calculated intensities are compared with experimental ones in Table 4.5.
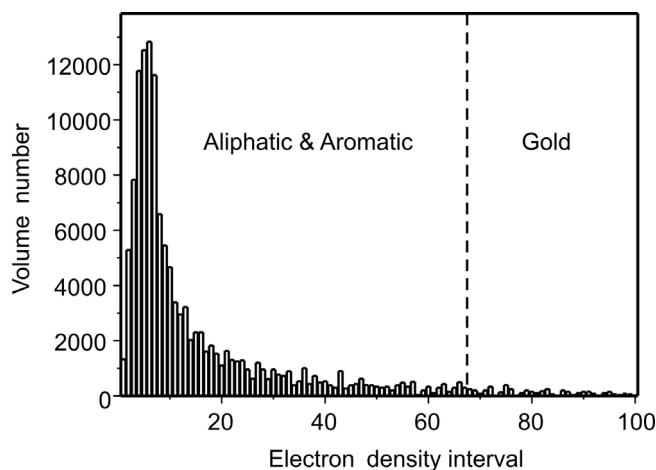

Figure 4.9. Volume number *vs.* electron density histogram of the face centre cubic phase. The dashed line indicates the boundary between high electron density gold core and low electron density organic components.

The volume fraction *vs.* electron density histogram is shown in Figure 4.9, in which the sharp peak appeared at low electron density region means most of the space in a unit cell is occupied by organic components. Taking the above determined volume fraction 5.52 % of the gold core in this FCC structure, then the remaining space is taken up by aromatic and aliphatic as indicated by the dashed line in the histogram. According to mass density calculation, the electron density fluctuation between the two organic parts is two orders of magnitude smaller than the electron density difference between gold and them. On the other hand, the aromatic and aliphatic parts are expected to mix in the real structure, so they together form the low electron density continuum between gold nanoparticles.

4.4 Nanostructures Formed by GNPs Covered with Chiral Mesogens

For sample AuCholC6 the co-ligands used are hexylthoils while the mesogenic ligands are completely different from previous samples as shown in Table 4.1. Ordered mesophase of this sample was observed from room temperature to 90 ºC.

Small angle X-ray scattering experiments were carried out on powder sample. The sharp diffraction peaks shown in Figure 4.10a and b indicate the existence of ordered arrangement of gold nanoparticles. Grazing incidence small angle X-ray scattering method was also used to help index this structure. In this case the sample was prepared as thin film on the surface of a silicon substrate. To get better orientation the thin film sample was cooled from 140 to 30 ºC with a cooling rate of 0.2 ºC/min under vacuum conditions. The GISAXS pattern recorded by area detector is shown in Figure 4.10c. The observed reflections here correspond to the powder pattern very well except the intensity maximum close to the origin of reciprocal space. Up to now it is not clear where it came from. However, this maximum was found to be present even beyond the isotropic temperature of the sample, indicating that it did not originate from the current mesophase. From GISAXS pattern we see that after long time annealing the orientation of the thin film sample was improved even though the ring-like feature of the reflections can still be seen.

Combining the powder SAXS and oriented thin film GISAXS results the diffraction pattern of this structure can be indexed on a 2D oblique lattice, in which the unit cell parameters a, b equals 45.2 Å, 52.7 Å respectively and the angle between the two axes is 57.0º. The index of each reflection is shown on top of the diffraction patterns and the corresponding d-spacings are given in Table 4.6. The central position of the hump besides (10) observed in powder diffraction pattern corresponds to a d-spacing of 37.0 Å, which might come from the third dimension positional correlation of gold nanoparticles. However, this correlation must be very weak, as no higher order reflections could be observed in this direction.

Electron density map of this structure was reconstructed using the diffraction intensities measured from powder diffraction pattern. In this pattern the higher order peaks with almost

equivalent *d*-spacings are overlapped and it is hard to tell the intensity difference between each other. On the other hand, the pronounced background in the higher order region makes it difficult to measure their intensities accurately. Taking these into account, only diffraction intensities of the first three lower order sharp peaks were used to reconstruct the electron density map. The measured intensities and phase combination for this reconstruction are listed in Table 4.6.
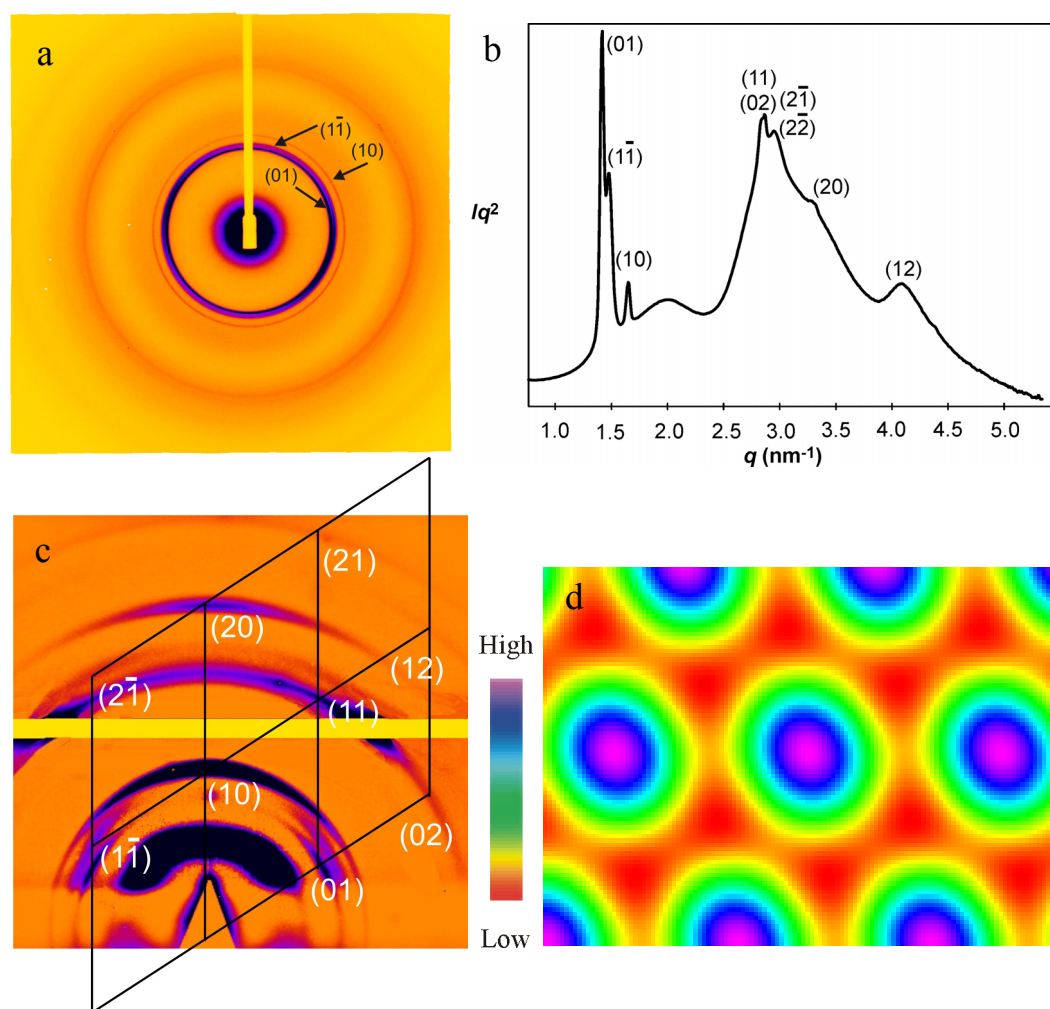

Figure 4.10. a) Small angle X-ray scattering pattern of sample AuCholC6 taken at 30 ℃. b) 1D spectrum converted from a). c) GISAXS pattern from an oriented thin film. d) Reconstructed electron density map from experimental results using the first three low order reflections.

The reconstructed electron density map is shown in Figure 4.10d. The purple-blue colour represents the high electron density regions contributed by the gold nanoparticles and each gold nanoparticle is surrounded by low electron density regions indicated by the red colour

which are contributed by organic molecules. Comparing the electron density maps of this structure with the one of the 2D hexagonal structure found in sample AuL3C6, the similarity between these two indicates the gold nanoparticles in this oblique lattice also form columns with the gold strings along the column axes. However, it seems in this current 2D structure the columns packed on a distorted hexagonal lattice, in which the gold columns may arrange with their axis tilted at an angle with respect to the substrate surface. This might be caused by the configuration of the chiral ligand molecules attached.

Table 4.6. Experimental and calculated d-spacings and diffraction intensities, measured at 30 ºC, including multiplicities and structure factor phase angles. Calculated intensities from best-fit two-level model are also listed.

| Peaks (*hkl*) | d-spacings (Å) | | Intensities | | Mult. | Phase angle ϕ |
	Exp.	Calc. $P2$ $a = 45.2$ Å, $b = 52.7$ Å, $\gamma = 57.0º$	Exp.	Model $D_{sphere} = 22.0$ Å $\sqrt{\langle u^2 \rangle} = 7.3$ Å $\Delta = 0.47*$		
(01)	42.2	44.2	100	99.96	2	0
(1$\bar{1}$)	42.3	42.4	90.57	91.62	2	0
(10)	37.9	37.9	72.49	72.34	2	0
(02)	22.0	22.1	-	-	2	-
(2$\bar{2}$)	21.2	21.2	-	-	2	-
(20)	19.0	19.0	-	-	2	-
(12)	15.6	15.7	-	-	2	-

$$ * \Delta = 100 (\sum_i \left| I_i^{exp} - I_i^{calc} \right|)/(\sum_i I_i^{exp}) . $$

Simulation of diffraction intensities was conducted based on a core-shell model. During simulation a Debye-Waller factor was used and the mean square displacement $\sqrt{\langle u^2 \rangle}$ was

found to be 7.3 Å in the best-fit model. The best fit intensities and phase combination is given in Table 4.6. From the best-fit model, the diameter of gold core is found to be 22.0 Å.

4.5 Conclusion

In this chapter, liquid crystalline molecules functionalized gold nanoparticles synthesized *via* the Brush-Schiffrin method have been studied. The self-assembled nanostructures of these decorated gold nanoparticles were investigated by small angle X-ray scattering and grazing incidence small angle X-ray scattering methods. Normal nematic liquid crystalline molecules and molecule that possesses cholesteric nematic phase have been introduced to the hybrid system. Different structures were found from these functionalized gold nanoparticles.

For gold nanoparticles covered with nematic forming mesogens, three different self-assembled phases with long-range positional order are observed. One of them, the simple hexagonal 3D packing, has not been observed in any LC system, and the other one the face-centered cubic phase is the first occurrence reported in thermotropics. The current results indicate the presence and amount of co-ligands in the system is found to be critical in determining the exact mode of self-assembly of such nanoparticles. It seems there is an upper and lower limit of co-ligand volume within which rod-like mesogenic ligands are able to impose anisotropy on the self-assembly of sphere-like nanoparticles. With too little (sample AuL3) or too much co-ligand (sample AuL3C12) the mesogens are either too tightly wrapped around the particle, or too dilute, to achieve long-range orientational order and impose anisotropy on the packing of nanoparticles.

In sample AuL3, there is no co-ligand around gold nanoparticle (Figure 4.11 left). To fill the space mesogens have to crowd around gold particles and also follow the curvature of the particle surface. However, since the tendency of parallel alignment of the rigid units, a completely random arrangement of the molecules is impossible. As a result, a box-like shell with parallel aligned mesogens in each facet formed around the gold core. This mesogen arrangement makes the final decorated particles nearly isotropic, thus after they packed on a simple 3D hexagonal lattice the unit cell parameters of a (41.0 Å) and c (40.0 Å) are almost equivalent. The lack of birefringence of this sample also proves the isotropic-like feature of the decorated gold nanoparticles.
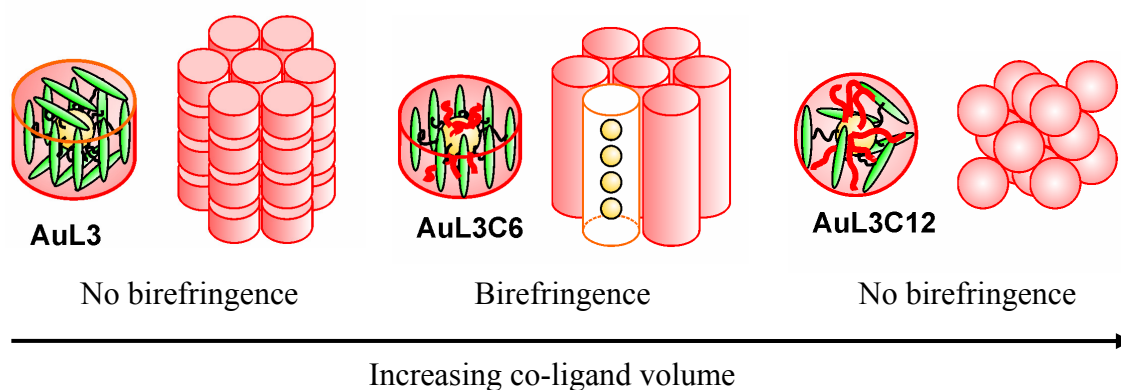
Figure 4.11. Schematic illustration of the different arrangements of ligands and co-ligands around a nanoparticle depending on the relative amount of co-ligand and of the different resulting types of ordered self-assembly.

If co-ligands were used (AuL3C6, Figure 4.11 middle), the obtained mesophase can be described as the packing of gold nanoparticle columns on 2D hexagonal lattice. In each column the gold string forms the column axis which is surrounded by mesogens with uniaxial nematic-like alignment, and at the same time the co-ligands aggregate near the north and south poles. In this case the gaps between neighbouring gold nanoparticles in the same column are mainly filled by co-ligands as shown in the model. So the intracolumnar particle distance is tunable, depending on the co-ligand volume. These gold columns then packed on different lattices forming structures with anisotropic optical properties, for example birefringence.

Further increase of the co-ligands volume leads to the conversion of every single decorated gold nanoparticle from anisotropic to isotropic-like particle (AuL3C12, Figure 4.11 right), as the rod-like mesogens are diluted by the co-ligands which do not possess liquid crystalline properties. So the arrangement of gold nanoparticles was not affected by the mesogens during self-assembly and thus a typical close packing of face centre cubic structure with no birefringence was found in this sample.

For gold nanoparticles covered with chiral molecules (sample AuCholC6), a 2D oblique structure has been found. It seems in this structure the gold nanoparticles also form columns with gold strings along column axes. However, comparing the reconstructed electron density

map with the one of the 2D structure found in AuL3C6, it indicates that in this structure the gold columns packed on a distorted hexagonal lattice with the column axes tilted at an angle with respect to the substrate surface. This might be caused by the chiral property of the end attached mesogens.

These results presented here on AuL3 series, combined with previous results on AuL4 series, point to effective ways of controlling anisotropic self-assembly of organic-inorganic hybrid systems for variety of applications.

Chapter 5 Study of Gold Nanoparticle Arrays by Grazing Incidence Small Angle X-ray Scattering Method

5.1 Introduction

Metallic nanoparticle containing polymer composites are of particular interest for their controllable electronic and optical properties [158-160]. As novel nanocomposites, assemblies of multilayered polyelectrolyte (PE) films which are alternated by nanoparticle inclusions have been widely investigated due to their applications in catalysis, biocompatibility and biosensor technology [161-162]. Several methods have been developed over the past years to obtain such layered material. Comparing with traditional Langmuir-Blodgett [163] or chemisorption strategies [164], layer by layer technique has gathered more and more attention due to its simplicity, versatility and robustness for fabricating well defined metal/polymer layer structures [165].
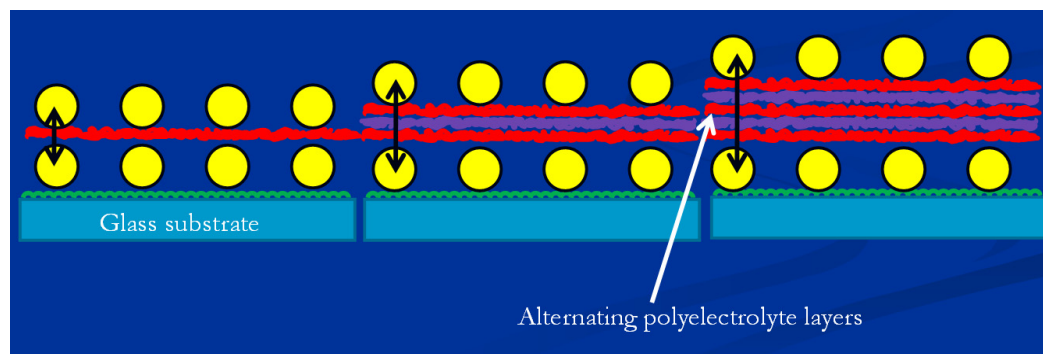

Figure 5.1. Simple schematic drawing of models of layered samples with different number of polyelectrolyte layers between two gold nanoparticle layers [166].

In this chapter the morphology of gold nanoparticle arrays which were prepared on glass substrates *via* layer by layer technique has been investigated by grazing incidence small angle X-ray scattering method. The samples involved in this chapter were provided by Dr A. Cunningham [167]. Briefly, in order to obtain multilayered gold arrays, both the substrate and gold nanoparticles need to be pre-treated so that they are equipped with opposite charges. Polyelectrolyte layer, which can be either positively or negatively charged, was introduced to

control the separation of two gold nanoparticle layers. After surface treatment, the positive charge of the terminal amine group on the functionalized glass substrate allows the deposition of negatively charged gold nanoparticles which form the first gold layer. Similarly, the positively charged PE layers can be deposited on gold nanoparticle layer or negatively charged PE layers. Therefore the deposition of the second or even more gold nanoparticle layers is possible after an odd number of oppositely charged PE layers, and gives rise to multilayered structures in which the distance between two gold nanoparticle layers is tunable depending on the number of PE layers used. Models of the layered structure are shown in Figure 5.1, where the yellow spheres represent gold nanoparticles which are separated into two layers by different number of polyelectrolyte layers in between. By repeat depositing of oppositely charged layers a true 3D materials can eventually be obtained. For this kind of gold arrays, the coupling of plasmonic resonances as a function of the separating distance between two gold nanoparticles arrays has been observed and theoretically simulated as well as the effect of particle size on the this system [167].

In the following section discussion will be focused on four multilayered samples which were prepared on glass substrate, and each of them contains two gold nanoparticle layers separated by different number of PE layers in between. The number of PE layers used in the four samples is 5, 11, 15 and 21, respectively.

5.2 Results and Discussion

Grazing Incidence Small Angle X-ray scattering studies were carried out on the four samples, and for each sample a series of diffraction patterns were recorded with different X-ray incident angles. For sample on substrate of such kind there might be two critical angles for the X-ray beams when they go through the sample, one is at the air-sample surface and the other one is at the sample-substrate surface as indicated in Figure 5.2. Normally, we use the incident angle α_i slightly above the first critical angle to make sure the X-ray beam goes into the sample so we have better scattering intensity, and at the same time the splitting of the diffraction peaks due to the total reflection at the sample-substrate interface is not so drastic as to keep the essential features of the GISAXS pattern intact, also to keep the horizon low and cover larger q-range in the GISAXS pattern. With the increasing of the incident angle the splitting of peaks in the diffraction pattern becomes more and more obvious until the angle of

γ is larger than the critical angle at the sample-substrate surface, in which case the reflected beam from the sample-substrate surface disappears and the intensity comes from the scattering of primary beam by the sample.
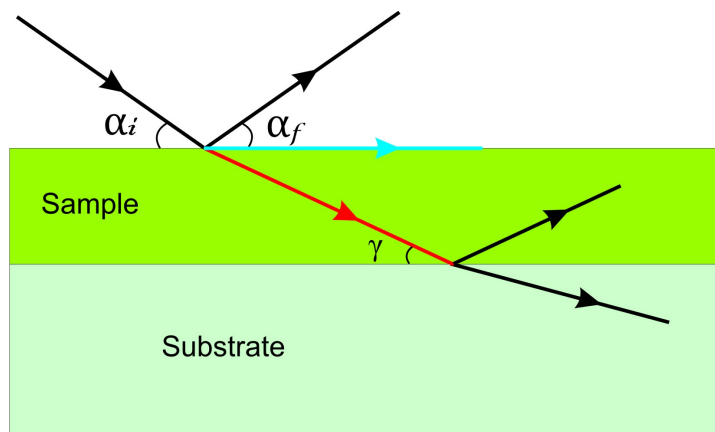

Figure 5.2. The schematic drawing of the path of X-ray beam goes through thin film sample on substrate.

The GISAXS patterns of the four samples shown in Figure 5.3 are recorded with the incident angle just above the critical angle at the air-sample surface. We can see very similar diffraction patterns are observed from the four samples. All of them are mainly characterized by the ring-like feature which is decided by the size and shape of nanoparticles. It was found that for all of the four samples with the increase of incident angle the ring-like feature becomes more and more intense, and then the vertical broadening of the rings appeared due to the reflected beam from the sample-substrate surface and this is quite obvious especially in the regions close to the meridian. At even higher incident angle which we presume is above the critical angle at the sample-substrate surface, different scattering patterns were observed and they will be shown later. Assuming that the gold nanoparticles are spherical with uniform density inside then the ring-like feature can be fitted theoretically by calculating the form factor of spherical particle. This is because the peak positions are determined by the size of particles, by adjusting the peak positions of form factor and that of the experimental GISAXS pattern the particle size can be determined. According to the best-fit, the diameter of the nanoparticles in all the four samples is found to be 13.0 ± 0.5 nm. In Figure 5.3 the GISAXS patterns are converted to 1D spectra *via q* vector scan using the FibreFix (CCP13) and also the form factor of sphere with diameter of 6.5 nm is shown (red curve). By using the diameter of different size the theoretical curve of the form factor may shift horizontally along both

directions, depending on increasing or decreasing the diameter. This might be the reason why the troughs of the experimental results are not zero which indicates the polydispersity of the particle size. Also as we can see although the number of the polyelectrolyte layers in each sample is different, the peak positions of the four samples are almost the same, and this further confirms that the ring-like feature in these diffraction patterns is generated by the gold nanoparticles.
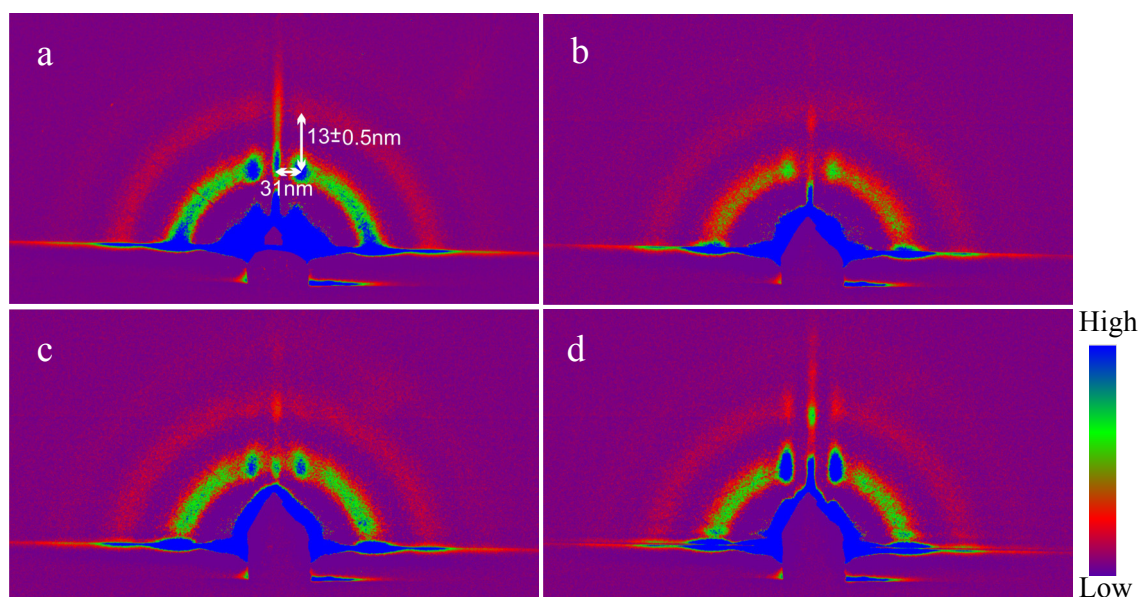

Figure 5.3. The GISAXS patterns of the samples with (a) 5, (b) 11, (c) 15 and (d) 21 polymer layers in between the two nanoparticle layers.

In addition, in each of the four diffraction patterns two streaks are observed at both sides of the meridian. With the increase of the polyelectrolyte layers between the two gold nanoparticle arrays these streaks become more and more obvious, and this feature originated from the positional correlation between gold nanoparticles in the same layer. By calculating the distance of the streaks away from the meridian, the average sideway distance between gold nanoparticles is determined to be 31 nm as indicated in Figure 5.3a, and this value is found to be the same in all of the four samples.
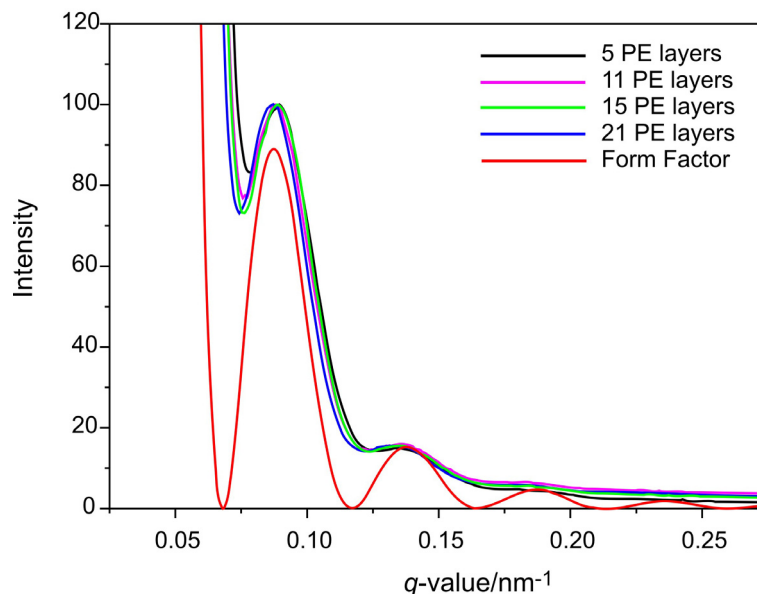
Figure 5.4. The one dimensional spectrum of the grazing incidence small angle X-ray scattering patterns, which are converted from GISAXS patterns corresponding to Figure 5.3. The theoretical calculation of a sphere form factor with the diameter of 6.5 nm is shown as red curve.

By increasing the X-ray beam incident angle, information about the correlation between the two gold nanoparticle layers can be better seen. The higher angle GISAXS patterns of the four samples are shown in Figure 5.5 (left hand side), where splitting in the vertical direction can be seen in the two streaks. Such splitting can only be observed at high incident angles and is barely visible for the sample with only 5 polymer layers, but is much clearer shown for the other three samples (Figure 5.5 right hand side). This is because at higher incident angles the X-ray beam can penetrate the sample deeper and reach the second gold nanoparticle layer as indicated in Figure 5.2, as consequence, the correlation between the two gold nanoparticle layers can be investigated. According to the GISAXS pattern, the distance between the two nanoparticle layers can be determined for the three thicker samples to be 40.0 nm, 49.0 nm and 65.0 nm respectively as indicated in Figure 5.5.

These obtained distances between the two nanoparticle layers seem to correspond very well with the model shown in Figure 5.1. As the expected thickness of each polyelectrolyte layer is 2.6 nm. This thickness is controllable but likely to be affected and tend to be smaller during fabrication [168-169]. Based on the determined diameter 13.0 nm of the gold nanoparticle, assuming that the thickness of each polyelectrolyte layer is 2.5 nm, the calculated distance

between the two gold nanoparticle layers are 40.5 nm, 50.5 nm and 65.5 nm respectively. These theoretical values correspond to the experimental results very well as depicted in Figure 5.6, and as one would have expected the distance between the two gold nanoparticle layers has a linear relationship with the number of polyelectrolyte layers in between them.
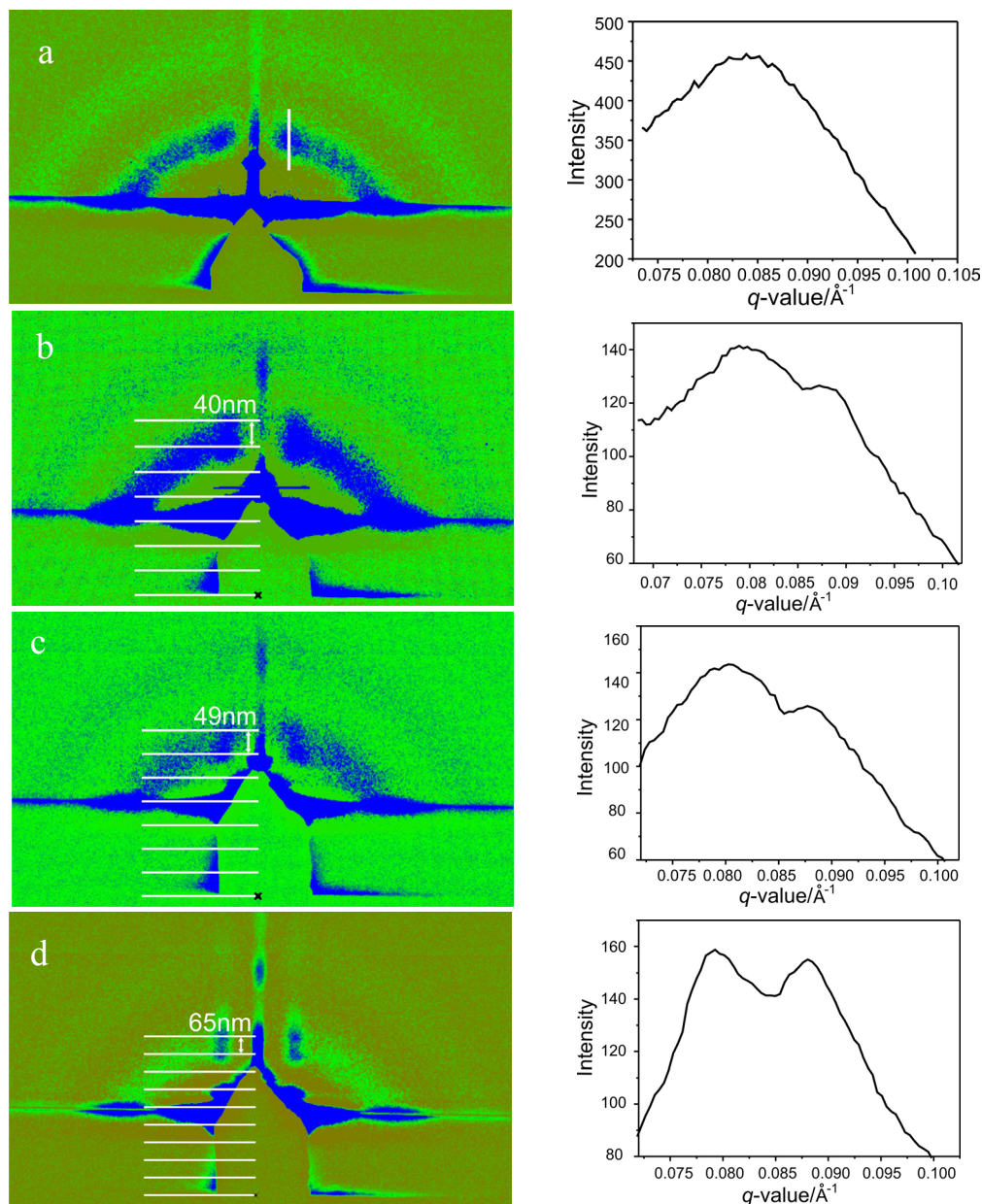

Figure 5.5. GISAXS patterns of the four samples recorded at higher incident angles. The splitting of the steaks becomes more and more obvious with the increase of polyelectrolyte layers. The parallel white lines indicate the positions of different diffraction orders. Figure a), b), c) and d) on the left hand side corresponds to sample with 5, 11, 15 and 21 polyelectrolyte layers between the two gold nanoparticle arrays. The curves on the right hand side show the intensity features of the q scan along the streak of each sample. The scan region was chosen to be almost the same in the four samples as indicated by the white rod in Figure a).
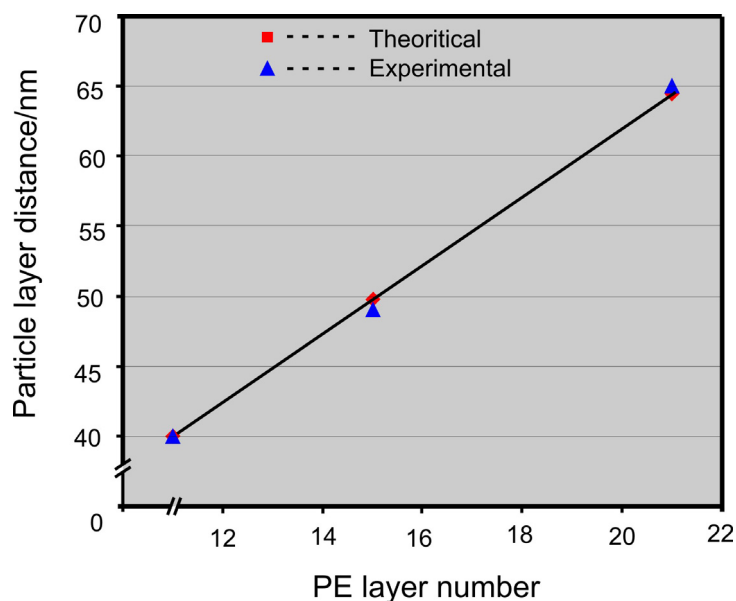
Figure 5.6. Relationship between the distance of the two gold nanoparticle layers and the number of polyelectrolyte layers used in between. Only sample with 11, 15 and 21 polyelectrolyte layers are described here.
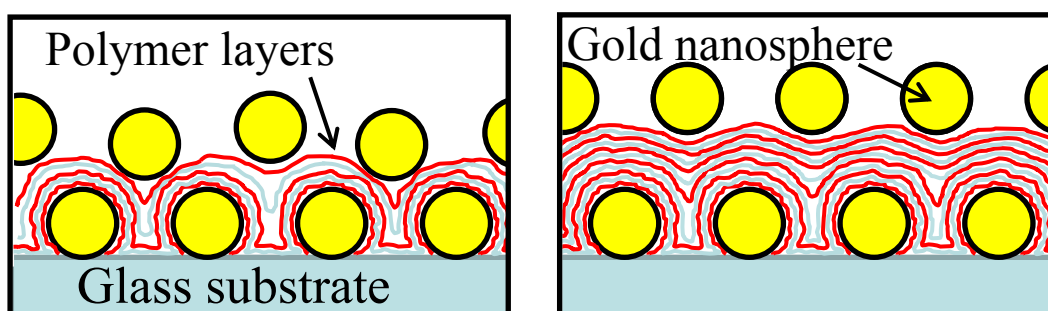

Figure 5.7. The morphology of polyelectrolyte between the two gold nanoparticle layers. Left) if fewer polymer layers are used, they are likely to fill the gaps between neighbouring gold particles, consequently the fluctuation of the vertical positions of the top layer particles are quite obvious. Right) with the increase of polyelectrolyte layers the top surface of this interlayer becomes flat, and then the vertical positions of gold nanoparticles in the second layer can be defined better [167].

The best correlation between the two gold nanoparticle layers is found in the sample with thickest polyelectrolyte layers (21 layers). This can be explained as the unevenness in the polymer layers, originated from the first gold nanoparticle layer, is gradually smoothed out with each polyelectrolyte layer added. As a result, the vertical positions of the second layer gold nanoparticles can be well defined and then better correlation between the two gold layers

formed. At the same time, with the increase of polyelectrolyte layers gold nanoparticles in the same layer tend to distribute more uniformly as detected by Scanning Electron Microscopy (SEM), the results of which will be discussed later. This can also explain why the correlation between the two gold nanoparticle layers is not so good in the sample with only 5 polyelectrolyte layers in between. As for sample with fewer polymer layers (5 layers), the polyelectrolyte are likely to fill the gaps between neighbouring gold particles, and consequently the top polymer layer is not as smooth as in the other samples (see Figure 5.7). In this case, the vertical positions of nanoparticles in the second layer are more broadly distributed and the correlation between two nanoparticle layers can hardly be detected.
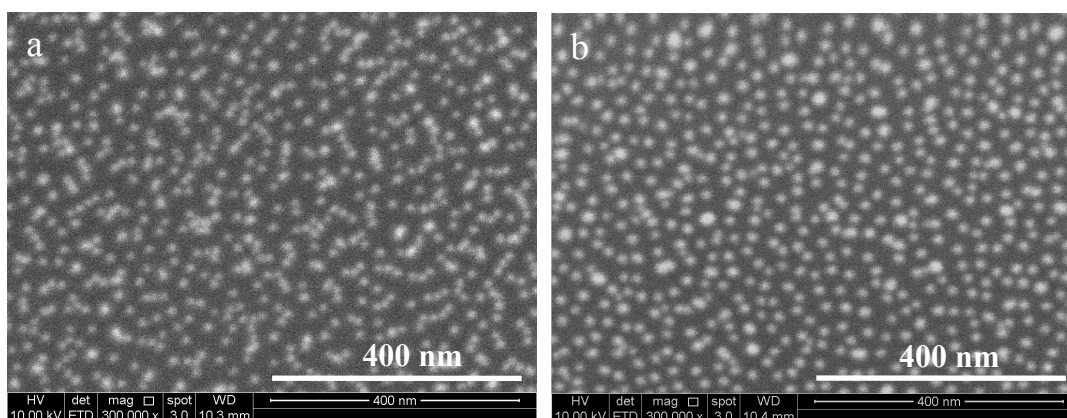

Figure 5.8. The SEM pictures of the double layered gold nanoparticle samples (Contributed by Dr F. Liu). a) Sample with 5 polyelectrolyte layers and b) sample with 15 polyelectrolyte layers in between. Although in both cases the local hexagonal shape formed by the gold nanoparticles is shown, it is more obvious for the sample with more polyelectrolyte layers.

The SEM images of samples with 5 and 15 polyelectrolyte layers are shown in Figure 5.8. It seems that in sample with 5 polyelectrolyte layers (Figure 5.8a) the gold nanoparticles in the second layer distribute more randomly and the sideway correlation is weaker compared with the other sample. This is in line with the above discussed X-ray diffraction results and can also be explained in terms of the surface condition of polyelectrolyte interlayer, as the rough polyelectrolyte surface will affect the location of gold particles in the second layer. The apparent local aggregations of the gold particles present here might be an artefact caused by the observation of gold nanoparticles that belong to both top and bottom layers. For samples with thicker polyelectrolyte layers the sideway correlation of gold nanoparticles becomes

more significant because of the flat polyelectrolyte surface. Figure 5.8b is the SEM image of sample with 15 polyelectrolyte layers, where more uniform particle distribution can be observed and it seems that the neighbouring gold nanoparticles in the same layer tend to have a local hexagonal arrangement.
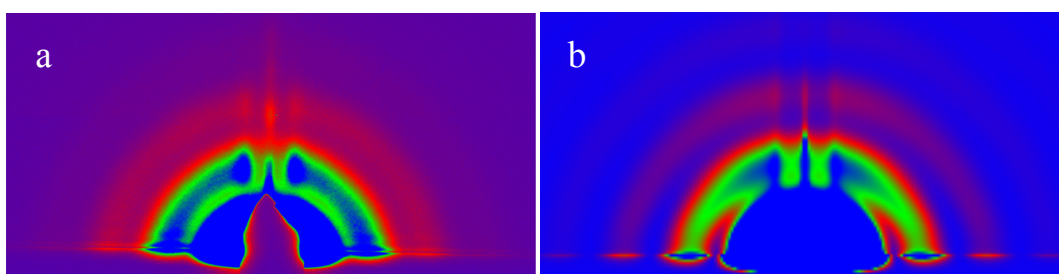

Figure 5.9. a) Experimental GISAXS pattern of sample with 21 polyelectrolyte layers. b) Simulated GISAXS pattern using IsGISAXS software.

Based on the above experimental results, the 2D GISAXS pattern of the multilayer sample was simulated using IsGISAXS software, which is developed by R. Lazzari [170]. The aim of this software is to provide a way to simulate and analyze GISAXS patterns generated from nanostructures, and many simple island geometrical shapes are available in this software. However, the sample geometry is restricted to only one single layer of particles, which means the multiple layered particle arrays were not encompassed in this software [170-171]. So in the current study, this software was employed to simulate the GISAXS pattern of the multilayered sample only when the incident angle is relatively small, in which case it can be considered that the X-ray beam goes through the top gold nanoparticle layer only and the scattering pattern will not be affected by the bottom gold nanoparticle layer.

The simulation was carried out on the basis of gold nanoparticle with spherical geometry, and sideway correlation between particles was also considered. In order to determine more accurately the value of a parameter, a series of simulations have been carried out by setting different values to it with other parameters fixed. And then by comparing with the experimental scattering pattern the best result was chosen to be used to determine other parameters. Eventually, all the parameter values decided in this way were used to simulate the scattering pattern and further optimised by fine adjustment of these parameters.
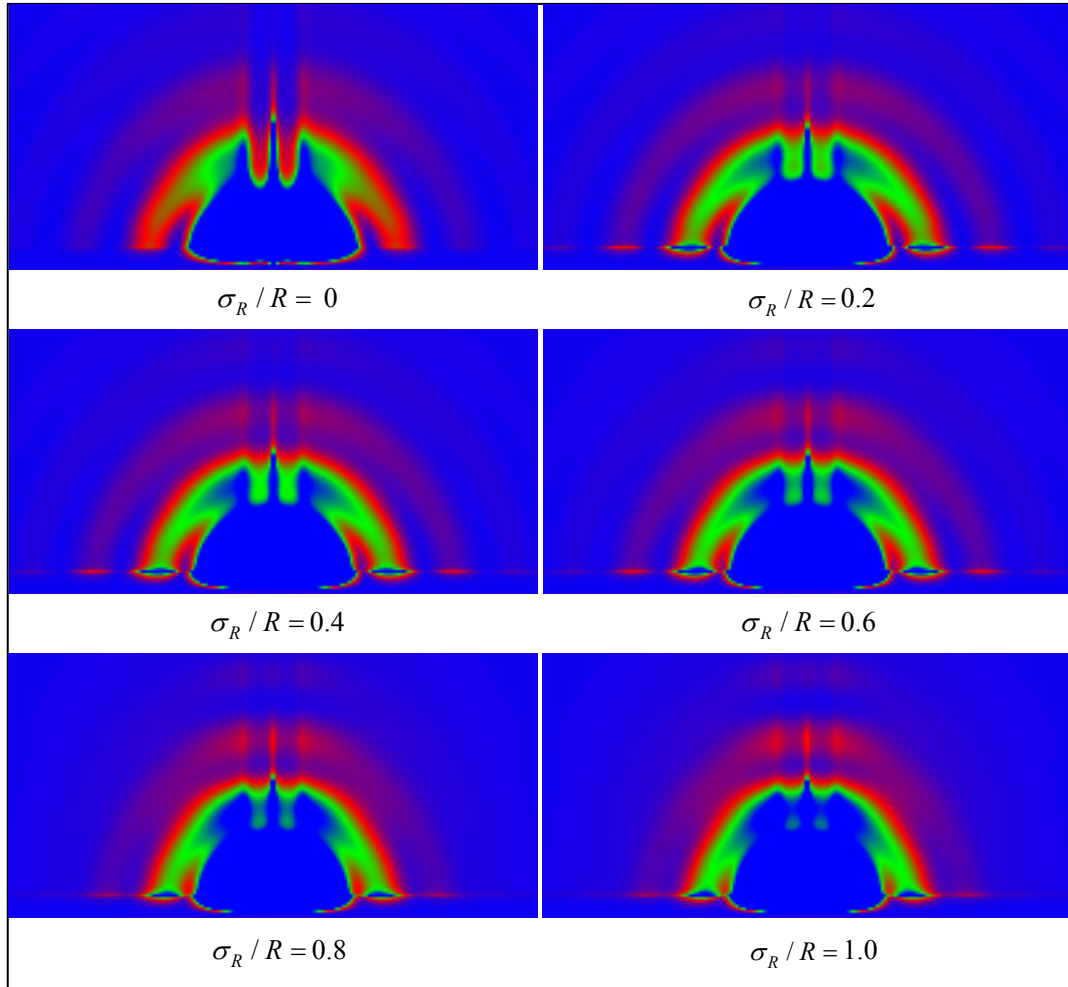
Figure 5.10. The effect of σ_R / R value on the simulated diffraction pattern.

For comparison the experimental and one of the simulation results is shown in Figure 5.9. The simulation pattern was obtained from particle model with a central size of 6.5 nm in radius and this particle size is polydisperse with a Gaussian distribution feature. The relative width of this distribution is dependent on σ_R / R, where R is the central value of radius and σ_R determines the full width at half maximum (*FWHM*) of this distribution which is give by,

$$FWHM = 2\sigma_R \sqrt{2\ln 2} \qquad (5.1)$$

The σ_R value for the simulation pattern shown in Figure 5.9b is 2.1 nm, which means the σ_R / R is about 0.3 and the *FWHM* equals 4.9 nm. From the simulation result we can see the ring-like feature that contains the shape and size information of the particles fits the

experimental results very well. With other decided parameters fixed the effect of σ_R/R on the simulation pattern is shown in Figure 5.10. As we see if the value of σ_R/R is too small the simulation pattern cannot reflect the experimental result properly. While if this value is too large the intensity of scattering rings and the streaks are too strong comparing with the experimental result.
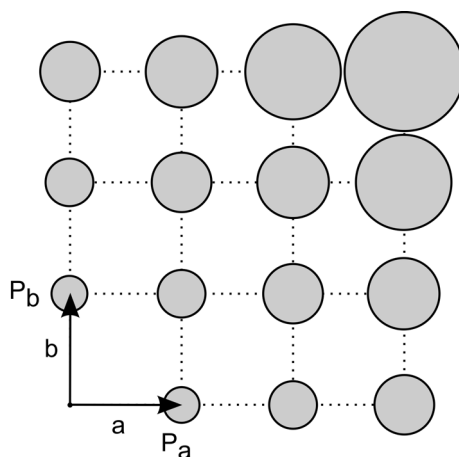

Figure 5.11. Schematic view of a paracrystal in two dimensions. Each circle represents the area where the probability of finding one particle is maximum [172].

In terms of the streaks feature observed in the diffraction pattern, different models have been used to describe the particle correlation during the simulation. The best one in this case is the paracrystal model with hexagonal symmetry which makes a link between the regular lattice and completely disordered structure, and this model is in line with the SEM results discussed above. An example of a two dimensional paracrystal lattice is shown in Figure 5.11 where the paracrystal is built on pseudo regularly lattice with two axes *a* and *b*. In paracrystal model the long range order of the particles is destroyed gradually in a probabilistic way. The possibility of finding a particle at a lattice point which is decided by the regular lattice is different, depending on the distance of this point to the lattice origin. For the position which is far away, the location of a particle at that point becomes more flexible. If the distance is far enough the position of the particle can be considered as disordered. However, it is more likely to find a particle at lattice points close to the origin, *i.e.* locally particles can be considered as possessing the order of a regular lattice.
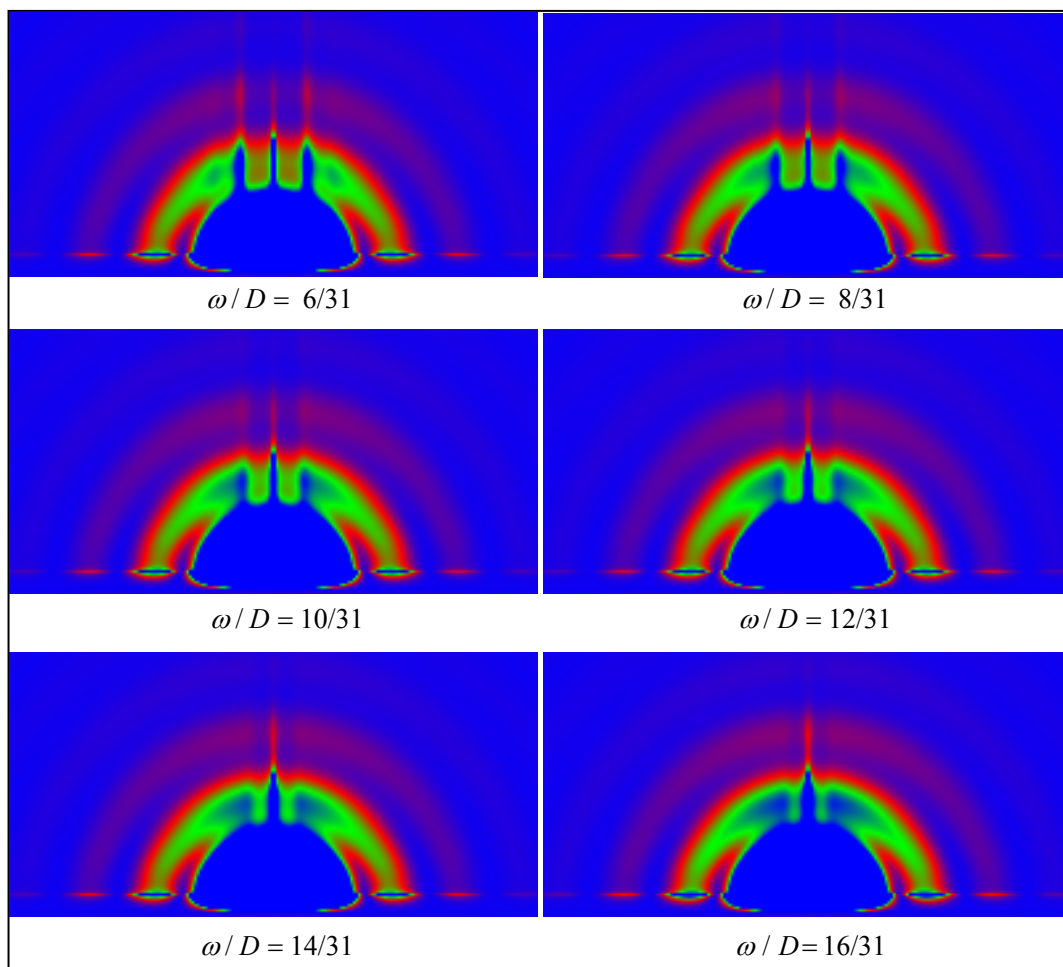
Figure 5.12. The effect of ω/D value on the simulated diffraction pattern.

In this ISGISAX software a parameter ω/D is used to describe the paracrystal feature, where D is the spacing to the first neighbouring peak in the case of disordered lattice, according to the particle sideway distance this value was chosen to be 31 nm during simulation, and ω is the amplitude of disorder factor which can be considered as the position variance of particle. The broadening of the simulated streaks with increasing of ratio ω/D indicates the transition from a more ordered lattice to a more disordered one. The effect of ω/D parameter on the simulation pattern is shown in Figure 5.12, with other fitting parameters fixed. By changing the order of the paracrystal model the streaks shown in experimental result can be simulated very well. If ω/D is too small, which means the positional order of the particles in model is too high, then we can see the second order streaks (*e.g.* $\omega/D = 6/31$). If ω/D is too large then the disorder of the particles in the paracrystal model is over estimated, which results in the

very weak streak feature in the simulation pattern. On comparison, 10/31 is found to be the best value for the ω/D parameter.

5.3 Conclusion

Gold nanoparticle arrays fabricated *via* layer by layer technique have been investigated using grazing incidence small angle X-ray scattering method. Samples containing two gold nanoparticle layers which are separated by 5, 11, 15 and 21 polyelectrolyte interlayers are studied. According to the GISAXS results the gold particles diameter is determined to be 13±0.5 nm in all of the four samples. The sideway correlation of the particles is studied by employing low X-ray incident angles. The results show that this correlation is dependent on the thickness of polyelectrolyte layers. With the increase of this thickness the correlation of gold particles in the same layer becomes more and more obvious, and it seems the gold nanoparticles tend to form hexagonal lattice which has been proved by the SEM images and the paracrystal model used during simulation. In terms of the vertical correlation between the two gold nanoparticle layers, high X-ray incident angles are used. This correlation cannot be observed for the sample with only 5 polyelectrolyte layers, and the best vertical correlation is found in sample with thickest polymer interlayer. The gold nanoparticle size, sideway distance between particles and distance between two gold layers have been determined from GISAXS patterns. For the future experiments, study on sample with only one single gold nanoparticle layer and sample with even thicker polymer interlayer should be carried out for further comparison. Also, some other techniques might be helpful, for example X-ray reflectivity.

Summary

In summary, various nanostructures formed either by liquid crystalline molecule functionalized gold nanoparticles or T-shaped bolaamphiphiles have been investigated by small angle X-ray scattering and grazing incidence small angle X-ray scattering techniques. The combination of the SAXS and GISAXS methods has been proved to be a powerful tool and effective way to probe material structures. In this thesis, nanostructures including both 2D and 3D ones were solved and electron density maps were reconstructed using the experimental diffraction intensities. Based on the reconstructed electron density maps, molecular structure and dimension of unit cell *etc*, model of molecule arrangement in each structure was proposed.

T-shaped bolaamphiphiles, composed of a biphenyl core with polar group at each end and a long chain attached laterally, have been found to form several novel mesophases. By modifying the lateral chain slightly, different phase sequences were observed. In these 2D and 3D mesophases molecules form columns first and these columns then pack in different ways, leading to structures with different symmetries. In the 2D rectangular columnar phase, the column cross section is 10-molecule hexagon which is composed of 10 end-to-end connected biphenyl units. These rigid units shape the wall of each column with the lateral chains inside. In the 3D monoclinic and triclinic structures, the arrangement of molecules is similar to the 2D structure *i.e.* the column cross section is also 10-molecule hexagon. But in the 3D structures the electron density distribution inside each column is different from the 2D one. In this case, local aggregations of the lateral chains were observed due to the changing of molecule configuration at higher temperature. These aggregations caused long range correlation along column direction leading to the formation of the third dimension in these structures. Another different feature found in these 3D structures is the orientation of the rigid biphenyl units with respect to the column axes. The rigid parts of molecules are always found to be perpendicular to the column axes in 2D columnar phases, but in these 3D structures they tilt at an angle. The molecule arrangement found in these 3D structures indicates another way to cope with the expanded lateral chains without collapsing the columnar features, which would otherwise cause the transition to lamellar phases as commonly found in previous research.

In the hybrid system of liquid crystalline molecules functionalized gold nanoparticles, due to the strong orienting influence of the laterally attached rod-like mesogens, the gold nanoparticles were driven to self-assemble and consequently unconventional structures were obtained from these spherical nanoparticles. The effect of co-ligand volume ratio on the self-assembled structure has been studied in this thesis and different mesophases of 2D and 3D ordered structures have been determined. The current results indicate that the final structure formed by the decorated gold nanoparticles to a large extent depends on the surface condition of each particle. There are two controlling factors, the tendency of the anisotropic mesogens to align to form liquid crystal (nematic) phase, and the requirement for space filling. If the volume ratio of mesogen is large, the gold nanoparticles are likely to form ordered structures. However, if only mesogenic ligands were used, in the final self-assembled structure the mesogens form box-like shell around each gold core as consequence of space filling requirement, and this makes the structure optically isotropic with no birefringence observed (*e.g.* sample AuL3). If the gold nanoparticle is functionalized by both mesogen ligand and alkyl chain co-ligand (*e.g.* sample AuL3C6), anisotropic structures can be obtained. In this case the gold nanoparticles form columns which packed on different lattices. The axes of columns are formed by the gold strings, the wall of each column is formed by axially aligned mesogens and the gaps between neighbouring particles in the same column are filled by co-ligands. If the volume ratio of the alkyl chain co-ligand is too large, the decorated gold nanoparticles become similar to conventional spherical particles that every single decorated nanoparticle tends to be isotropic. As a result, close packed cubic structure is obtained (*e.g.* sample AuL3C12). In short, to obtain ordered structures with liquid crystal properties from this hybrid system the control over the volume ratio of the mesogen ligand and alkyl chain co-ligand is critical.

Finally, the self-assembled morphologies of double layered gold nanoparticles have been investigated by grazing incidence small angle X-ray scattering technique. The sideway correlations between gold nanoparticles in the same layer can be investigated by employing small incident angles, as in this case it can be considered that the X-ray beams only pass through the top gold nanoparticle layer. While at higher incident angles the X-ray beams penetrate the layered sample and the vertical correlations between the two gold nanoparticle layers can be investigated. According to the obtained results, it was found that the more polyelectrolyte layers between two gold arrays the better vertical correlation can be observed, as thicker polyelectrolyte interlayer can provide a flatter top surface and consequently the

better defined vertical positions of gold nanoparticles in the second layer become possible. Simulation of the 2D GISAXS pattern was carried out and good agreements between simulation and experimental results have been achieved.

Future Work

Self-assembly of mesogen functionalized gold nanoparticles has been proved as an effective method to arrange spherical nanoparticles into unconventional ordered structures. According to the current results some basic factors that affect the self-assembly process as well as the final structures have been suggested, and these results can be used for guiding the design of functionalized nanoparticles. In terms of future work, different mesogens can be introduced to this hybrid system. Although we have tried to attach chiral molecules to gold nanoparticles and obtained some preliminary results, still more work needs to be done to figure out the interaction between such chiral molecules and gold nanoparticles. There are many theoretical studies predicting that chiral packing of nanoparticles could lead to interesting optical effects, and it would be desirable to achieve such structures through such an self-assembly route. On the other hand, research into gold nanoparticles of larger size or different metallic nanoparticles are some other interesting research aspects required for their better potential as metamaterials and different potential optical applications.

For the self-assembly of T-shaped molecules, lots of work has been done in our group over the past several years. In this thesis attention was just paid to those unsolved complicated mesophases. Most of these structures have been determined but still there is one left at this moment. For this unsolved mesophase further investigations need to be conducted, not only by X-ray diffraction techniques, but also by other methods, for example atomic force microscopy (AFM) *etc*. There are indications, even though still need be proved, that the triclinic phase (new High-T phase) could in fact be chiral. The measurement of its optical properties, such as circular dichroism, would be an interesting step forward.

Some preliminary results of the multilayered gold nanoparticle samples have been discussed in this thesis. Even though the essential features of these samples are presented here, more precise modelling needs to be carried out. As all the current samples contain two gold nanoparticle layers and it is hard to answer how much the sideway correlation is affected by the second nanoparticle layer or not. So for the future experiments, it would be useful to have a sample with only the first gold nanoparticle layer as reference. Moreover, some other

experimental methods, for example X-ray reflectivity *etc*, have been carried out and hopefully will provide more information details about such systems.

Publication and Conference

[1] Xiaobin Mang, Xiangbing Zeng, Baijia Tang *etc*. "Control of Anisotropic Self-assembly of Gold Nanoparticles Coated with Mesogens" *Journal of Materials Chemistry..* Submitted.

[2] Xiaobin Mang, Xiangbing Zeng, Goran Ungar, L. Cesh, G. H. Melh, *"Self-assembled messogen covered gold nanoparticles"*, poster, 24th Annual British liquid crystal society conference. University of Hull, Hull, UK, 29th-31st May 2010.

[3] *Nanogold* project meeting. University of Patras, Greece, 19th-22nd May 2010.

[4] *Nanogold project meeting*. Friedrich Schiller University Jena, Germany, 26th-29th January 2011.

[5] Xiaobin Mang, Xiangbing Zeng, Goran Ungar, Carsten Tschierske. *"3D Liquid Crystal Phases Formed by T-shaped Molecules"*, poster, the 11th European Conference on Liquid Crystals. Maribor, Slovenia, 6th-11th February, 2011.

References

1. Demus, D., et al., *Handbook of Liquid Crystals*. Vol. 1-3. 1998: Wiely-VCH: Weinheim, Germany.

2. Pauluth, D. and K. Tarumi, *Advanced liquid crystals for television.* Journal of Materials Chemistry, 2004. 14(8): p. 1219-1227.

3. Kawamoto, H., *The history of liquid-crystal displays.* Proceedings of the Ieee, 2002. 90(4): p. 460-500.

4. Liu, F., *Complex Supramolecular Self-assembly of T- and X-shaped Amphiphiles.* PhD thesis, 2009.

5. Satyendra, K., *Liquid crystals: experimental study of physical properties and phase transitions*. 2001, UK: Cambridge University Press.

6. P. G. Gennes and J. Prost, *The physics of liquid crystals.* Oxford Science Pubulications, 1995(Second edition).

7. Collings, P.J., *Liquid crystal-nature's delicate phase of matter.* Book, 2002: p. 1-7.

8. Bisoyi, H.K. and S. Kumar, *Liquid-crystal nanoscience: an emerging avenue of soft self-assembly.* Chemical Society Reviews, 2011. 40(1): p. 306-319.

9. Staufer, G., M. Schellhorn, and G. Lattermann, *Cis, cis-(3,5-dihydroxycyclohexyl) - 3,4.bis(alkoxy)benzoates. Thermal behaviour and water absorption.* Liq. Cryst., 1995. 18(4): p. 519-527.

10. Glettner, B., et al., *Liquid-Crystal Engineering with Anchor-Shaped Molecules: Honeycombs with Hexagonal and Trigonal Symmetries Formed by Polyphilic Bent-Core Molecules.* Angew. Chem., Int. Ed., 2008. 47(32): p. 6080-6083.

11. Tschierske, C., *Liquid crystal engineering - new complex mesophase structures and their relations to polymer morphologies, nanoscale patterning and crystal engineering.* Chem. Soc. Rev., 2007. 36(12): p. 1930-1970.

12. Tschierske, C., *Non-conventional liquid crystals-the importance of micro – segregation for self-organization.* J. Mater. Chem., 1998. 8(7): p. 1485-1508.

13. Tschierske, C., *Micro-segregation, molecular shape and molecular topology-partners for the design of liquid crystalline materials with complex mesophase morphologies.* J. Mater. Chem., 2001. 11: p. 2647–2671.

14. Prehm, M., *Komplexe Mesophasenstrukturen polyphiler Blockmoleküle*. 2006, The university of Halle: Halle.

15. Kumar, S., *Self-organization of disc-like molecules: chemical aspects*. Chemical Society Reviews, 2006. 35(1): p. 83-109.

16. Tamba, M.G., et al., *Mesogenic dimers composed of a calamitic and a bent-core mesogenic unit*. Soft Matter, 2006. 2: p. 60-65.

17. Fuchs, P., et al., *A Thermotropic Mesophase Comprised of Closed Micellar Aggregates of the Normal Type*. Angew. Chem., Int. Ed., 2002. 41(4): p. 628-631.

18. Borisch, K., et al., *Tailoring thermotropic cubic mesophases: amphiphilic polyhydroxy derivatives*. J. Mater. Chem., 1998. 8: p. 529 - 543.

19. Cheng, X., et al., *Influence of Semiperfluorinated Chains on the Liquid Crystalline Properties of Amphiphilic Polyols: Novel Materials with Thermotropic Lamellar, Columnar, Bicontinuous Cubic, and Micellar Cubic Mesophases*. Langmuir, 2002. 18(17): p. 6521-6529.

20. Tschierske, C., *Non-conventional soft matter*. Annu. Rep.Prog .Chem. Sect.C, 2001. 97: p. 191–267.

21. Diele, S., *On thermotropic cubic mesophases*. Curr. Opin. Colloid Interface Sci., 2002. 7(5-6): p. 333-342.

22. Kutsumizu, S., *The thermotropic cubic phase: a curious mesophase*. Curr. Opin. Solid State Mater. Sci., 2002. 6(6): p. 537-543.

23. Imperor-Clerc, M., *Thermotropic cubic mesophases*. Curr. Opin. Colloid Interface Sci., 2005. 9(6): p. 370-376.

24. Borisch, K., et al., *Design of Thermotropic Liquid Crystals with Micellar Cubic Mesophases: Amphiphilic N-(2,3-Dihydroxypropyl)benzamides*. Angew. Chem. Int. Ed., 1997. 36: p. 2087-2089.

25. Borisch, K., et al., *Amphiphilic N-benzoyl-1-amino-1-deoxy-D-glucitol derivatives forming thermotropic lamellar, columnar and different types of cubic mesophases*. Liq. Cryst., 1997. 22(4): p. 427-443.

26. Seddon, J.M. and R.H. Templer, in *Handbook of Biological Physics*, R. Lipowsky and E. Sackmann, Editors. 1995, Elsevier: Amsterdam. p. 97-160.

27. Hassan, S., W. Rowe, and G.J.T. Tiddy, in *Handbook of Applied Surface and Colloid Chemistry*, K. Holmberg, Editor. 2002, Wiley-VCH: Chichester. p. 465.

28. Hamley, I.W., *The Physics of Block-Copolymers*. 1998, Oxford: Oxford University Press.

29.   Abetz, V. and P.F.W. Simon, *Phase Behaviour and Morphologies of Block Copolymers.* Adv. Polymer Sci. , 2005. 189: p. 125–212.

30.   Abetz, V. and T. Goldacker, *Formation of superlattices via blending of block copolymers.* Macromol. Rapid Commun., 2000. 21(1): p. 16 - 34.

31.   Hückstädt, H., A. Göpfert, and V. Abetz, *Synthesis and morphology of ABC heteroarm star terpolymers of polystyrene, polybutadiene and poly(2-vinylpyridine).* Macromol. Chem. Phys. , 2000. 201(3): p. 296-307.

32.   Sioula, S., N. Hadjichristidis, and E.L. Thomas, *Direct Evidence for Confinement of Junctions to Lines in an 3 Miktoarm Star Terpolymer Microdomain Structure.* Macromolecules, 1998. 31(23): p. 8429-8432.

33.   Tschierske, C., *Liquid crystal engineering - new complex mesophase structures and their relations to polymer morphologies, nanoscale patterning and crystal engineering.* Chemical Society Reviews, 2007. 36(12): p. 1930-1970.

34.   Bates, F.S. and G.H. Fredrickson, *Block Copolymers---Designer Soft Materials.* Physics Today, 1999. 52(2): p. 32-38.

35.   Ruzette, A.-V. and L. Leibler, *Block copolymers in tomorrow's plastics.* Nat. Mater., 2005. 4(1): p. 19-31.

36.   Judeinstein, P., et al., *Nematogens containing oxyethylene units at a lateral or terminal position and their mixtures with salts.* Liq. Cryst., 2001. 28(11): p. 1691-1698.

37.   Hildebrandt, F., et al., *Formation of columnar mesophases by rod-like molecules: Facial amphiphilic p-terphenyl derivatives.* Advanced Materials, 1997. 9(7): p. 564-&.

38.   Tschierske, C., *Molecular self-organization of amphotropic liquid crystals.* Progr. Polym. Sci., 1996. 21(5): p. 775-852.

39.   Joachimi, D., et al., *Molecular Self-Organization of Amphotropic Cyanobiphenyl Mesogens.* Angew. Chem., Int. Ed., 1993. 32(8): p. 1165-1167.

40.   Lindner, N., et al., *Formation of Columnar and Cubic Mesophases by Calamitic Molecules: Novel Amphotropic Biphenyl Derivatives.* J. Phys. Chem. B, 1998. 102(27): p. 5261-5273.

41.   Neumann, B., et al., *Liquid crystalline macrocycles containing phenylpyrimidine units.* J. Mater. Chem., 2003. 13(4): p. 778-784.

42.   Neumann, B., et al., *Molecular design of amphotropic materials: influence of oligooxyethylene groups on the mesogenic properties of calamitic liquid crystals.* J. Mater. Chem., 1996. 6(7): p. 1087-1098.

43. Malthete, J., H.T. Nguyen, and C. Destrade, *Phasmids and polycatenar mesogens.* Liq. Cryst., 1993. 13(2): p. 171-187.

44. Nguyen, H.T., C. Destrade, and J. Malthete, *Phasmids and Polycatenar Mesogens.* Adv. Mater., 1997. 9(5): p. 375-388.

45. Tschierske, C., *Micro-segregation, molecular shape and molecular topology partners for the design of liquid crystalline materials with complex mesophase morphologies.* Journal of Materials Chemistry, 2001. 11(11): p. 2647-2671.

46. Prehm, M., et al., *New Liquid Crystalline Phases with Layerlike Organization.* J. Am. Chem. Soc., 2002. 124(41): p. 12072-12073.

47. Prehm, M., et al., *Correlated Layer Structures: A Novel Type of Liquid Crystalline Phase with 2D-Lattice.* J. Am. Chem. Soc., 2003. 125(3): p. 614-615.

48. Cheng, X., et al., *Calamitic Bolaamphiphiles with (Semi) Perfluorinated Lateral Chains: Polyphilic Block Molecules with New Liquid Crystalline Phase Structures.* J. Am. Chem. Soc., 2003. 125(36): p. 10977-10996.

49. Cheng, X.H., et al., *Novel Liquid-Crystalline Phases with Layerlike Organization.* Angew. Chem., Int. Ed., 2002. 41(21): p. 4031-4035.

50. Kieffer, R., et al., *Siloxanes and carbosilanes as new building blocks for T-shaped bolaamphiphilic LC molecules.* Soft Matter, 2009. 5(6): p. 1214-1227.

51. Chen, B., et al., *Liquid Crystalline Networks Composed of Pentagonal, Square, and Triangular Cylinders.* Science, 2005. 307: p. 96-99.

52. Chen, B., et al., *Liquid Crystals with Complex Superstructures.* Angew. Chem., Int. Ed., 2004. 43(35): p. 4621-4625.

53. Chen, B., *New Mesophase Morphologies Formed by Facial T-shaped Ternary Amphiphiles.* 2004, University of Halle: Halle.

54. Kölbel, M., et al., *Design of Liquid Crystalline Block Molecules with Nonconventional Mesophase Morphologies: Calamitic Bolaamphiphiles with Lateral Alkyl Chains.* J. Am. Chem. Soc., 2001. 123(28): p. 6809-6818.

55. Schröter, J.A., et al., *Liquid-Crystalline Crown Ether: Forming Columnar Mesophases by Molecular Recognition.* Angew. Chem., Int. Ed., 1997. 36(10): p. 1119-1121.

56. Chen, B., et al., *Carbohydrate Rod Conjugates: Ternary Rod-Coil Molecules Forming Complex Liquid Crystal Structures.* J. Am. Chem. Soc., 2005. 127(47): p. 16578-16591.

57.   El-Sayed, I.H., X.H. Huang, and M.A. El-Sayed, *Surface plasmon resonance scattering and absorption of anti-EGFR antibody conjugated gold nanoparticles in cancer diagnostics: Applications in oral cancer.* Nano Letters, 2005. 5(5): p. 829-834.

58.   Gur, I., et al., *Air-stable all-inorganic nanocrystal solar cells processed from solution.* Science, 2005. 310(5747): p. 462-465.

59.   Konstantatos, G., et al., *Ultrasensitive solution-cast quantum dot photodetectors.* Nature, 2006. 442(7099): p. 180-183.

60.   Talapin, D.V. and C.B. Murray, *PbSe nanocrystal solids for n- and p-channel thin film field-effect transistors.* Science, 2005. 310(5745): p. 86-89.

61.   Ravnik, M., et al., *Entangled Nematic Colloidal Dimers andWires.* Physical Review Letters, 2007. 99: p. 247801-1.

62.   Vroege, G.J., et al., *Smectic Liquid-Crystalline Order in Suspensions of Highly Polydisperse Goethite Nanorods.* Adv. Mater., 2006. 18: p. 2565-2568.

63.   Patrıcio, P., M. Tasinkevych, and M.M.T.d. Gama, *Colloidal dipolar interactions in 2D smectic-C films.* Eur. Phys. J. E, 2002. 7: p. 117-122.

64.   Smith, D.R., J.B. Pendry, and M.C.K. Wiltshire, *Metamaterials and Negative Refractive Index* science, 2004. 305: p. 788-792.

65.   Vlasov, Y.A., et al., *On-chip natural assembly of silicon photonic bandgap crystals.* nature 2001. 414: p. 289-293.

66.   Russel, W., D. Saville, and W. Schowalter, *colloidal dispersions* Cambridge University Press, 1989.

67.   Nazarenko, V.G., A.B. Nych, and B.I. Lev, *Crystal Structure in Nematic Elmulsion.* Physical Review Letters, 2001. 87(7): p. 075504-1.

68.   Borsˇtnik, A., H. Stark, and S. Zumer, *Temperature-induced flocculation of colloidal particles immersed into the isotropic phase   of a nematic liquid crystal.* Physical Review E, 2000. 61(3): p. 2831-2839.

69.   Lev, B.I. and P.M. Tomchuk, *Interaction of foreign macrodroplets in a nematic liquid crystal and induced supermolecular structures.* Physical Review E, 1999. 59(1): p. 591-602.

70.   Borsˇtnik, A., H. Stark, and S.Z. umer1, *Interaction of spherical particles dispersed in a liquid crystal above the nematic-isotropic phase transition.* Physical Review E, 1999. 60(4): p. 4210-4217.

71.   Lubensky, T.C., D. Pettey, and N. Currier, *Topological defects and interactions in nematic emulsions.* Physical Review E, 1998. 57(1): p. 610-625.

72.   Andrienko, D. and M.P. Allen†, *Defect structures and torque on an elongated colloidal particle immersed in a liquid crystal host.* Physical Review E, 2002. 65: p. 041702-1.

73.   Škarabot, M., et al., *Two-dimensional dipolar nematic colloidal crystals.* Physical Review E, 2007. 76: p. 051406-1.

74.   Ravnik, M. and S. Zumer, *Nematic colloids entangled by topological defects.* Soft Matter, 2009. 5: p. 269–274.

75.   Musevic, I., et al., *Two-Dimensional Nematic Colloidal Crystals Self-Assembled by Topological Defects.* science, 2006. 313: p. 954-959.

76.   Nych, A.B., et al., *Coexistence of Two Colloidal Crystals at the Nematic-Liquid-Crystal–Air Interface.* Physical Review Letters, 2007. 98(5): p. 057801-1.

77.   Loudet, J.C., P. Poulin, and P. Barois, *Edge dislocations of colloidal chains suspended in a nematic liquid crystal. Europhys. Lett.*, 2001. 54(2): p. 175-181.

78.   Poulin, P., et al., *Novel Colloidal Interactions in Anisotropic Fluids.* Science, 1997. 275: p. 1770-1774.

79.   Škarabot, M., et al., *Interactions of quadrupolar nematic colloids.* Physical Review E, 2008. 77: p. 031705-1.

80.   Škarabot, M., et al., *Hierarchical self-assembly of nematic colloidal superstructures.* Physical Review E, 2008. 77: p. 061706-1.

81.   Boettcher, S.W., et al., *Tunable electronic interfaces between bulk semiconductors and ligand-stabilized nanoparticle assemblies.* Nat. Mater., 2007. 6(8): p. 592-596.

82.   Grzelczak, M., et al., *Directed Self-Assembly of Nanoparticles.* ACS Nano, 2010. 4(7): p. 3591-3605.

83.   Westerlund, F. and T. Bjørnholm, *Directed assembly of gold nanoparticles.* Current Opinion in Colloid & Interface Science, 2009. 14(2): p. 126-134.

84.   Zeng, Q., et al., *Host−Guest Directed Assembly of Gold Nanoparticle Arrays.* Langmuir, 2009. 26(2): p. 1325-1333.

85.   Ghosh, P., et al., *Gold nanoparticles in delivery applications.* Advanced Drug Delivery Reviews, 2008. 60(11): p. 1307-1315.

86.   Skirtach, A.G., et al., *Laser-induced release of encapsulated materials inside living cells.* Angewandte Chemie-International Edition, 2006. 45(28): p. 4612-4617.

87.   Liliana, C. and G.H. Mehl, *Structure–property relationships in nematic gold nanoparticles.* J. Mater. Chem., 2007. 17: p. 311-315.

88. Giersig, M. and P. Mulvaney, *Preparation of ordered colloid monolayers by electrophoretic deposition. Langmuir*, 1993. 9: p. 3408-3413.

89. Brust, M., et al., *Synthesis of thiol-derivatized gold nanoparticles in a 2-phase liquid-liquid system.* Journal of the Chemical Society-Chemical Communications, 1994(7): p. 801-802.

90. Christine, D.M. and D. Astruc, *Gold Nanoparticles: Assembly, supramolecular Chemistry, Quantum-Size-Related Prpperties, and Applications toward Biology, Catalysis, and Nanotechnology. Chem. Rev.*, 2004. 104: p. 293-346.

91. Henglein, A., *Small-particle research: physicochemical properties of extremely small colloidal metal and semiconductor particles.* Chsm.Rev., 1989. 89(8): p. 1861-1873.

92. Mallia, V.A., et al., *In situ synthesis and assembly of gold nanoparticles embedded in glass-forming liquid crystals.* Angewandte Chemie-International Edition, 2007. 46(18): p. 3269-3274.

93. Wu, Z., J. Suhan, and R.C. Jin, *One-pot synthesis of atomically monodisperse, thiol-functionalized Au(25) nanoclusters.* Journal of Materials Chemistry, 2009. 19(5): p. 622-626.

94. Liliana, C. and G.H. Mehl, *The Design and Investigation of Room Temperature Thermotropic Nematic Gold Nanoparticles.* J. AM. CHEM. SOC., 2006. 128: p. 13376-13377.

95. Bertrand, D., et al., *Dendronized Ferromagnetic Gold Nanoparticles Self-Organized in a Thermotropic Cubic Phase.* Adv. Mater., 2007. 19: p. 3534-3539.

96. Draper, M., et al., *Self-Assembly and Shape Morphology of Liquid Crystalline Gold Metamaterials.* Advanced Functional Materials, 2011: p. n/a-n/a.

97. Zeng, X., et al., *3D Ordered Gold Strings by Coating Nanoparticles with Mesogens.* Adv. Mater., 2009. 21: p. 1-5.

98. Wojcik, M., et al., *Liquid-Crystalline Phases Made of Gold Nanoparticles.* Angewandte Chemie-International Edition, 2009. 48(28): p. 5167-5169.

99. Wojcik, M., et al., *Multidimensional structures made by gold nanoparticles with shape-adaptive grafting layers.* Soft Matter, 2010. 6(21): p. 5397-5400.

100. Ohta, K., et al., *Discotic liquid crystalline semiconductors.* Mol. Cryst. Liq. Cryst, 2003. 397: p. 25-45.

101. M, O.N. and K. SM, *Liquid crystals for charge transport, luminescence, and photonics.* Advanced Materials, 2003. 15(14): p. 1135-1146.

102. Liu, C.-y., et al., *Room Temperature Discotic Liquid Crystalline Thin Films of Hexa-peri-hexabenzocoronene: Synthesis and Optoelectronic Properties.* Chem. Mater., 2003. 15(1): p. 124-130.

103. Kumar, S., et al., *Novel conducting nanocomposites: synthesis of triphenylene-covered gold nanoparticles and their insertion into a columnar matrix.* Soft Matter, 2007. 3: p. 896-900.

104. Shen, Z., M. Yamada, and M. Miyake, *Control of stripelike and hexagonal self-assembly of gold nanoparticles by the tuning of interactions between triphenylene ligands.* Journal of the American Chemical Society, 2007. 129(46): p. 14271-14280.

105. Jin, J., et al., *Self-assembly of uniform spherical aggregates of magnetic nanoparticles through pi-pi interactions.* Angewandte Chemie-International Edition, 2001. 40(11): p. 2135-2138.

106. Ipe, B.I. and K.G. Thomas, *Investigations on nanoparticle-chromophore and interchromophore interactions in pyrene-capped gold nanoparticles.* Journal of Physical Chemistry B, 2004. 108(35): p. 13265-13272.

107. Pyc, P., et al., *Bent-core molecules with lateral halogen atoms forming tilted, synclinic and anticlinic, lamellar phases.* J . Ma t e r . C h em., 2004. 14: p. 2374-2379.

108. Reddy, R.A. and C. Tschierske, *Bent-core liquid crystals: polar order, superstructural chirality and spontaneous desymmetrisation in soft matter systems.* Journal of Materials Chemistry, 2005. 16: p. 907–961.

109. T., N., et al., *Distinct ferroelectric smectic liquid crystals consisting of banana shaped achiral molecules.* Journal of material chemistry, 1996. 6(7): p. 1231-1233

110. Lee, G.W., et al., *Difference in Icosahedral Short-Range Order in Early and Late Transition Metal Liquids.* Physical Review Letters, 2004. 93(3): p. 037802.

111. M.Marx, V., et al., *Bent-core liquid crystal (LC) decorated gold nanoclusters: synthesis,self-assembly, and effects in mixtures with bent-core LC hosts.* Journal of Materials Chemistry, 2008. 18: p. 2983-2994.

112. Tokuhisa, H. and R.M. Crooks, *Interactions between Organized, Surface-Confined Monolayers and Vapor-Phase Probe Molecules. 12. Two New Methods for Surface-Immobilization and Functionalization of Chemically Sensitive Dendrimer Surfaces. Langmuir*, 1997. 13: p. 5608-5612.

113. Krasteva, N., et al., *Self-Assembled Gold Nanoparticle/Dendrimer Composite Films for Vapor Sensing Applications.* Nano Letters, 2002. 2(5): p. 551-555.

114.   Bosman, A.W., H.M. Janssen, and E.W. Meijer, *About Dendrimers: Structure, Physical Properties, and Applications. Chem. Rev.*, 1999. 99: p. 1665-1688.

115.   Balogh, L., et al., *Formation of silver and gold dendrimer nanocomposites.* Journal of Nanoparticle Research, 1999. 1: p. 353–368.

116.   Vossmeyer, T., et al., *Gold Nanoparticle/Polyphenylene Dendrimer Composite Films: Preparation and Vapor-Sensing Properties.* Advanced Materials, 2002. 14(3): p. 238-242.

117.   Garcia, M.E., L.A. Baker, and R.M. Crooks, *Preparation and Characterization of Dendrimer−Gold Colloid Nanocomposites.* Analytical Chemistry, 1998. 71(1): p. 256-258.

118.   Chechik, V. and R.M. Crooks, *Monolayers of Thiol-Terminated Dendrimers on the Surface of Planar and Colloidal Gold.* Langmuir, 1999. 15(19): p. 6364-6369.

119.   Esumi, K., et al., *Role of Poly(amidoamine) Dendrimers for Preparing Nanoparticles of Gold, Platinum, and Silver.* Langmuir, 2000. 16(6): p. 2604-2608.

120.   Frein, S., et al., *Liquid-Crystalline Thiol- and Disulfide-Based Dendrimers for the Functionalization of Gold Nanoparticles.* Helvetica Chimica Acta, 2008. 91: p. 2321-2337.

121.   Woolfson, M.M., *An introduction to X-ray crystallography.* Cambridge University Press, 1997.

122.   Glatter, O. and O. Kratky, *Small angle X-ray scattering.* 1982, London: Academic press Inc.

123.   Adachi, S.-i., J. Kim, and H. Ihee, *Synchrotron-Based Time-Resolved X-ray solution Scattering (Liquidography).* Advances in Lasers and Electro Optics, 2010: p. 778-808.

124.   Caffrey, M. and D.H. Bilderback, *Real-time X-ray diffraction using synchrotron radiation: System characterization and applications.* Nuclear Instruments and Methods in Physics Research, 1983. 208(1-3): p. 495-510.

125.   Dunphy, D., et al., *Dynamic Investigation of Gold Nanocrystal Assembly Using In Situ Grazing-Incidence Small-Angle X-ray Scattering.* Langmuir, 2008. 24(19): p. 10575-10578.

126.   Narayanan, S., et al., *Real-time evolution of the distribution of nanoparticles in an ultrathin-polymer-film-based waveguide.* Physical Review Letters, 2005. 94(14).

127.   Renaud, G., R. Lazzari, and F. Leroy, *Probing surface and interface morphology with Grazing Incidence Small Angle X-Ray Scattering.* Surface Science Reports, 2009. 64(8): p. 255-380.

128. Pietsch, U., *Investigations of semiconductor surfaces and interfaces by X-ray grazing incidence diffraction.* Current science, 2000. 78(12): p. 1484-1495.

129. Parratt, L.G., *Surface study of solid by total reflection of x-ray.* Physical review, 1954. 95(2): p. 359-369.

130. Liu, F., *Complex Supramolecular Self-assembly of T- and X-shaped Amphiphiles*, in *Enginerring Materials.* 2009, The University of Sheffield: Sheffield.

131. Smilgies, D.M., et al., *Synchrotron Radiation News.* 2002. 15(35).

132. Bryant, G.C., et al., *Structural study of spin-coated and LB films of monomeric and oligomeric phthalocyanines.* Thin Solid Films, 1994. 243(1-2): p. 316-324.

133. Busch, P., et al., *Surface induced tilt propagation in thin films of semifluorinated liquid crystalline side chain block copolymers.* Macromolecules, 2007. 40(1): p. 81-89.

134. Tung, S.H., et al., *Hierarchical assemblies of block-copolymer-based supramolecules in thin films.* Macromolecules, 2008. 41(17): p. 6453-6462.

135. Ungar, G., et al., *GISAXS in the study of supramolecular and hybrid liquid crystals*, in *Xiv International Conference on Small-Angle Scattering*, G. Ungar, Editor. 2010, Iop Publishing Ltd: Bristol.

136. Dierking, I., *Textures of Liquid crystals.* 2003.

137. *The Theory of Birefringence.* Cambridge Polymer Group, Consulation, Testing, and Instrumentation for Polymer Materials, 2004.

138. http://www.olympusmicro.com/primer/techniques/polarized/michel.html.

139. Toralf, S., *Polarized Light in Liquid Crystals and Polymers.* 2007.

140. *Tutorials of Materals Studio.* Verison of 4.3, Software from Accelrys.

141. Ishitobi, M., *Introduction to molecular dynamics simulation.* Journal of Japanese Society of Tribologists, 2000. 45(9): p. 649-654.

142. Rapaport, D.C., *An introduction to molecular dynamics simulation.* Computer Simulations of Surfaces and Interfaces, ed. B. Dunweg, D.P. Landau, and A.I. Milchev. Vol. 114. 2003, Dordrecht: Springer. 59-73.

143. Hill, J.-R., L. Subramanian, and A. Maiti, *Molecular modeling techniques in material sciences.* 2005: Boca raton, FL : Taylor & Francis.

144. A. K. Rappe, et al., *A Full Periodic Table Force Field for Molecular Mechanics and Molecular Dynamics Simulations* J. Am. Chem. Soc., 1992. 114: p. 10024-10035.

145. Zeng, X., Y. Liu, and M. Impéror-Clerc, *Hexagonal Close Packing of Nonionic Surfactant Micelles in Water.* The Journal of Physical Chemistry B, 2007. 111(19): p. 5174-5179.

146. Imai, M., et al., *Static and dynamic structures of spherical nonionic surfactant micelles during the disorder-order transition.* Journal of Chemical Physics, 2005. 122(4).

147. Tschierske, C., *Liquid crystals stack up.* Nature, 2002. 419: p. 681-682.

148. Prehm, M., et al., *Distinct Columnar and Lamellar Liquid Crystalline Phases Formed by New Bolaamphiphiles with Linear and Branched Lateral Hydrocarbon Chains.* Chem. Eur. J., 2008. 14(21): p. 6352-6368.

149. Cheng, X., et al., *Polygonal Cylinder Phases of 3-Alkyl-2,5-diphenylthiophene-Based Bolaamphiphiles: Changing Symmetry by Retaining Net Topology.* Chem. Mater., 2008. 20(14): p. 4729-4738.

150. Prehm, M., et al., *The Giant-Hexagon Cylinder Network - A Liquid-Crystalline Organization Formed by a T-Shaped Quaternary Amphiphile.* Angew. Chem., Int. Ed., 2007. 46(42): p. 7972-7975.

151. Prehm, M., et al., *The Giant-Hexagon cylinder network - A liquid-crystalline organization formed by a T-shaped quaternary amphiphile.* Angewandte Chemie-International Edition, 2007. 46(42): p. 7972-7975.

152. Cheng, X., et al., *Liquid Crystalline Bolaamphiphiles with Semiperfluorinated Lateral Chains: Competition between Layerlike and Honeycomb-Like Organization.* J. Am. Chem. Soc., 2004. 126(40): p. 12930-12940.

153. Patel, N.M., et al., *Twist Elasticity and Anchoring in a Lamellar Nematic Phase.* Phys. Rev. Lett., 2004. 92(1): p. 015501.

154. Patel, N.M., et al., *Possible structures for the lamellar-isotropic and lamellar-nematic phases.* Liq. Cryst., 2005. 32(1): p. 55–61.

155. Cseh, L. and G.H. Mehl, *The Design and Investigation of Room Temperature Thermotropic Nematic Gold Nanoparticles.* J. Am. Chem. Soc., 2006. 128(41): p. 13376-13377.

156. Cseh, L. and G.H. Mehl, *Structure-property relationships in nematic gold nanoparticles.* J. Mater. Chem., 2007. 17(4): p. 311-315.

157. Zeng, X., et al., *3D Ordered Gold Strings by Coating Nanoparticles with Mesogens.* Adv. Mater., 2009. 21(17): p. 1746-1750.

158. Jeon, J., et al., *Molecular dynamics simulations of mutilayer films of polyelectrolytes and nanoparticles.* Langmuir, 2006. 22(10): p. 4629-4637.

159. Zhao, J.J., et al., *Nanoparticle-mediated electron transfer across ultrathin self-assembled films.* Journal of Physical Chemistry B, 2005. 109(48): p. 22985-22994.

160. Chapman, R. and P. Mulvaney, *Electro-optical shifts in silver nanoparticle films.* Chemical Physics Letters, 2001. 349(5-6): p. 358-362.

161. Santos, H.A., et al., *Electrochemical study of interfacial composite nanostructures: Polyelectrolyte/gold nanoparticle multilayers assembled on phospholipid/dextran sulfate monolayers at a liquid-liquid interface.* Journal of Physical Chemistry B, 2005. 109(43): p. 20105-20114.

162. Gulaboski, R., et al., *Probing of the voltammetric features of graphite electrodes modified with mercaptoundecanoic acid stabilized gold nanoparticles.* Journal of Physical Chemistry C, 2008. 112(7): p. 2428-2435.

163. Blodgett, K.B. and I. Langmuir, *Built-up films of barium stearate and their optical properties.* Physical review, 1937. 51(11): p. 0964-0982.

164. Decher, G., *Fuzzy Nanoassemblies: Toward Layered Polymeric Multicomposites.* Science, 1997. 277(5330): p. 1232-1237.

165. Peng, C.Q., Y.S. Thio, and R.A. Gerhardt, *Enhancing the Layer-by-Layer Assembly of Indium Tin Oxide Thin Films by Using Polyethyleneimine.* Journal of Physical Chemistry C, 2010. 114(21): p. 9685-9692.

166. Cunningham, A., *Bottom-up fabrication and optical properties of tunable layered arrays of gold nanoparticles.* Presentation, 2010.

167. Cunningham, A., et al., *Coupling of Plasmon Resonances in Tunable Layered Arrays of Gold Nanoparticles.* Journal of Physical Chemistry C, 2011. 115(18): p. 8955-8960.

168. Schmitt, J., et al., *Metal nanoparticle/polymer superlattice films: Fabrication and control of layer structure.* Advanced Materials, 1997. 9(1): p. 61-&.

169. Tronin, A., Y. Lvov, and C. Nicolini, *Ellipsomerty and x-ray reflectomtry charaterization of self-assembly process of polystyrensulfonate and polyallylamine.* Colloid and Polymer Science, 1994. 272(10): p. 1317-1321.

170. Lazzari, R., *IsGISAXS: a program for grazing-incidence small-angle X-ray scattering analysis of supported islands.* Journal of Applied Crystallography, 2002. 35: p. 406-421.

171. J. Daillant and A. Gibaud, *X-ray and neutron reflectivity-principles and applications.* Springer, Berlin Heidlberg, 2009.

172. Lazzari, R., *Manual of IsGISAX: a tool for analyzing grazing incidence small angle x-ray scattering analysis from nanostructures.* 2006.
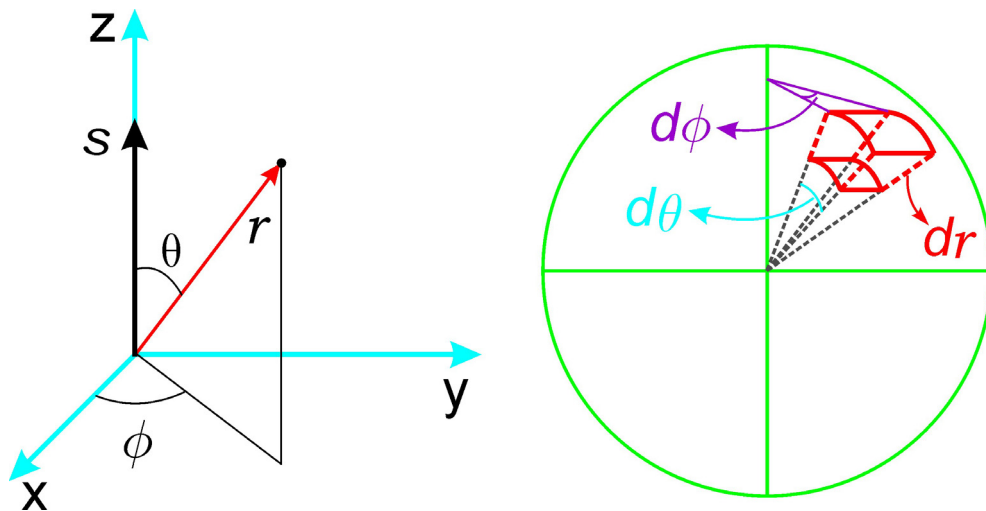
Appendix

A1 The Form Factor of Sphere

Figure A1. The polar coordinate system and the volume element of sphere

The equation 2-17

$$F(h,k,l) = \int_V \rho(x,y,z)\, e^{2\pi i(hx+ky+lz)}\, dv = \int_V \rho(x,y,z)e^{2\pi i s \cdot r} dv$$

Can be written as

$$F(s) = \int_V \rho(x,y,z)e^{2\pi i s \cdot r} dv$$

Where, the vector **s** has the Cartesian components of h, k, l in reciprocal space and the vector **r** can be expressed with the components of x, y, z. In this equation if we change the vector **r** into spherical polar coordinates in terms of three variables r, θ, ϕ as indicated in Figure A1, then we can get the volume element of sphere:

$$dv = r\sin\theta d\phi \cdot rd\theta \cdot dr = r^2 \sin\theta d\theta d\phi dr$$

Since

$$\mathbf{s} \cdot \mathbf{r} = sr\cos\theta$$

So we get

$$F(s) = \int_{\phi=0}^{2\pi}\int_{\theta=0}^{\pi}\int_{r=0}^{\infty} \rho(x,y,z)e^{2\pi is \cdot r \cdot \cos\theta}\sin\theta \, r^2 d\theta d\phi dr$$

$$= 4\pi\int_{r=0}^{\infty} \rho(x,y,z)r^2 \frac{\sin(2\pi sr)}{2\pi sr}dr$$

In this equation if $\rho(x,y,z)$ is real and depends only on the length of vector r, then the integration with respect to θ, ϕ can be performed without knowing of $\rho(x, y, z)$. Due to the spherical symmetry, the electron density ρ_0 of a solid sphere of radius R is defined by

$$\rho(r) = \begin{cases} \rho_0 \cdots\cdots\cdots r \leq R \\ 0 \cdots\cdots\cdots r > R \end{cases}$$

According to the equation 2-5 we know

$$F(q) = 4\pi\int_{r=0}^{\infty} \rho(x,y,z)r^2 \frac{\sin(qr)}{qr}dr$$

$$= \frac{\rho_0}{q}\int_{r=0}^{R} 4\pi r \sin(qr)dr$$

$$= 3\rho_0 V \frac{[\sin(qR) - qR\cos(qR)]}{(qR)^3}$$

This equation is the form factor of spherical particle and V is the volume of the sphere.

A2 Simulation of Diffraction Pattern

Based on the determined unit cell parameters, the GISAXS diffraction patterns of the monoclinic and the triclinic structures have been simulated. To simulate the position of each reflection in the 2D diffraction pattern, the reciprocal unit cell should be determined first.
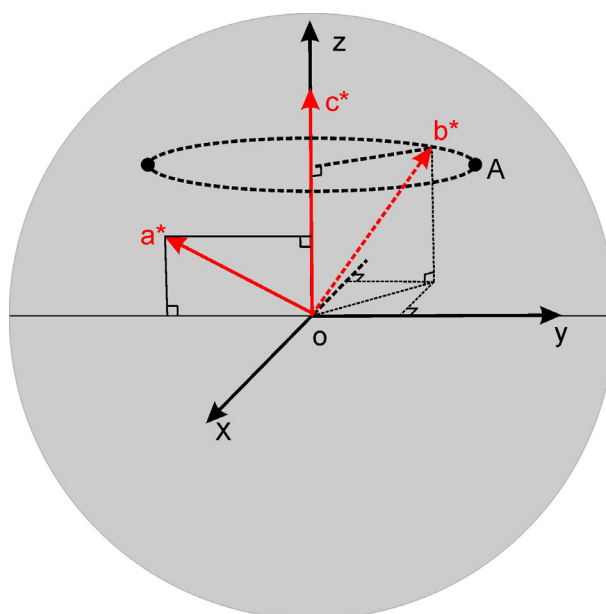

Figure A2. The Geometry of determining the reciprocal unit cell.

In Figure A2 the gray circular plane represents a GISAXS pattern, on top of which a Cartesian coordinate system of the reciprocal space is shown. The unit cell vectors are indicated by a^*, b^* and c^* which define the reciprocal lattice. As each reflection in the diffraction pattern can be considered as the intersection of a reciprocal lattice point with the Awald's sphere and these reflections are generated by rotating the reciprocal lattice with respect to an axis. To simulate the diffraction pattern, we can assume two of the unit cell vectors a^*, c^* are in the plane of this diffraction pattern (the *yz* plane), which means both their directions and positions are fixed. The vector b^* points to a certain direction with its end on the dashed line circle, depending on the unit cell parameters. The modul of b^* is given by point A, where it cuts the Awald's sphere. So the reciprocal unit cell can be written as

$$\boldsymbol{a}^* = x_1\boldsymbol{i} + y_1\boldsymbol{j} + z_1\boldsymbol{k}$$

$$\boldsymbol{b}^* = x_2\boldsymbol{i} + y_2\boldsymbol{j} + z_2\boldsymbol{k}$$

$$\boldsymbol{c}^* = x_3\boldsymbol{i} + y_3\boldsymbol{j} + z_3\boldsymbol{k}$$

The value of x_n y_n z_n ($n = 1, 2, 3$) are the coordinates of the vectors and can be measured or calculated from the diffraction pattern. With the reciprocal unit cell determined, for any given reflection (hkl) with coordinate (x, y, z), it can be expressed by a vector in the reciprocal space as

$$
\begin{aligned}
&h \cdot \boldsymbol{a}^* + k \cdot \boldsymbol{b}^* + l \cdot \boldsymbol{c}^* \\
&= h \cdot (x_1\boldsymbol{i} + y_1\boldsymbol{j} + z_1\boldsymbol{k}) + k \cdot (x_2\boldsymbol{i} + y_2\boldsymbol{j} + z_2\boldsymbol{k}) + l \cdot (x_3\boldsymbol{i} + y_3\boldsymbol{j} + z_3\boldsymbol{k}) \\
&= (hx_1 + kx_2 + lx_3) \cdot \boldsymbol{i} + (hy_1 + ky_2 + ly_3) \cdot \boldsymbol{j} + (hz_1 + kz_2 + lz_3) \cdot \boldsymbol{k} \\
&= x \cdot \boldsymbol{i} + y \cdot \boldsymbol{j} + z \cdot \boldsymbol{k}
\end{aligned}
$$

Where $x = hx_1 + kx_2 + lx_3$, $y = hy_1 + ky_2 + ly_3$ and $z = hz_1 + kz_2 + lz_3$.

Therefore, the horizontal and the vertical positions of this reflection in the 2D diffraction pattern are given by $(\sqrt{x^2 + y^2}, z)$.
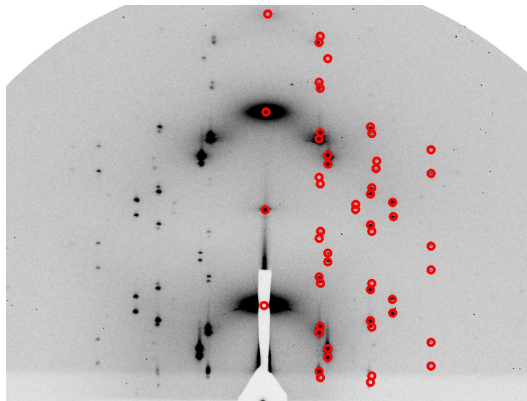

Figure A3. The simulated GISAXS diffraction pattern of the triclinic structure found in the sample T-C$_4$F$_{10}$

A3 Selection of Phase Combination

The electron density map of each structure was reconstructed using the measured diffraction intensities from experimental results. In this section a simple example, the *c2mm* phase of compound T-$C_1(OC_{11}F_8)$, is used to explain the basic rules to choose a reasonable electron density map. For simplicity only three reflections were used here.
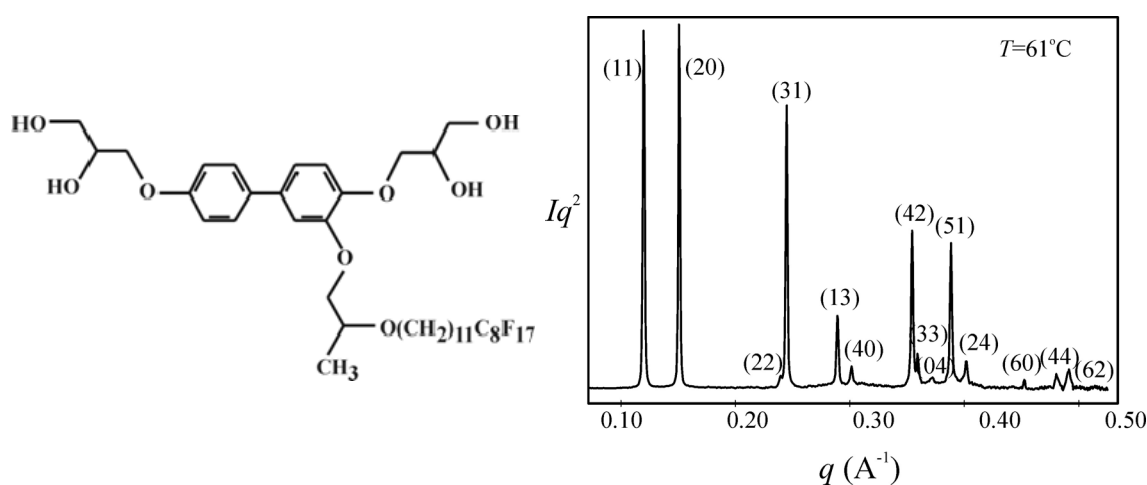

Figure A4. The molecular structure of compound T-$C_1(OC_{11}F_8)$ and the small angle X-ray scattering pattern of the *c2mm* phase recorded at 61 ºC.

Table A1. The Electron densities and volume fractions of the three incompatible segments of the compound shown in Figure A4.

	Volume ratio	Electron density
Biphenyl plus polar group	39.2	0.51
Hydrocarbon spacer	32.3	0.47
Fluorinated end	28.5	0.80

Table A2. The Experimental and calculated *d*-spacings of the observed SAXS reflections for the rectangular columnar phase of sample T-C$_1$(OC$_{11}$F$_8$) at 61 ºC. All the intensity values are Lorentz and multiplicity corrected.

(*hk*)	$d_{obs.}$ (Å)	$d_{calc.}$ (Å)	*I(hk)*
(11)	52.0	52.0	55.3
(20)	41.4	41.4	100.0
(22)	26.1	26.0	2.8

All the possible reconstructions with three reflections are shown in Figure A5. The pairs of phase combinations (000) and (π00), (00π) and (π0π), ($\pi\pi$0) and (0π0), ($\pi\pi\pi$) and (0$\pi\pi$) are basically the same except the origin of the unit cell is shift from (0, 0) to $(0, \frac{1}{2})$. So the different electron density maps can be reduced by half and only four of them need to be considered. Furthermore, the pairs of (000) and ($\pi\pi\pi$), (00π) and ($\pi\pi$0) are simply inverse of each other, therefore the essentially different electron density maps reconstructed from three reflections are only two and here we just need to choose between (000) and (00π). In both maps the purple colour represents the high electron density regions which are contributed by the fluorinated ends the lateral chains, and the red colour means the low electron density areas which contain the hydrocarbon spacers of the lateral chains. The green areas are the medium electron density regions indicating the locations of rigid biphenyl units. The most pronounced difference between the two maps is the volume ratio of different electron density regions. According to calculation (Table A1), among the three parts of the molecule, the fluorinated end and the biphenyl unit has smallest and largest volume ratio respectively. These volume ratios can be corresponded to the electron density map with phase combination (000) very well, as for phase combination (00π) the volume ratio of high electron density region (purple colour) is too large while the medium region (green colour) is smaller than the calculated volume ratio. Therefore, the (000) was determined to be the most reasonable phase combination.

0 0 0

0 0 π

0 π 0

0 π π

π 0 0

π 0 π
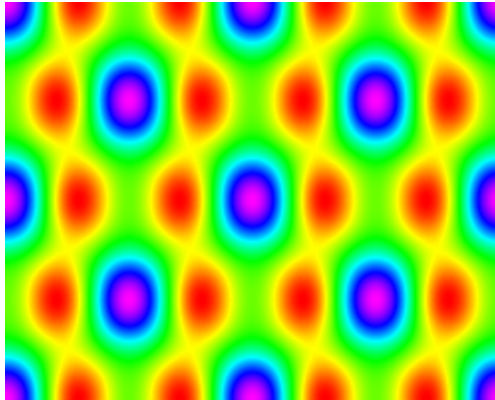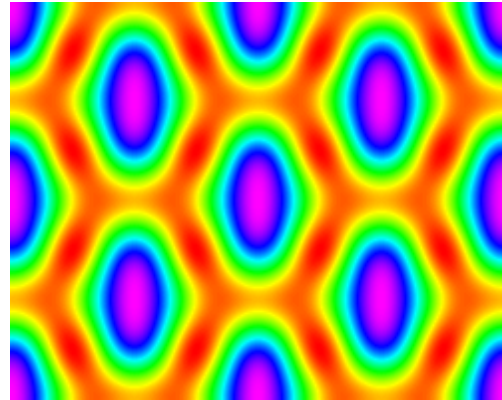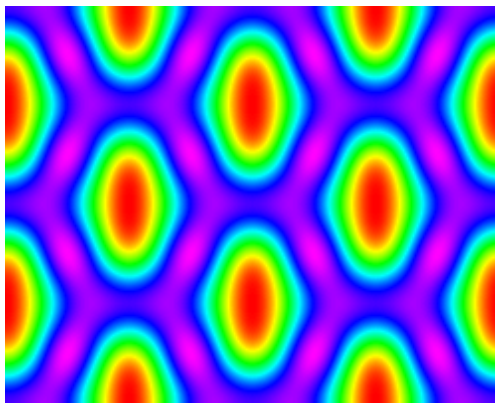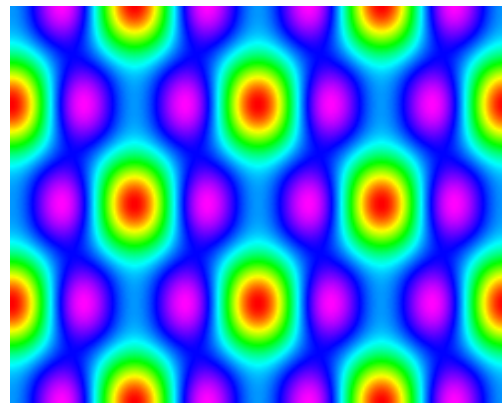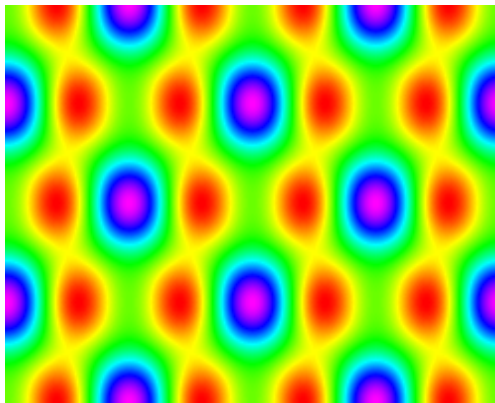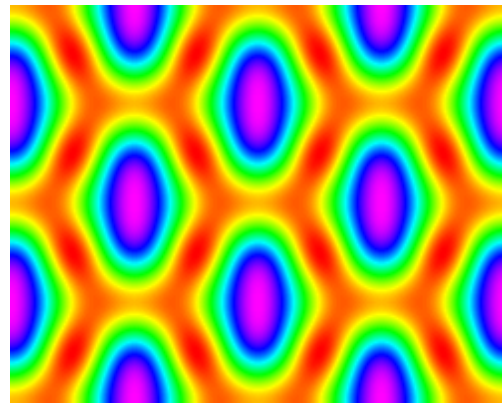
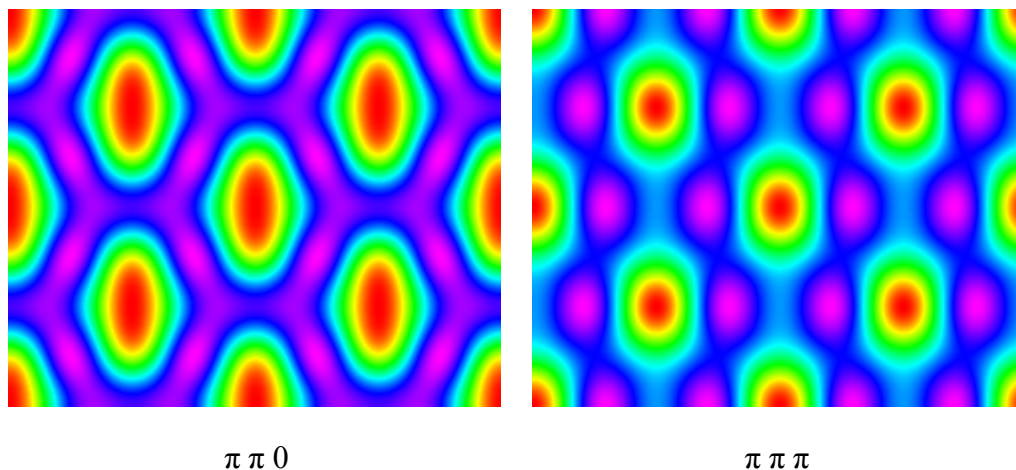$$\pi \, \pi \, 0 \qquad\qquad \pi \, \pi \, \pi$$

Figure A5. All possible phase combinations of the electron density maps of the *c2mm* phase. Reconstruction was carried out using the first three reflections.

A4 Calculation of the Molecule Number

For the mesophases formed by T-shaped molecules, the number of molecules that compose the hexagon in each structure was calculated based on a hypothetical 3D unit cell. In this unit cell two of its axes are in the plane that formed by the rigid biphenyl units of the molecules, and the third axis is along column direction representing the average stacking distances of the molecules along this direction. The calculated result for each structure is given in Table A3, where

V_{cell} = the volume of hypothetical 3D unit cell.

V_{mol} = volume of a single molecule calculated using crystal volume increments. [1]

$n_{cell, cryst}$ = the calculated molecule number based on the average packing coefficient k equals 0.7 in crystal.

$n_{cell, liq}$ = the calculated molecule number based on the average packing coefficient k equals 0.55 in isotropic liquid. [2]

$n_{\text{cell,ave}} = (n_{\text{cell, cryst}} + n_{\text{cell, liq}})/2$, the average number of calculated molecules in the circumference of each hexagon.

Table A3. The calculated parameters of the liquid crystal phases in different compounds

Sample-phase	V_{cell}/ Å^3	V_{mol}/ Å^3	$n_{\text{cell, cryst}}$	$n_{\text{cell, liq}}$	$n_{\text{cell,ave}}$
T-C$_1$(OC$_{11}$F$_8$)-$c2mm$	24926.9	854.6	20.4	16.0	18.2
T-C$_1$(OC$_{11}$F$_8$)-triclinic	14887.1	854.6	12.1	9.5	10.8
T-C$_3$(C$_{11}$F$_8$)-monoclinic	26359.1	891.7	20.7	16.3	18.5
T-C$_3$(C$_{11}$F$_8$)-triclinic	14365.7	891.7	11.3	8.9	10.1
T-C$_4$F$_{10}$- triclinic	14382.2	807.1	12.4	9.8	11.1

1.   Immirzi, A. and B. Perini, *Crystal Physics, Diffraction, Theoretical and General Crystallography.* Acta Crystallogr. Sect. A, 1977. **33**(1): p. 216-218.

2.   Kitaigorodski, A.I., *Molekülkristalle.* Akademieverlag Berlin, 1979.